ulm university universität
uulm

Universität Ulm | 89081 Ulm | Germany **Institute of Physical Chemistry II**

Electronic Structure of Manganese and Manganese Oxide Nanoparticles on a Magnesia Thin Film Surface Investigated with a Novel Femtosecond Extreme Ultraviolet Laser Beamline Setup

Dissertation
zur Erlangung des Doktorgrades
`Dr. rer. nat.`
der Fakultät für Naturwissenschaften
der Universität Ulm

Vorgelegt von:
Christian Weigelt
aus Gifhorn

März 2026

Amtierender Dekan: Prof. Dr. Kay-E. Gottschalk

1. Gutachter: Prof. Dr. Thorsten M. Bernhardt
2. Gutachter: Prof. Dr. Kay-E. Gottschalk
3. Gutachter: Prof. Dr. Ulrich K. Heiz

Tag der Prüfung: 13. Mai 2026

“Eternity is in love with the productions of time.”

— William Blake

Table of Contents

Abbreviations **7**

Abstract **9**

Introduction **11**

1 Theory **15**
1.1 High Harmonic Generation 15
1.1.1 Overview of High Harmonic Generation 15
1.1.2 Three Step Model and Quantum Mechanical Treatments 16
1.1.3 Historical Milestones in HHG and Attosecond Science 22
1.1.4 Applications in Technology and Materials 27
1.2 Principles of Optics 29
1.2.1 Classical Reflection 29
1.2.2 XUV Reflection 32
1.3 Photoelectron Spectroscopy 39
1.3.1 Fundamental Theory of PES 39
1.3.2 Types of PES Spectrometers 42
1.3.3 Calibration of TOF Spectrometers 44
1.3.4 Intensity Scaling in TOF Spectrometers 45
1.4 Surface Analytical Tools 47
1.4.1 Auger Electron Spectroscopy 47
1.4.2 Low Energy Electron Diffraction 49

2 Novel HHG Experimental Setup and its Characterization **53**
2.1 Vacuum and Chamber Design 53
2.1.1 Vacuum Plan 54
2.1.2 Mechanical Design 55
2.1.3 Design of the Semi Infinite Gas Cell 56
2.2 fs-Laser System 58
2.3 Raytracing of the HHG XUV Beamline 59
2.3.1 Material Selection for the Optical Elements 60
2.3.2 Diffraction Grating 61
2.3.3 Toroidal Mirror 63
2.4 HHG Characterization 66
2.5 Surface Preparation 71

2.5.1 Molybdenum Substrate . . . 71
2.5.2 Mg Oven Calibration and MgO Thin Film Preparation . . . 74
2.5.3 Mn Oven Calibration . . . 78
2.6 Integration of the Photoelectron Spectrometer . . . 79
2.6.1 MCP Detector of the PES . . . 79
2.6.2 PES Calibration for HHG . . . 83

3 Experimental Results . . . 87
3.1 Results of Molybdenum PES . . . 87
3.1.1 Spectral Reproducibility . . . 88
3.1.2 Data Processing . . . 89
3.2 Results of Magnesia PES . . . 92
3.3 Results of coverage dependent Manganese PES . . . 93
3.4 Results of oxidized Manganese PES . . . 96

4 Discussion . . . 99
4.1 Mo Substrate Characterization . . . 99
4.2 Magnesia Thin Film Characterization . . . 101
4.2.1 Resolving the MgO Bandgap . . . 103
4.2.2 Momentum-Dependent Oscillations in MgO PES . . . 105
4.2.3 Annealing of MgO Thin Film . . . 108
4.3 Electronic Structure of Mn and MnO Nanoparticles . . . 109
4.3.1 Coverage Dependent Spectral Evolution . . . 109
4.3.2 Progressive Oxidation of Manganese Nanoparticles . . . 111
4.4 Tuneability of the Electronic Structure of Mn and MnO for OER . . . 112

5 Conclusions . . . 115
5.1 Future Investigations . . . 116

A Determining the Blaze Angle for the Grating . . . 119

B Purity Analysis of Mg and Mn through XPS . . . 123

C TOF Uncertainty Calculation . . . 127

Acknowledgments . . . 130

Bibliography . . . 137

Abbreviations

AES	Auger Electron Spectroscopy
CAD	Computer-Aided Design
CF	ConFlat
CPA	Chirped Pulse Amplification
eV	Electronvolt
FWHM	Full Width at Half Maximum
HHG	High Harmonic Generation
IMFP	Inelastic Mean Free Path
I_p	Ionization Potential
IR	Infrared
keV	Kiloelectronvolt
LEED	Low-Energy Electron Diffraction
MgO	Magnesium-Oxide
MHV	Miniature High Voltage
ML	Monolayer Equivalent
MPI	Multiphoton Ionization
nm	Nanometer
OER	Oxygen Evolution Reaction
p-p	Peak-to-Peak
PES	Photoelectron Spectroscopy
REMPI	Resonance Enhanced Multiphoton Ionization
SFA	Strong Field Approximation
SIGC	Semi-Infinite Gas Cell
SMD	Surface Mounted Device
TDDFT	Time-dependent Density-functional Theory
TDSE	Time-dependent Schrödinger Equation
TOF	Time-of-Flight
U_p	Ponderomotive Energy
VBM	Valence Band Maximum
XPS	X-ray Photoelectron Spectroscopy
XUV	Extreme Ultraviolet

Abstract

The kinetic limitations of the Oxygen Evolution Reaction (OER) represent the primary thermodynamic barrier to sustainable fuel production from water. While less abundant, i.e. expensive, noble metal oxides currently overcome this barrier, global scalability necessitates the adoption of earth-abundant analogues. Manganese, inspired by the Mn_4CaO_5 cluster in Photosystem II, has emerged as the leading candidate, with recent advances in nanostructuring and defect engineering demonstrating that synthetic oxides can indeed rival the activity of established noble metal catalysts such as ruthenium and iridium.

However, rational catalyst design faces a major obstacle because the interplay between structural disorder and electronic states at the surface is essentially an analytical blind spot. Conventional bulk-averaging spectroscopies struggle to resolve these details, as they often drown out the signal from the active monolayer.

To overcome this analytical limitation and to isolate the electronic signature of these active sites, this thesis presents the development and application of a surface-sensitive Extreme Ultraviolet (XUV) photoemission spectrometer. In this work, XUV radiation generated by High Harmonic Generation (HHG) provides a coherent, tunable, ultrashort-wavelength probe with sufficient photon energy to access relevant valence states that govern bond breaking and bond formation, while maintaining strong surface sensitivity. Utilizing a HHG source tuned to the minimum of the universal Inelastic Mean Free Path (IMFP) curve, the apparatus achieves monolayer-level surface specificity. This setup was employed to probe manganese and manganese oxide nanostructures deposited on inert magnesium oxide thin films on a molybdenum (100) substrate, to reveal electronic structure properties that aim to foster the OER.

Introduction

As the global energy infrastructure shifts toward decarbonization, hydrogen has emerged as a critical element for storing renewable energy. However, the widespread implementation of hydrogen technology is currently limited by the inefficiency of production through water electrolysis. The fundamental constraint lies in the OER, a kinetically complex step that imposes significant energy losses (Ede and Luo, 2021). While current electrolyzers overcome this barrier using noble metal catalysts like Ruthenium and Iridium, the scarcity and cost of these elements prevent terawatt-scale deployment. To make sustainable hydrogen production a reality, the field must therefore transition to widely available alternatives. This requirement positions Manganese, nature's own choice for water oxidation (Berg et al., 2018), as a primary candidate for future technologies.

Manganese–calcium–oxo clusters act as the core of the biological water oxidation machinery, specifically within the protein complex known as Photosystem II. Here, a cluster of manganese, calcium and oxygen atoms (Mn_4CaO_5) is the catalytic active center for water oxidation. The element is particularly suited for this task because it can adopt a wide variety of oxidation states, ranging from -3 to +7 (Ikeda et al., 2017). This unique property allows manganese to form many different stable structures and oxides. To replicate biological efficiency in the laboratory, these materials are synthesized as nanostructures.

Early studies supported the effectiveness of these design strategies. Brimblecombe et al. (2008) demonstrated sustained water-oxidation photocatalysis using a bio inspired manganese cluster, supporting a biomimetic approach. In parallel, Gorlin and Jaramillo (2010) showed that nanostructured manganese oxides can reach oxygen electrocatalytic activities approaching those of noble metal catalysts (Pt, Ru, Ir).

The field's understanding of the active site was fundamentally shifted by Holger Dau and co-workers (Melder et al., 2020). Rather than treating crystallographic phase purity as the main target, their work showed that highly crystalline Mn-oxide materials often underperform (Baktash et al., 2013). In agreement, Zaharieva et al. (2012) discuss, the most effective water-oxidation catalysts tend to be amorphous or only weakly ordered. This is furthered by Wiechen et al. (2012), who introduce the idea of biomimetic rocks. The core argument is that reproducing the full protein architecture of Photosystem II is not necessary; it can be enough to capture the key local structural and electronic environment around Mn that enables water oxidation using layered Mn oxides such as birnessites. In line with this concept, synthetic calcium manganese oxides were shown to mimic important structural and functional characteristics of the biological catalyst (Zaharieva et al., 2011). Linking structure to function therefore requires access to the surface electronic states that determine reaction energetics and kinetics.

A significant barrier to understanding catalytic mechanisms is the inability of standard characterization tools to isolate surface states from bulk signals. To address the difficulty of isolating weak, surface specific signals, this work employs a specialized custom built HHG apparatus based on a Semi-Infinite Gas Cell (SIGC). The generated XUV radiation is essential for accessing the minimum of the 'Universal Curve', a region where the photoelectron IMFP is shortest.

To fully exploit this surface sensitivity for the analysis of this work, manganese nanostructures are grown on an inert Magnesium-Oxide (MgO) thin film on a molybdenum substrate. This configuration prevents sample charging and ensures that the supporting layers do not interfere with the electronic states in the valence region. Consequently, this specific energy range allows for the exclusive detection of photoelectrons from the topmost atomic layers, granting direct access to the Mn 3d and O 2p valence band orbitals. As a result, this setup effectively isolates the surface electronic signature, allowing for a detailed analysis of the orbitals involved in the catalytic mechanism.

This thesis is structured into five chapters. The theory chapter guides the reader through the historical development of HHG and X-ray optics, before establishing the principles of

Photoelectron Spectroscopy (PES), Auger Electron Spectroscopy (AES), and Low-Energy Electron Diffraction (LEED), which are fundamental surface analysis tools used in this work. With this theoretical background in place, the experimental chapter details the design and construction of the apparatus used to investigate the electronic structure of manganese nanostructures on MgO thin films. The results and discussion chapters form the core of the thesis, presenting the experimental data obtained with the apparatus and providing a critical interpretation of these findings. The thesis closes with concluding remarks and a future outlook.

Chapter 1

Theory

1.1 High Harmonic Generation

1.1.1 Overview of High Harmonic Generation

HHG first observed in the late 1980s, has since evolved into a versatile light source that now forms the basis for a wide spectrum of ultrafast spectroscopic techniques (Frietsch et al., 2013). Strongly focused laser light, through the application of strong field laser matter interaction in gases, undergoes up-conversion into coherent radiation at n-multiples of the fundamental wavelength, reaching the regions of XUV and soft X-ray wavelengths (Coccia and Luppi, 2022). The evolution and continuous improvements in HHG have been driven by parallel advances in laser technology, experimental techniques, novel optics, and improved theoretical understanding (Young et al., 2018). The collective advancements have established HHG to enable the generation of attosecond pulses in the early 2000s, providing the time resolution needed to probe electron dynamics and chemical processes on their natural time scales. (Bauer, 2005)

Initial Discovery of HHG

The first publications on gas-phase HHG were published in 1987 by McPherson et al. (1987) as well as Ferray et al. (1988). This line of work ultimately enabled the generation of attosecond light pulses, which was recognised with the 2023 Nobel Prize in Physics

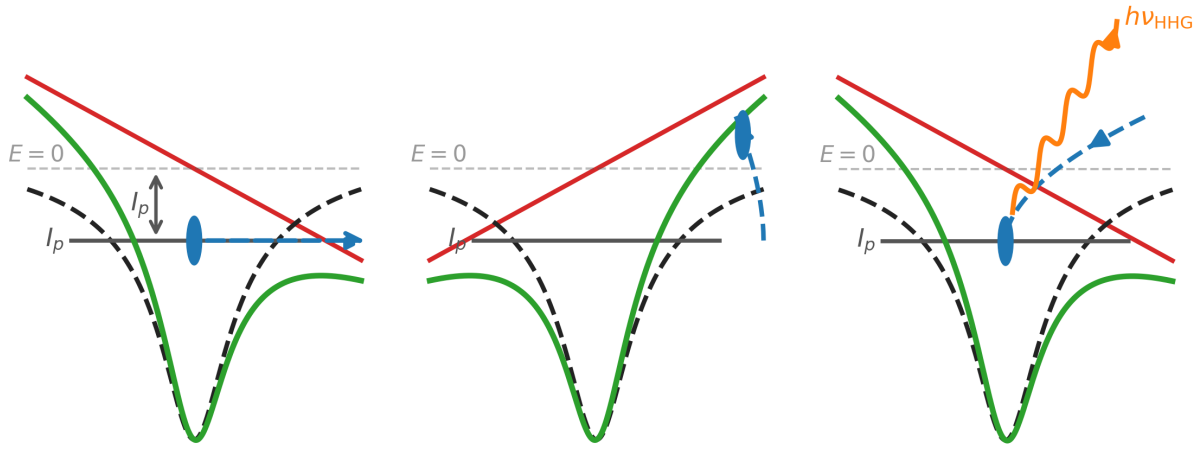
awarded to P. Agostini, F. Krausz, and A. L'Huillier. They observed, when a pulsed laser was intensely focused into a rare gas, the spectral output detected after the gas target featured a series of odd harmonics, which eventually plateaued before reaching the cutoff. This was of great surprise to many, as with other nonlinear effects, it was expected that there should be a rapid drop-off in intensity with increasing harmonic order. This effect defied the expectations of conventional perturbative nonlinear optics, based on higher order susceptibilities. It pointed towards new processes involving quantum mechanics, described by Corkum (1993) and Lewenstein et al. (1994), as detailed in the next section.

The rise of high-power Chirped Pulse Amplification (CPA) femtosecond Ti:sapphire lasers in the early 1990s enabled another big step in HHG research. Ti:sapphire Lasers provided ultrashort pulses on the order of several femtoseconds with astonishing temporal coherence at high peak intensities (Strickland and Mourou, 1985), a breakthrough that was later recognised with the 2018 Nobel Prize in Physics. The perfect combination required for driving HHG. With the heightened flexibility offered by these new lasers, researchers were thus able to better control phase matching, absorption and propagation effects. Long interaction-length geometries such as semi-infinite gas cells and gas-filled hollow-core waveguides can sustain phase matching, enabling the coherent buildup of harmonic radiation over extended distances (Rundquist et al., 1998b). All these experimental improvements allowed for a significant increase in the output of HHG systems and enabled the development of compact tabletop sources.

1.1.2 Three Step Model and Quantum Mechanical Treatments

While experiments advanced rapidly, theoretical insight continued to grow in parallel. The process is commonly described by Corkum (1993) semiclassical three-step model, which combines classical physics with quantum mechanics:

1. An intense laser field (1×10^{15} W/cm^2), which reaches a magnitude comparable to the internal atomic field of an atom, distorts its Coulomb potential to such an extent that an electron can tunnel through the suppressed Coulomb barrier and escape into vacuum.



(a) Step 1 — Tunnel ionisation (b) Step 2 — Acceleration (c) Step 3 — Recombination

Figure 1.1: Schematic of the three-step model of HHG. Potentials shown are unperturbed atomic (dashed black), laser field (red), and total (green). The electron (blue) undergoes: (a) tunnel ionisation, (b) continuum acceleration, and (c) recombination, emitting a high-energy photon.

2. The free electron is accelerated away from the parent ion by the driving electric field of the laser, where it gains kinetic energy.

3. As the laser field reverses its direction, a possibility exists of the wandering electron being forced back towards the atom where it can recombine, thereby emitting a photon in energy corresponding to the sum of the ionization potential and the pondermotive energy it gained in the strong laser field.

This process is illustrated schematically in Figure 1.1, which maps the trajectory of an electron (blue) through the three-step model of HHG. The underlying physics is governed by the superposition of the unperturbed atomic potential (dashed black curvel) and the linear potential of the driving laser electric field (red line), resulting in the total combined potential (green curve). Within this dynamic potential landscape, (a) the electron first undergoes tunnel ionization through the field-suppressed Coulomb barrier. Once liberated (b), it is accelerated away and subsequently back toward the parent ion by the oscillating laser field in the continuum. Finally (c), upon recombination with the parent ion, the kinetic energy acquired during its continuum trajectory, along with the ionization potential, is released as a high-energy photon $h\nu_{\mathrm{HHG}}$. The model enables an foundational understanding of HHG and of its cutoff law:

$$E_{\mathrm{cutoff}} = I_{\mathrm{p}} + 3.17\,U_{\mathrm{p}}. \tag{1.1}$$

It defines how the maximum photon energy reached in the HHG scales with the Ionization Potential (I_p) and the Ponderomotive Energy (U_p) of the tunnelled electron Kapteyn et al. (2005).

Figure 1.2 gives insight into the emission time and the corresponding electron trajectories, which were plotted and calculated with python by solving Newton's equation for an electron released at time t_0:

$$\begin{aligned} F &= ma \\ F &= m\ddot{x}(t) \\ F &= qE \\ F &= -eE_0\cos(\omega t) \\ \therefore m\ddot{x}(t) &= -eE_0\cos(\omega t), \end{aligned}$$

where E_0 and ω are the laser-field amplitude and angular frequency, e is the elementary charge ($q = -e$), and $a = \ddot{x}$ is the acceleration (the second derivative of position). By separating the variables:

$$\ddot{x}(t) = -\frac{eE_0}{m}\cos(\omega t), \tag{1.2}$$

and integrating the equation of motion, with the initial conditions $x(t_0) = 0$, $\dot{x}(t_0) = 0$, with respect to time:

$$\begin{aligned} \int_{t_0}^{t} \ddot{x}(t')\,dt' &= \int_{t_0}^{t} -\frac{eE_0}{m}\cos(\omega t')\,dt' \\ \dot{x}(t) - \dot{x}(t_0) &= -\frac{eE_0}{m\omega}\left[\sin(\omega t')\right]_{t_0}^{t} \end{aligned}$$

$$\dot{x}(t) = -\frac{eE_0}{m\omega}\left[\sin(\omega t) - \sin(\omega t_0)\right]. \tag{1.3}$$

Integrating Equation 1.3 a second time to solve for the electron's position $x(t)$:

$$\int_{t_0}^{t} \dot{x}(t')\,dt' = \int_{t_0}^{t} -\frac{eE_0}{m\omega}\left[\sin(\omega t') - \sin(\omega t_0)\right] dt'$$

$$x(t) - x(t_0) = -\frac{eE_0}{m\omega}\left[-\frac{1}{\omega}\cos(\omega t') - t'\sin(\omega t_0)\right]_{t_0}^{t}$$

$$x(t) = \frac{eE_0}{m\omega^2}\left[\cos(\omega t) - \cos(\omega t_0) + (\omega t - \omega t_0)\sin(\omega t_0)\right]. \tag{1.4}$$

Recollision times t_r satisfy $x(t_\mathrm{r}) = 0$, and the associated kinetic energy is $E_\mathrm{kin}(t_\mathrm{r}) = \frac{1}{2}m\,\dot{x}^2(t_\mathrm{r})$.

The red solid curve shows the normalized driving electric field $E(t) = \cos(\omega t)$ over one optical cycle. The dashed colored curves are the normalized electron displacements for different release times t_0. *Top panel:* $0 \le t_0 \le 0.5\pi$ (first quarter–cycle). Electrons released while $E > 0$ are accelerated in the negative direction, reverse when the field changes sign, and re-encounter the core. *Bottom panel:* $0.5\pi < t_0 \le \pi$ (second quarter–cycle). Electrons born in this half-cycle are accelerated away and never return to the parent ion, so they do not contribute to HHG.

By calculating the maximum kinetic energy across all emission times, one will find that it corresponds to 3.17 times the pondermotive energy (U_p). This result follows from simulations of the electron trajectories in Figure 1.2, with the return energies plotted in Figure 1.3.

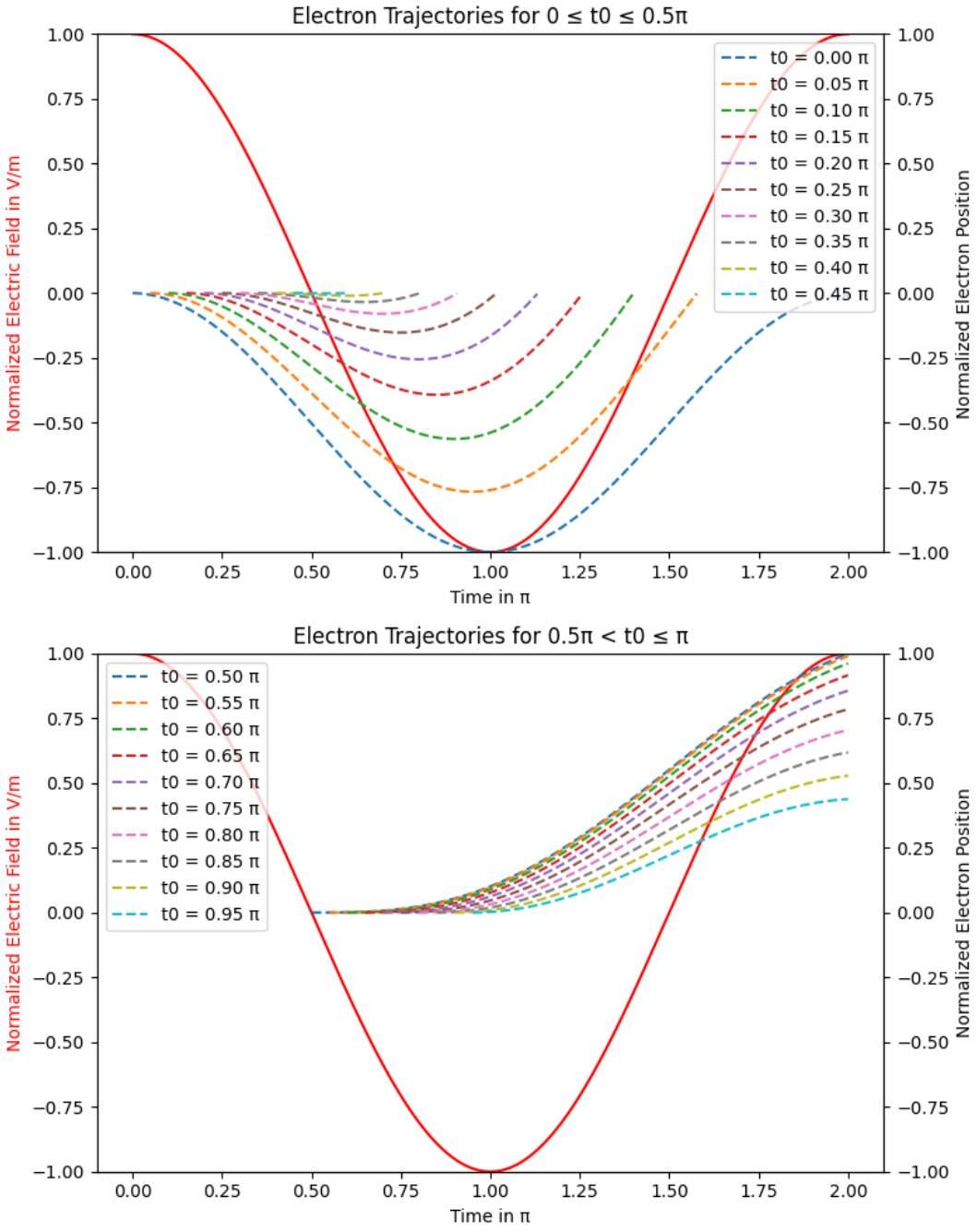


Figure 1.2: Simulated classical electron trajectories in a cosinusoidal electric field.

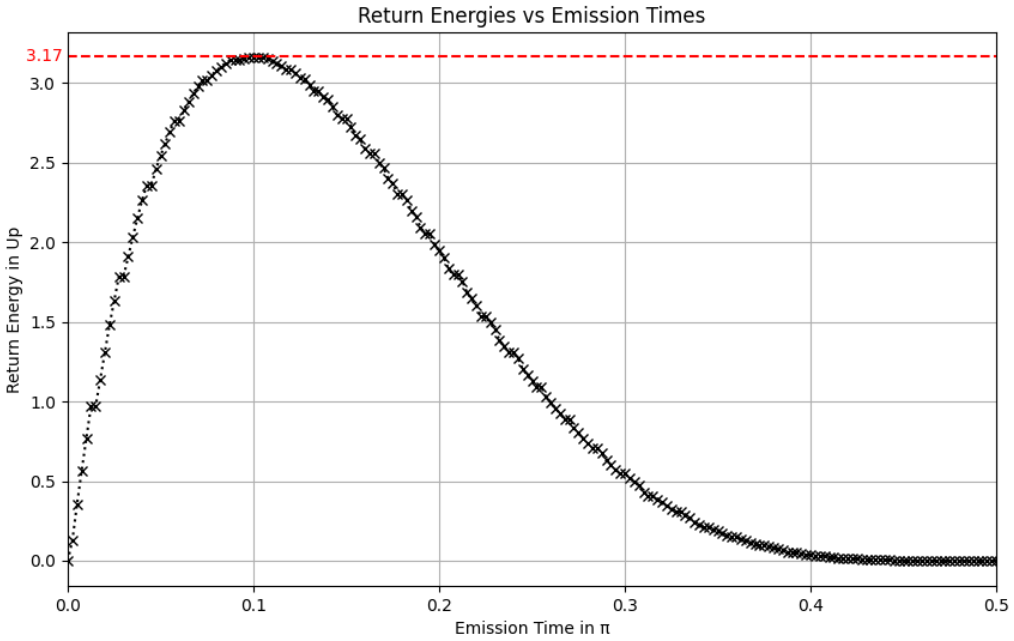


Figure 1.3: Return energies with respect to their emission time.

The Ponderomotive Energy is the cycle-averaged quiver energy of a free electron in an oscillating laser field. It represents the mean kinetic energy an electron gains from being driven back and forth by the field, and is given by:

$$U_\mathrm{p} = \frac{e^2 E_0^2}{4 m_\mathrm{e} \omega^2}, \tag{1.5}$$

where e is the elementary charge, m_e the electron mass, E_0 is the field amplitude and ω the laser frequency.

The above mentioned semiclassical three step model provides an intuitive explanation for the higher harmonic process, but improvements utilizing a deeper quantum mechanical treatment (Schafer et al., 1993), such as the Time-dependent Schrödinger Equation (TDSE) and the Strong Field Approximation (SFA), allow the community to further understand the intricacies of electron dynamics in HHG. These provided fundamental theoretical insights, which classical models did not cover. For example, the plateau region could now be described due to the constructive interference of the many concurrent returning recombining electrons. With Time-dependent Density-functional Theory (TDDFT) phase and

amplitude dependencies and interference effects that govern the temporal structure of the emitted radiation could be calculated and verified as well (Tong and Chu, 1998). The theoretical work has deepened the understanding of the HHG process while furthering new design ideas for the optimization of more advanced HHG sources. With these heightened theoretical insights, HHG has managed to quickly advance. It did not take long for the first experimental breakthroughs to occur.

1.1.3 Historical Milestones in HHG and Attosecond Science

Besides pushing wavelengths to higher energies, one further very exciting possibility with HHG is the ability to generate attosecond pulses. The first pulse durations of 650 attoseconds were published in Hentschel et al. (2001).

A milestone in attosecond metrology was marked by the publication from Itatani et al. (2002) by introducing attosecond streaking. In this method, an XUV pulse ionizes atoms while a synchronized Infrared (IR) field shifts the photoelectrons' kinetic energy in a time-dependent way, mapping the XUV pulse's temporal structure onto the electron spectrum. This enabled pulse duration measurements on the order of 100 attoseconds.

Molecular Orbital Tomography represents another advancement that has been made possible with HHG. With it, researchers were able to reconstruct the electron wavefunctions in molecules to provide insight into their electronic structures. First published by Itatani et al. (2004), the angular dependence of the XUV emission was mapped by varying the molecular alignment with respect to the laser polarization. Using the Fourier relationship between the orbital structure and the transition dipole moment, the researchers were able to directly image the spatial distribution of electron density in the orbital (Patchkovskii et al., 2006).

The first MHz HHG laser system was based on an optical femtosecond enhancement cavity architecture developed in 2005. This system incorporated the gas target directly inside the cavity, leveraging the high circulating pulse energy of a stabilized optical frequency comb to drive HHG at megahertz repetition rates (Labaye et al., 2019).

Aside the previously described scientific breakthroughs, probably the key contributing fac-

tor to all these developments is the fact that an HHG experiment is able to be implemented in a simple compact tabletop system (Rundquist et al., 1998a). With the improved laser stabilization techniques and optimized focusing geometries, scientists are able to develop HHG sources that produce bright light with high spatial and temporal coherence (Brabec and Krausz, 2000).

A further milestone in the HHG development was the extension of the light to higher energies, including the soft X-ray regimes (Kapteyn et al., 2005). Traditionally, rare-gas HHG sources driven by Ti:sapphire lasers were limited to photon energies of odd harmonics below around 100 eV. While useful for many applications, the light did not access core level transitions. Utilizing longer wavelength driving laser, the pondermotive energy could be increased, pushing for a higher cutoff energy. This technique has generated photon energies that reach beyond the water window (282 eV to 533 eV), and in some extreme experimental configurations, even into the Kiloelectronvolt (keV) regions (Spielmann et al., 1997). The extreme broad tunability in photon energy has opened up new applications for XUV and soft X-ray spectroscopy, which are critical for probing inner-shell electron levels.

When reducing the pulse duration of the driving laser something incredibly exciting takes place during the HHG process. While a many-cycle long laser pulse enters the semi-infinite gas cell, a pulse train is produced, meaning a sequence of ultrashort attosecond bursts emitted once per optical half-cycle, so that repeated bursts occur for as long as the driving pulse is present, as seen in Figure 1.4.

Seemingly, the overall duration of the pulse did not change significantly. However, with ever decreasing pulse-durations of the driving laser, ultimately reaching single-cycle bursts, true attosecond pulses emerge (Gallmann et al., 2012). These isolated attosecond pulses, in contrast to the attosecond pulse trains repeated every half cycle of the driving laser, have allowed scientists to perform pump-probe experiments where the HHG pulse acts as an ultrafast probe to capture real-time snapshots of molecular and electronic dynamics (Agostini and DiMauro, 2004).

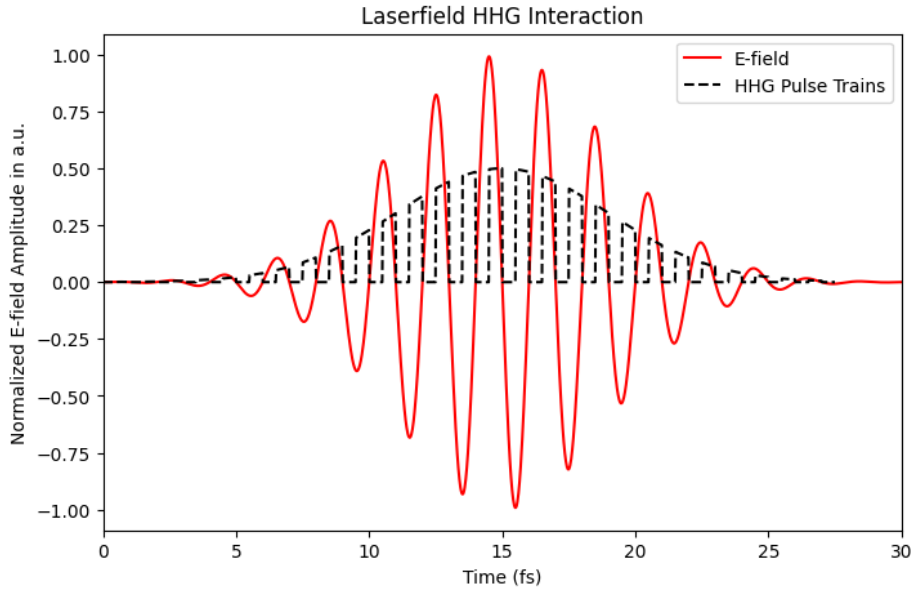


Figure 1.4: In solid red is the underlying electric field of the laser driving the HHG. The dashed black curves show the attosecond bursts, which are generated only in the first quarter–cycle of the cosine driving laser field as explained in Figure 1.2.

Extending Femtochemistry to Attochemistry

The integration of HHG into the field of femtochemistry has offered new exciting possibilities in which chemical reactions can be observed. Pioneered by Ahmed Zewail, femtochemistry revolutionized the understanding of chemical reactions by capturing chemical bonding events on the fs-timescale. By pushing the limits even further into the attosecond regime, HHG sources now offer the possibility to observe dynamics taking place at even faster time scales, e.g. observing electron rearrangements that precede nuclear motion. Integrating HHG with ultrafast spectroscopic techniques such as transient absorption spectroscopy (Geneaux et al., 2019), time-resolved photoelectron spectroscopy (Wernet et al., 2011) and coherent diffraction imaging (Young et al., 2018), enables researchers to deepen the understanding of the ultrafast electronic processes responsible for the subsequent chemical transformations. These experiments reveal information on electron migration and charge separation that occur in the first few moments following photoexcitation. Ultimately, HHG has provided an exciting extension to Zewail's work by opening up the possibility of attochemistry, where electron motion and charge migration can be observed in real time with unprecedented detail (Nandi et al., 2020).

In Zewail's fs-pump-probe experiments, an initial pump pulse would excite an atom or molecule, which would subsequently be probed by a second light pulse. Research in which the second probe pulse would ionize the atom or molecule, heavily relied on Multiphoton Ionization (MPI) (Bernstein and Zewail, 1989). MPI historically played an important role in studying molecular dynamics, as it enabled the ionization of the reaction intermediates with the existing visible light from the experimental setup. Resonance Enhanced Multiphoton Ionization (REMPI) relies on the sequential absorption of photons through intermediate resonant states to ionize a molecule; it is unfortunately limited by the available resonances and the temporal width of the probe pulses. This limits its ability to resolve ultrafast, non-resonant processes.

HHG on the other hand, produces broadband pulses with enough photon energy to enable single-photon excitation. This is of vital importance as it allows for a much broader window of ionizing the reaction intermediates and does not rely on a select wavelength which matches resonant-levels. This enables the direct probing of several intermediates at once with one broadband HHG-pulse. This is particularly significant in fs-pump-probe experiments, where the dynamics of short-lived intermediate states and the evolution of product states need to be captured with high temporal precision. The high temporal resolution and coherent nature of HHG pulses allows for direct probing, providing even deeper insights into reaction mechanisms that were previously inaccessible using REMPI techniques alone.

Surface Aligned Reactions

Gas phase experiments gave first insights into the dynamics of chemical reactions. However, research in heterogenous catalysis fundamentally depends on the support and influence of a surface. Therefore, moving the methodology of femtosecond resolved experiments to the surface was of particular interest.

Polanyi and Zewail (1995) have elegantly phrased the section their paper 'dreaming of the transition state', in which they depict the surface-aligned reaction concept. It emphasizes the role of adsorbate orientation enabling the detection of the coherent nuclear motion of an ensemble of molecules subsequent to being excited with a pump laser pulse. While this dream has not yet been fully realized, the coherent and ultrashort pulses of HHG offer

a powerful probing mechanism. Specifically, mass spectrometry combined with the new HHG beamline presented in this work might ultimately enable the detection of the typical evolution of surface-aligned chemical reactions via one-photon ionization. By capturing the resulting photoelectron and mass spectra, this approach brings us closer to tracking the rearrangement of electronic density in reaction intermediates at the level of detail Polanyi envisioned.

Nevertheless, chemical reactions previously studied in the gas phase can exhibit fundamentally different behaviour when repeated in the presence of a surface. Due to the interaction between the adsorbate molecules and the underlying substrate, the electronic states of the molecules can exhibit completely different configurations. Although, time-resolved experiments on the femtosecond scale were already possible, adapting them for surface studies was non-trivial. Now, the higher-energy light provided by an HHG source unlocks this capability, offering the greater surface sensitivity needed to isolate and probe only the topmost atomic layers. Surface experiments with HHG have been first published by Bauer et al. (2001), demonstrating the use of XUV pulses combined with time-resolved photoemission spectroscopy to directly observe transient changes in the chemical bonding of molecular oxygen adsorbed on a platinum surface.

The reasoning behind the heightened surface sensitivity of XUV radiation lies in the limited escape depth of the emitted photoelectrons. This depth is defined by the IMFP, which describes the average distance an electron can travel through a solid before losing energy. The IMFP λ_m, expressed in monolayers, is described by the universal curve first published by Seah and Dench (1979):

$$\lambda_\mathrm{m} = \frac{538}{E^2} + 0.41\sqrt{aE}, \tag{1.6}$$

where E is the electron energy above the Fermi level in eV and a is the monolayer thickness in nm. As illustrated in Figure 1.5, the mean free path exhibits a distinct minimum in the energy range accessible by XUV sources. The consequence of this minimum, as demonstrated by the experimental results of Bauer (1987), is that electrons originating from deeper within the bulk are scattered before reaching the vacuum, causing the spectroscopic

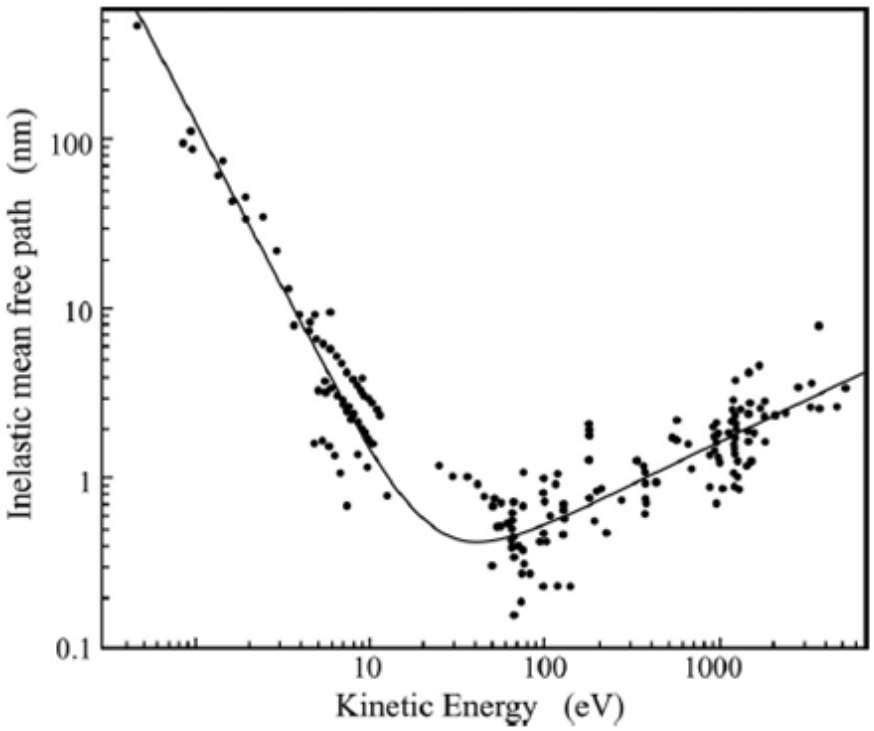


Figure 1.5: Electron Inelastic Mean Free Path (IMFP) versus kinetic energy according to Equation 1.6. Reprinted with permission from (Seah and Dench, 1979) M. P. Seah and W. A. Dench, Surf. Interface Anal. 1979, 1, 2. Copyright 1979 John Wiley & Sons, Ltd.

signal to exclusively record only the outermost atomic layers.

The improvements gained by utilizing HHG are creating new and exciting opportunities for experiments, hopefully opening new directions in femtochemistry at interfaces, where the ultrafast dynamics of charge transfer and bond rearrangement can be investigated under realistic catalytic conditions. Further advancements in laser technology continue to drive the evolution of HHG sources into higher repetition rates, which are particularly appealing for surface studies, where averaging over many events is often necessary to overcome low signal levels.

1.1.4 Applications in Technology and Materials

Beyond answering fundamental questions from physics, HHG is opening new opportunities in heterogeneous catalysis, energy conversion, and materials research. Its ability to resolve charge transfer and electron migration at catalytic interfaces under operating conditions

promises advances in processes such as water splitting and CO_2 reduction (Hruska et al., 2022). In materials science, direct tracking of ultrafast electronic rearrangements at interfaces could guide the design of faster, more efficient electronic and optoelectronic devices (Zürch et al., 2017). By bridging atomic-scale dynamics with macroscopic performance, HHG offers a powerful tool for applied innovation for the future.

HHG has evolved from its discovery in the late 1980s into a powerful tabletop light source for attosecond science. Successive advances in phase matching, high power, and attosecond pulse generation have enabled real-time, element-specific studies of ultrafast chemical dynamics. Building on Zewail's femtochemistry, HHG extends the time resolution to the attosecond scale, allowing direct observation of electron dynamics and transient states in reactions. By surpassing older methods like REMPI, HHG now provides unprecedented temporal and spatial resolution for surface and interface studies, and emerging technologies promise even greater control and selectivity in probing chemical processes.

To address the experimental question of the electronic structure of manganese and manganese oxides, HHG is particularly valuable because it provides access to photon energies in the 30 to 40 eV range, where photoemission becomes highly surface sensitive. As illustrated in Figure 1.5, this energy window corresponds to a minimum in the electron IMFP, so the detected signal is dominated by the near-surface electronic structure rather than the bulk.

1.2 Principles of Optics

1.2.1 Classical Reflection

To access the near-surface electronic structure of Mn and Mn-oxide nanoparticles, this thesis utilizes XUV reflection as a primary diagnostic tool. Because standard geometric optics are ineffective at these wavelengths, highly specialized components are required to guide and focus the beam. To determine the precise design specifications for these XUV optics, the underlying theoretical background governing light-matter interaction in this regime must first be established.

Normal Incidence Reflection

The principles governing optical reflection in the visible spectrum are well established and understood. In the visible spectral region, ranging from 400 Nanometer (nm) to 700 nm, common materials have refractive indices greater than 1 (Hecht, 2023). The refractive index is defined by:

$$n = \frac{c}{v}, \tag{1.7}$$

where n is the refractive index of the medium, c is the speed of light in vacuum, and v is the speed of light in the medium.

Take glass (BK7) for example, it has a refractive index of n $\approx$ 1.52 at 500 nm. In normal incidence, when light hits the surface perpendicularly (parallel to the surface normal), light passes from air (n $\approx$ 1) through glass, the reflection coefficient r and reflectivity R can be calculated with the Fresnel equations (Hecht, 2023). The reflection coefficient is given by:

$$r = \frac{n_1 - n_2}{n_1 + n_2}. \tag{1.8}$$

The reflectivity R is calculated by:

$$R = |r|^2 = \left| \frac{n_1 - n_2}{n_1 + n_2} \right|^2 . \tag{1.9}$$

This calculates the reflectivity, the intrinsic, theoretical reflection at a single ideal interface of the bulk material. If measuring a specific physical piece of glass, the proper term is reflectance, which would additionally account for the sample's specific thickness and secondary reflections from its back surface.

An example with light passing from air through glass in normal incidence in this case would look as follows:

The reflection coefficient r can be calculated with Equation 1.8, which is the ratio of the reflected light wave compared to the incoming light wave:

$$r = \tfrac{n_1 - n_2}{n_1 + n_2} = \tfrac{1.0 - 1.52}{1.0 + 1.52} = \tfrac{-0.52}{2.52} \approx -0.206.$$

This means the reflected light wave is about 20.6% the amplitude of the incoming wave but flipped in phase, due to the negative sign.

The reflectivity, the intrinsic fraction of intensity reflected at this interface, is calculated with Equation 1.9:

$$R = |r|^2 = (-0.206)^2 \approx 0.043.$$

So, approximately 4% of the incident light intensity is reflected at the air-glass interface under normal incidence, while the other 96% is transmitted.

Oblique Incidence Reflection

In the case that light does not approach the boundary between two media perpendicularly, the reflection coefficient changes to Equation 1.10 and 1.11 below. One must include the polarization of light into the calculations as well now. Polarization is a property of transverse waves which specifies the geometrical orientation of the oscillations. As depicted in Figure 1.6, polarization is defined relative to the plane of incidence, which is formed by the incoming light ray and the surface normal. S-polarization is when the electric field is

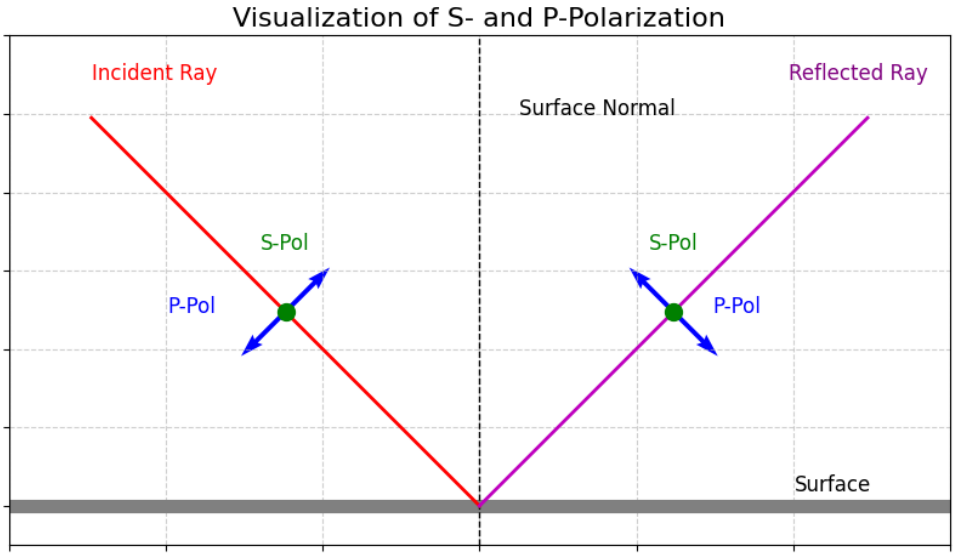


Figure 1.6: The incoming light ray (red line) and the reflected ray (purple line) are shown. The green dot symbolizes s-polarization, whereas the blue arrows indicate p-polarization. The black dashed line represents the surface normal.

perpendicular to the plane of incidence. P-polarization is when the electric field is parallel to the plane of incidence.

The Fresnel reflectance coefficients for oblique incidence are given by:

$$r_{\mathrm{s}} = \frac{n_1 \cos\theta_{\mathrm{i}} - n_2 \cos\theta_{\mathrm{t}}}{n_1 \cos\theta_{\mathrm{i}} + n_2 \cos\theta_{\mathrm{t}}} \tag{1.10}$$

$$r_{\mathrm{p}} = \frac{n_2 \cos\theta_{\mathrm{i}} - n_1 \cos\theta_{\mathrm{t}}}{n_2 \cos\theta_{\mathrm{i}} + n_1 \cos\theta_{\mathrm{t}}}, \tag{1.11}$$

where, θ_{i} corresponds to the angle of incidence, measured between the incoming ray and the surface normal and θ_{t} represents the angle of transmission (or refraction), measured between the refracted ray and the surface normal.

The magnitude of the reflectance is again calculated by squaring the magnitude of the reflection coefficient, as shown previously in Equation 1.9.

Refraction of Light

Additionally, at oblique incidence, one can observe an angular deviation in the direction of the propagation of light. This just occurred in the case of θ_t from Equations 1.10 and 1.11, which is caused by refraction, described by Snell's Law. The refractive index, which was previously defined in Equation 1.7, was the ratio of the different speeds of light in various media; it is also a measure of how much light changes direction of travel when it passes from one medium to another, expressed by:

$$n_1 \sin\theta_i = n_2 \sin\theta_t, \tag{1.12}$$

where n_1 is the refractive index of the incident medium, and n_2 is the refractive index of the transmission medium. The angle θ_i is the angle of incidence, while θ_t is the angle of transmission (or refraction), measured between the refracted ray and the normal (Zinth and Körner, 1998).

1.2.2 XUV Reflection

For photons with wavelengths smaller then 120 nm ($>$ 10 Electronvolt (eV)), the reflectivities change drastically (Rife, 2000). The transition around 120 nm is the point where the increasing photon energy surpasses the bandgap of nearly all conventional transparent materials. As a direct consequence the refractive index, which mainly dictates the reflection capabilities of a materials, falls below 1.

For many materials, especially in the X-ray or XUV regimes, the refractive index is expressed in complex form. This complex form arises from the material's interaction with high-frequency electromagnetic waves, where the electronic response leads to both a reduction in phase velocity (dispersion) and energy loss (absorption) (Jackson, 1975). As the refractive index is very close to unity in this domain, it is often expressed as:

$$n = 1 - \delta + i\beta, \tag{1.13}$$

where δ represents the dispersive term and β the absorption.

To show the poor reflectivity of materials with XUV light, the incident medium is taken to be vacuum ($n_1 = 1$) in the following example. The complex refractive index given above can then be substituted into equation 1.9:

$$R = |r|^2 = \left|\frac{\delta - i\beta}{2 - \delta + i\beta}\right|^2.$$

Since δ, β are on the order of 10^{-3} in the XUV region, we approximate the denominator:

$$2 - \delta + i\beta \approx 2.$$

Thus, the reflectance becomes:

$$R = |r|^2 \approx \left|\frac{\delta - i\beta}{2}\right|^2 = \frac{1}{4}(\delta^2 + \beta^2).$$

Since both δ and β are small values, the reflectance R is also small. The wave penetrates only a very short distance into the material rapidly decaying due to absorption, resulting in very low transmission.

Total External Reflection

Efficient reflection in this wavelength range can be achieved by total external reflection. It is an optical phenomenon which occurs when light travels from a medium with higher refractive index to one with a lower refractive index. At very shallow angles, all the light is reflected from the interface. This is exactly the case with reflections in the XUV region. Total external reflection occurs at very grazing angles of incidence θ_i:

$$\theta_\mathrm{i} < \theta_\mathrm{c},$$

where, the critical grazing angle θ_c is derived from 1.12 with $\theta_\mathrm{t} = 90°$.

$$n_1 \sin\theta_\mathrm{c} = n_2 \sin(90)$$

$$\theta_\mathrm{c} = \sin^{-1}\left(\frac{n_2}{n_1}\right). \tag{1.14}$$

The grazing angle (measured relative to the surface) can be approximated by $\theta_g \approx \sqrt{2\delta}$. Neglecting absorption ($\beta \approx 0$) for a first order analysis in the total external reflection regime, the approximation is derived as follows:

with $\delta \ll 1,\ n_1 = 1$ (in vacuum), and $n_2 = 1 - \delta$:

$$\sin\theta_c = 1 - \delta. \tag{1.15}$$

With $\theta_t = 90°$, $\sin\theta = 1$, we define the small deviation from 90° as:

$$\theta_c = \frac{\pi}{2} - \theta_g, \quad \text{where } \theta_g \ll 1 \tag{1.16}$$

Then:

$$\sin\theta_c = \sin\left(\frac{\pi}{2} - \theta_g\right) = \cos\theta_g, \tag{1.17}$$

with the Taylor series expansion of $\cos\theta_g$ at $\theta_g = 0$, neglecting higher orders as θ_g is small.

$$\sin\theta_c = \cos\theta_g \approx 1 - \frac{1}{2}\theta_g^2 \tag{1.18}$$

Matching both expression 1.15 and 1.18 for $\sin\theta_c$:

$$1 - \delta \approx 1 - \frac{1}{2}\theta_g^2 \quad \Rightarrow \quad \theta_g^2 \approx 2\delta \quad \Rightarrow \quad \theta_g \approx \sqrt{2\delta}. \tag{1.19}$$

Here, an energy of 1 keV and a standard gold coating are used to illustrate the fundamental concept of the critical grazing angle. The delta parameter of gold at this energy is $\delta = 0.0021$.

$$\theta_g \approx \sqrt{2\delta} = \sqrt{2 \cdot 0.0021} = 0.065 \text{ rad } \approx 3.72°$$

The Fresnel reflectivity $R_p = |r_p|^2$ for p-polarized light incident on gold at a grazing angle

of $\theta_g = 3.72°$ is computed. Given at this point:

$$n_1 = 1, \quad n_2 = 1 - 0.002 + i0.001$$

$$\theta_i = 3.72° \Rightarrow \theta_i = \frac{3.72°}{180°}\pi \approx 0.0649 \text{ rad}$$

$$n_1 \sin\theta_i = n_2 \sin\theta_t \quad \Rightarrow \quad \sin\theta_t = \frac{n_1}{n_2}\sin\theta_i$$

From the Pythagorean identity:

$$\sin^2\theta_t + \cos^2\theta_t = 1, \tag{1.20}$$

we solve for $\cos\theta_t$:

$$\cos\theta_t = \sqrt{1 - \sin^2\theta_t} = \sqrt{1 - \left(\frac{n_1^2}{n_2^2}\sin^2\theta_i\right)} = \sqrt{1 - \left(\frac{\sin\theta_i}{n_2}\right)^2}.$$

We then substitute this into the Fresnel formula for p-polarized light 1.11 and calculate the reflectivity with 1.9. First, the Fresnel equation:

$$r_p = \frac{(0.998 + i0.001)\cdot 0.0646 \text{ rad} - 1\cdot\cos\theta_t}{(0.998 + i0.001)\cdot 0.0646 \text{ rad} + 1\cdot\cos\theta_t},$$

which results in $r_p \approx 0.20 - 0.40i$, so the reflectivity is:

$$R_p = |r_p|^2 = (0.20)^2 + (-0.40)^2 \approx 0.04 + 0.16 \approx 0.20 \approx 20\%.$$

This high reflectivity at grazing incidence makes total external reflection an essential principle for designing X-ray and XUV mirrors and optical components.

XUV Mirrors

As discussed in the previous section, the low normal incidence reflectivity in the XUV makes grazing incidence the standard choice for optical design. The mirror substrates are typically coated with materials chosen for their optical constants and durability. Classic substrates for synchrotrons are silicon and silicon carbide for their smoothness and ease of polishing. Reflective coatings, such as gold, platinum and B4C are often employed (Palmer, 2014).

High quality mirrors for XUV light and X-rays must have incredibly smooth surfaces with minimal errors, which are measured in angstroms. These errors, which include figure errors and microroughness, are critical because they cause the beam to scatter (Carl Zeiss SMT GmbH, 2016).

The scattering can also introduce distortions in the reflected beam, such as a pulse front tilt or phase distortions. These distortions are particularly problematic in ultrafast experiments, like those using HHG where the pulse durations lie in the femtosecond regime and below. If the mirror surface is flawed, it can cause different parts of the light pulse to travel slightly different distances, effectively stretching the pulse and ruining the experiment's precise timing. (Poletto et al., 2010)

The optical elements shapes are tailored to the specific function they perform. For focusing in 1-D: elliptical and cylindrical mirrors. 2-D focusing can be achieved with toroidal mirrors, as these have two radii of curvature.

XUV Gratings

In HHG beamlines, the design of the optical system is a critical challenge. Depending on the experiment, the broad spectrum of the HHG is not suitable directly. A harmonic order needs to be selected with a monochromator while managing the relatively low photon flux and preserving the temporal width of the ultrashort pulses, which Frassetto et al. (2011) explain in detail.

Blazed and laminar gratings are the two primary types of gratings being employed. The former possess a sawtooth or triangular groove profile engineered to concentrate a signifi-

cant portion of the diffracted energy into a specific diffraction order. This is achieved by setting an optimal blaze angle that symmetrically aligns the incident and diffracted beams with respect to the facet normal, thereby maximizing efficiency. Laminar gratings have a rectangular groove profile that is relatively straightforward to fabricate, but they tend to spread the diffracted power over several orders rather than concentrating it into one. Their design represents a trade off between spectral resolution and efficiency (Palmer, 2014).

The fundamental operation of gratings is described by the grating equation:

$$m\lambda = d(\sin\theta_\mathrm{i} + \sin\theta_\mathrm{d}), \tag{1.21}$$

where m is the diffraction order, λ is the wavelength, d is the groove spacing, θ_i is the angle of incidence, and θ_d is the diffraction angle (Freund, 1989).

The efficiency of a diffraction grating is critically dependent on its groove density and blaze angle. While a higher groove density enhances spectral resolution by increasing dispersion, it can also lead to a reduction in throughput if the groove profile and depth are not properly optimized. To mitigate this trade off, advanced designs may incorporate gratings with multiple groove densities in a single system, as seen in Poletto et al. (2014). These design choices are typically guided by numerical modelling, for example using rigorous coupled wave analysis (RCWA) following Moharam and Gaylord (1981), and are then validated by high precision metrology, such as the measurements performed at the BESSY II optics beamline (Schäfers, 1996).

A key consideration in grating design is the inherent presence of multiple diffraction orders. While blazed gratings are designed to favor a single order (e.g., $m = 1$), unwanted orders must be suppressed, as shown by Sokolov et al. (2018), through the use of order sorting filters or other optical configurations. There is a fundamental design trade off: optimizing efficiency for a specific order often compromises spectral bandwidth and resolution, requiring careful balancing to achieve desired performance metrics.

As established in the preceding section, XUV optics rely predominantly on grazing incidence geometries to achieve usable reflectivity. This same XUV energy range is ideally

suited for surface sensitive photoelectron spectroscopy, which is employed here to resolve the electronic structure of manganese and manganese oxide nanoparticles. Under XUV illumination, photoelectrons are emitted with high surface sensitivity, and measuring their kinetic energies and emission intensities provides direct access to the near-surface valence electronic structure.

1.3 Photoelectron Spectroscopy

PES is a primary analytical technique for investigating the electronic structure of molecules in the gas phase and on solid surfaces (Hüfner, 1996). Its practical applications are extensive, particularly in fields such as surface chemistry and materials science, as explained by Casu and Chassé (2014), who highlight how it has advanced the understanding of solid-state physics principles. In the context of this thesis, it is employed to answer the experimental question of how the near-surface valence electronic structure of manganese and manganese oxides is configured.

1.3.1 Fundamental Theory of PES

The historical foundation of PES lies in the discovery of the photoelectric effect. In 1887, Hertz (1887) demonstrated that ultraviolet light could cause the emission of negative charge from a solid surface. This phenomenon, which was not initially understood, was a key precursor to modern physics.

Einstein (1905) offered a theoretical explanation for these observations by introducing the concept of the photon, for which he was awarded the Nobel Prize of 1921. He formulated the fundamental photoelectric equation, which relates the maximum kinetic energy (E_{kin}) of an emitted electron to the energy of the incident photon $h\nu$ and the material's work function Φ_0:

$$E_{\text{kin}} = h\nu - \Phi_0. \tag{1.22}$$

This equation established a linear relationship between kinetic energy and photon frequency (ν), a concept that was later experimentally confirmed and solidified the quantum theory of light (Reinert and Hüfner, 2005). However, this model describes the simplest case of electron ejection from the material's surface, where Φ_0 represents the minimum energy required to remove the Fermi electrons in the case of a metal conductor. The electrons which occupy the highest energy state at absolute zero (0 K) are denoted the Fermi electrons.

The phenomenon of photoelectric effect is the basis of PES. While the work function de-

scribes the minimum energy needed, PES experiments measure the unique binding energy (E_B) of each electron (Benigna, 2014). This value provides a direct link to the electron's original energy state within the material. It is defined as the energy required to remove an electron from its specific quantum state to the vacuum level:

$$E_{kin} = h\nu - E_B - \Phi_0. \tag{1.23}$$

With the knowledge of the binding energies, a detailed map of the material's electronic structure, from its valence band to its inner core levels can be determined (Hüfner, 2007). The number of electrons detected with a specific kinetic energy corresponds to the density of states, (D(E)), at that energy level. (Kumar, 2018)

In a PES experiment, following sample excitation, the ejected photoelectrons are detected using an instrument such as a kinetic energy analyzer.

To interpret the measured kinetic-energy spectrum in terms of binding energies, the relevant energy reference levels of the sample and the spectrometer must be defined, including the Fermi level, the vacuum levels, and the role of an applied bias.

Figure 1.7 illustrates the measurement principle. A single photon of energy $h\nu_{pump}$ promotes an electron from an initial state E_1 to a final state E_2 above the sample vacuum level $E_{vac}(pr)$. The energy difference between the sample Fermi level E_F and $E_{vac}(pr)$ is the sample work function Φ_{Pr}.

Only electrons with final-state energies above $E_{vac}(pr)$ are emitted. In the spectrometer, the measured kinetic energy E_{kin} is referenced to the spectrometer vacuum level $E_{vac}(spec)$. The fastest detected electrons originate from the highest occupied initial states near E_F. The slowest detected electrons are those that just overcome $E_{vac}(pr)$ and therefore originate from the deepest states that can still be measured (largest binding energy).

The binding energy of an initial state E_1 is:

$$E_B = E_{vac}(pr) - E_1 = (E_F - E_1) + \Phi_{Pr}. \tag{1.24}$$

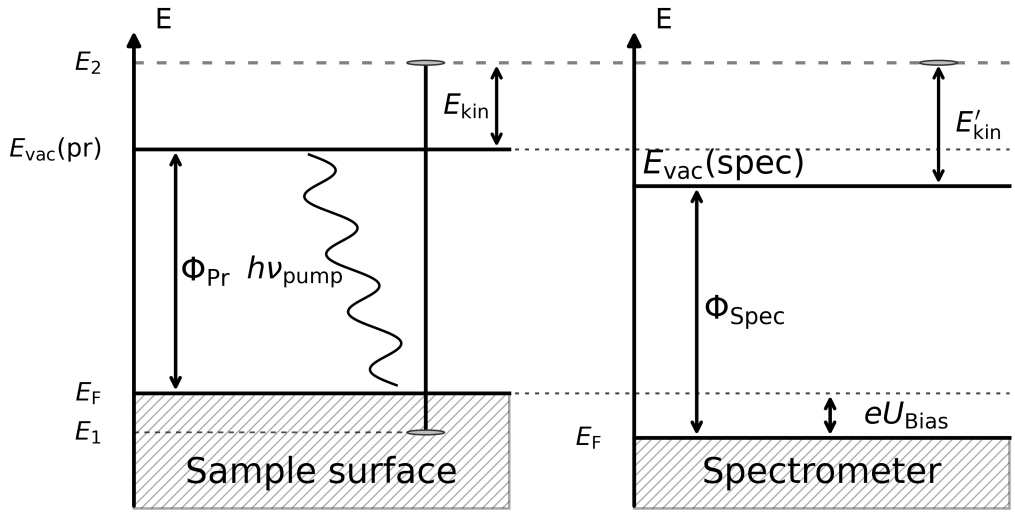


Figure 1.7: Schematic energy diagram of photoemission and spectrometer energy reference.

For $U_{\text{bias}} = 0$, the sample and spectrometer share the same Fermi level because they are electrically connected. For $U_{\text{bias}} \neq 0$, the sample energy scale is shifted by eU_{bias} relative to the spectrometer. If the work functions differ, the vacuum levels are additionally offset by $\Delta E_{\text{vac}} = \Delta\Phi$. As a result, the kinetic energy measured by the analyzer (referenced to E_{vac}(spec)) can differ from the kinetic energy at emission from the sample by these offsets.

If $E_{\text{vac}}(\text{pr}) < E_{\text{vac}}(\text{spec})$, the slowest electrons may not overcome E_{vac}(spec) and will be cut off. To avoid this, a bias voltage U_{bias} is applied such that:

$$eU_{\text{bias}} > \Delta E_{\text{vac}}, \qquad E_{\text{vac}}(\text{pr}) + eU_{\text{bias}} \geq E_{\text{vac}}(\text{spec}), \tag{1.25}$$

so that all emitted electrons can be detected. The spectrometer calibration with a metallic reference establishes the energy scale of the analyzer.

There are several different designs and working principles of these detectors which will be discussed next.

1.3.2 Types of PES Spectrometers

Time-of-Flight (TOF) Spectrometers

TOF spectrometers determine the kinetic energy of photoelectrons by measuring their flight time over a known length. Ideally, they contain a shielded mu-metall tube, which provides a field free flight path. This ensures that the collected electrons's velocities and trajectories are not influenced by stray fields, which would deter the quality of the measurements (Paulus et al., 2006).

The TOF spectrometer offers a simple design, consisting primarily of a drift tube and an electron detector. Samarin et al. (2003) express its key advantage in the parallel measurement of electron energies, where each electron's energy is determined from its characteristic flight time, enabling rapid data acquisition compared to scanning analyzers.

In a TOF setup, electrons are generated by a pulsed light source. The time an electron takes to travel from the sample to the detector is recorded. Kothe et al. (2013) explain the relationship connecting the measured flight time (t), the length of the drift tube (L), and the kinetic energy (E_{kin}) of the photoelectrons by:

$$E_{\text{kin}} = \frac{m_{\text{e}} L^2}{2e(t - t_0)^2}, \tag{1.26}$$

where m_e is the mass of the electron, e is the elemental charge and t_0 represents an intrinsic time offset accounting for delays in electron emission and transit time.

Lastly, the accelerating bias voltage (U_{bias}) applied during the experiment is subtracted to obtain the final binding energy scale:

$$E_{\text{B}} = E_{\text{kin}} - U_{\text{bias}}. \tag{1.27}$$

Magnetic Bottle Spectrometers

Magnetic bottle spectrometers employ a radically different approach to electron collection by exploiting highly inhomogeneous magnetic fields to funnel photoelectrons emitted in

nearly all directions into a common detection region (Kruit and Read, 1983). Typically, a strong permanent magnet or an electromagnet near the sample generates a high magnetic field that captures electrons over an almost full 4π steradian solid angle; as the electrons travel away from the sample into a region with a much weaker, homogeneous magnetic field, their trajectories become nearly collimated, effectively increasing the collection efficiency. The high collection efficiency makes magnetic bottle spectrometers extremely valuable in experiments where signal intensities are low, such as studies of evaporating clusters or liquid jets. However, the design inherently sacrifices angular resolution since the strong magnetic convergence effectively homogenizes the electron trajectories, precluding detailed measurements of the photoelectron emission angles (Kurahashi et al., 2021).

Hemispherical Analysers Spectrometers

For applications where high energy resolution is critical, hemispherical analyzers have long set the standard. The foundational work by Purcell (1938) explains how in these devices, electrons enter a narrow entrance slit and are injected into an electrostatic field between two concentric hemispherical electrodes maintained at different potentials. The resulting field forces electrons with different kinetic energies to follow distinct curved trajectories, so that only electrons within a narrow energy band, known as the pass energy, reach the detector (Imhof et al., 1976). Hemispherical analyzers typically provide energy resolution on the order of tens of millielectronvolts and, when paired with modern 2D detectors, high angular resolution. However, their angular acceptance is much narrower than that of TOF or magnetic bottle systems. Because of this, mapping a full momentum distribution requires either mechanically rotating the sample or using advanced electron-deflection lenses (Zouros and Benis, 2002).

Velocity Map Imaging

Velocity map imaging is an alternative PES setup designed to capture the full 3D momentum of emitted electrons, overcoming the limited collection efficiency of hemispherical analyzers. By using a series of electrostatic lenses to project the expanding electron cloud onto a 2D detector, it achieves nearly 4π collection efficiency in a single measurement (León

et al., 2014). These setups allow for high-resolution momentum mapping without the need for mechanical rotation or extensive post-imaging symmetrization.

1.3.3 Calibration of TOF Spectrometers

The accurate calibration of a TOF photoelectron spectrometer is essential for transforming raw arrival-time data into reliable kinetic-energy scales and, in turn, precise binding energy spectra. Calibration employs a clean metal sample with a known work-function (Φ_0) and a monochromatic photon source (ν) together with a controlled electrostatic bias applied to the sample or extraction optics. By sweeping this bias, one generates reference electrons of known kinetic energy anchored to the metal's Fermi level and the effective work function. For electrons emitted from E_F, they will exhibit following kinetic energy:

$$E_{\mathrm{kin}_0} = h\nu - \Phi_0. \tag{1.28}$$

Measuring the corresponding flight times for several bias voltages yields a set of (t, E_kin) pairs from which a time-to-energy transfer function is obtained by regression. That curve is then applied to subsequent TOF measurements to convert arrival times into accurate kinetic energies, ensuring that the derived binding energy scale is consistent and traceable to well defined standards.

Challenges of TOF Calibration

Several experimental challenges can affect the accuracy of TOF calibration. One of the primary issues encountered is the space charge effect. The occurrence of such space-charge-induced spectral broadening and shift in electron emission from surfaces is described by Hellmann et al. (2009). When a large number of electrons are emitted in response to a single ultrashort pulse, mutual Coulomb repulsion can cause broadening and shifts in the flight time distributions, which in turn degrade the energy resolution of the measurement. To mitigate such effects, experimenters often operate at lower pulse energies, so that only a limited number of electrons are generated in each shot, thereby avoiding distortion and broadening of the peaks.

A further issue that degrades photoelectron spectra during calibration is temporal jitter, which smears spectral features and reduces temporal resolution; therefore, a stable trigger source is necessary.

Additionally, systematic errors can be caused by field distortions from stray electric or magnetic fields, as well as timing offsets introduced by swapping cable lengths. To counter field distortions, mu-metal shielding is employed to guide the electrons in a field-free environment.

With photoelectron spectroscopy established as the central method for mapping the electronic structure of manganese and manganese oxide nanoparticles, the reliability of the results depends on the condition of the surface being probed. Section 1.4 therefore introduces the surface analytical and preparation tools used in this work to produce clean, well-defined surfaces and to verify their composition and morphology prior to PES measurements.

1.3.4 Intensity Scaling in TOF Spectrometers

One important thing to note for the conversion of flight times to kinetic energy is the intensity scaling. Because the data is transformed from the time domain to the energy domain, the signal intensity must be scaled to preserve the total count rate.

To preserve the signal intensity (I) during the transformation from the time domain $I(t)$ to the energy domain $I(E)$, it is required that the area under the curve remains constant:

$$I(E) \cdot dE = I(t) \cdot dt \tag{1.29}$$

The transformed signal $I(E)$ is related to the measured signal $I(t)$ by the Jacobian factor ($J = \left|\frac{dt}{dE}\right|$):

$$I(E) = I(t) \cdot J = I(t) \left|\frac{dt}{dE}\right|. \tag{1.30}$$

This is derived from

$$E = \frac{1}{2} m_\mathrm{e} v^2 = \frac{1}{2} m_\mathrm{e} \left(\frac{L}{t} \right)^2 = \frac{m_\mathrm{e} L^2}{2t^2}. \tag{1.31}$$

Differentiating E with respect to t:

$$\frac{dE}{dt} = \frac{d}{dt} \left(\frac{m_\mathrm{e} L^2}{2t^2} \right) = \frac{m_\mathrm{e} L^2}{2} \frac{d}{dt} \left(\frac{1}{t^2} \right) \tag{1.32}$$

$$= \frac{m_\mathrm{e} L^2}{2} \cdot (-2) \cdot t^{-3} \tag{1.33}$$

$$= -\frac{m_\mathrm{e} L^2}{t^3}. \tag{1.34}$$

This derivative is inverted to give the Jacobian $J = \left| \frac{dt}{dE} \right|$:

$$J = \left| \frac{dt}{dE} \right| = \left| \frac{1}{dE/dt} \right| = \frac{1}{(m_\mathrm{e} L^2)/t^3} = \frac{t^3}{m_\mathrm{e} L^2}. \tag{1.35}$$

Accounting for the initial offset t_0, this leads to:

$$J = \frac{(t_\mathrm{meas} - t_0)^3}{m_\mathrm{e} L^2}. \tag{1.36}$$

1.4 Surface Analytical Tools

Surface science has evolved into a discipline where the atomic-scale organization and composition of materials are probed with exceptional precision. In this context, techniques that are inherently surface sensitive are indispensable for the analysis of ultrathin films and adsorbate layers. Both and AES and LEED exploit the limited escape depth of electrons from the top few atomic layers, thus enabling detailed studies of surface reconstruction, chemical composition, and growth kinetics. By combining LEED's ability to provide direct information about the symmetry and periodicity of surface atomic arrangements with AES's element-specific detection and quantification of chemical species, one achieves a multidimensional understanding of surface phenomena including monolayer formation and interface evolution.

1.4.1 Auger Electron Spectroscopy

Auger spectroscopy exploits a three-electron, non-radiative decay that converts core-hole energy into a characteristic electron signal. A primary electron beam, in the range of 3 keV to 20 keV, ejects an inner-shell electron, creating a vacancy (Gunawardane and Arumainayagam, 2006). An electron from a higher shell then drops into this core level, and the excess energy of this radiationless transition is released in one of two ways: either as an X-ray photon, leaving the atom singly ionized or by expelling a second electron from the atom. As first described by Auger (1925), this emitted particle is the Auger electron which leaves the atom doubly ionized.

Auger electron spectroscopy provides element-specific fingerprints because the emitted electron's kinetic energy is characteristic of the parent atom. Moreover, the nanometre scale escape depth ($\approx$ 1 nm to 3 nm) makes AES intrinsically surface sensitive, ideally suited to probe the outermost atomic layers in thin-film growth, adsorption, and related surface processes (Seah, 1984).

Thin-Film Growth Analysis

Due to the high surface specificity of AES, the technique enables quantitative tracking of a monolayer formation and growth during adsorption and thin-film deposition. Described by Godowski and Hardegree (1994), a clean substrate first exhibits strong Auger peaks that attenuate as an overlayer grows, while adsorbate peaks emerge and strengthen. The adsorbate Auger Peak-to-Peak (p-p) height scales linearly with coverage, whereas the substrate p–p height is a weighted sum of the contribution from uncovered regions and the attenuated contribution from covered regions. Denoting coverage (Θ) in the range of ($0 < \Theta < 1$), the adsorbate ($h_A(\Theta)$) and substrate signals ($h_S(\Theta)$) are:

$$h_{\mathrm{A}}(\Theta) = h_{\mathrm{A}}^{\mathrm{B}} K_{\mathrm{A}} \Theta \tag{1.37}$$

$$h_{\mathrm{S}}(\Theta) = h_{\mathrm{S}}^{\mathrm{B}} \left[1 - K_{\mathrm{S}} \Theta \right] \tag{1.38}$$

where $\mathrm{h_A^B}$ and $\mathrm{h_S^B}$ are the bulk p-p heights for adsorbate (A) and substrate (S), and $\mathrm{K_A}$ and $\mathrm{K_S}$ are constants at the given kinetic energy. For quantitative work that avoids absolute-intensity drift, a ratio of two substrate peaks at low (L) and high (H) kinetic energies is used. With:

$$r_{\mathrm{LH}} \coloneqq \frac{h_{\mathrm{L}}}{h_{\mathrm{H}}}, \qquad r_{\mathrm{LH}}^{\mathrm{B}} \coloneqq \frac{h_{\mathrm{L}}^{\mathrm{B}}}{h_{\mathrm{H}}^{\mathrm{B}}}, \tag{1.39}$$

the ratio measured at coverage Θ relates to the clean ratio via:

$$r_{\mathrm{LH}} = r_{\mathrm{LH}}^{\mathrm{B}} \, \frac{(1 - K_{\mathrm{L}}\Theta)}{(1 - K_{\mathrm{H}}\Theta)}, \tag{1.40}$$

which inverts to give the coverage directly from the measured ratios and attenuation lengths:

$$\Theta = \frac{r_{\mathrm{LH}}^{\mathrm{B}} - r_{\mathrm{LH}}}{r_{\mathrm{LH}}^{\mathrm{B}} K_{\mathrm{L}} - r_{\mathrm{LH}} K_{\mathrm{H}}} \,. \tag{1.41}$$

For determining monolayer coverage, a more practical method, as described by Rogers and Rhead (1990), involves the plotting of the ratios of the Auger p-p intensities of the substrate and adsorbate as a function of deposition time. Under layer-by-layer (Frank–van der Merwe) growth (Kolasinski, 2012) these traces are piecewise linear, and the completion of each monolayer appears as a clear change in slope, as can be seen in Figure 2.20, linking successive linear segments.

This can be explained by the fact that, under layer-by-layer growth, deposition first fills the current monolayer, so the substrate signal decreases and the adsorbate signal increases at an approximately constant rate. Once the layer is complete, further deposition begins a new layer on top, changing how strongly the substrate electrons are attenuated relative to the adsorbate signal. This transition from filling a layer to building the next produces the observed change in slope.

1.4.2 Low Energy Electron Diffraction

LEED is based on the elastic scattering of low energy electrons, in the range of 20 eV to 200 eV, which are directed towards a surface. In the ideal case of a crystalline surface, the regularly spaced atoms diffract and scatter the incoming electrons into distinct spots, which can be observed (Pendry, 1974).

In essence a LEED setup consists of an electron gun and a capturing mechanism to display the diffracted electrons. Electrons from the filament are shaped and collimated by a Wehnelt cylinder and an electrostatic lens assembly, then accelerated to the chosen energy and directed towards the sample. The elastically backscattered electrons leaving the surface enter a retarding field grid stack: the first grid is held at ground to shield the beam from fringe fields of the subsequent electrodes, while the second and third grids are biased slightly negative relative to the primary energy to reject inelastically scattered electrons. The elastically diffracted electrons then traverse a final grounded grid and impinge on a multichannel plate for amplification, after which the electron diffraction pattern is made

visible on a phosphor screen (MacRae, 1963).

Due to the wave particle duality, the electrons exhibit a wavelength (λ) given by:

$$\lambda = \frac{h}{m_e v} = \frac{h}{\sqrt{2 m_e E_P}} \tag{1.42}$$

where h is Planck's constant, m_e is the electron mass, v is the electron speed, and E_P is the kinetic energy of the electrons from the electron gun.

For scattering from a periodic array with lattice spacing (a), constructive interference occurs when the path difference between waves from adjacent sites equals an integer multiple of the wavelength. This is described with the grating Equation 1.21, and substituting Equation 1.42 into it:

$$\sin\theta = \frac{n\,\lambda}{a} = \frac{n\,h}{a\,\sqrt{2 m_e E_P}}, \qquad n \in \{0, 1, 2, \ldots\}, \tag{1.43}$$

where θ is the angle of the scattered electrons relative to the surface normal, n is the diffraction order, and a is the nearest-neighbor spacing.

As the method employs low-energy electrons, their short IMFP ensures that the diffraction pattern arises from only the topmost atomic layers, making LEED a highly surface-sensitive probe. On an ideal, well-ordered surface the diffraction spots are sharp and well defined, reflecting long-range periodicity in the topmost layers. Disorder, defects, or partial reconstructions broaden or diffuse the spots, providing a straightforward diagnostic for deviations from perfect order. This means that even minor modifications in surface ordering or adsorption can significantly alter the resulting diffraction pattern.

Adsorbates commonly modify the surface periodicity. LEED reveals these changes through superstructure spots, spot splitting, or symmetry changes. Such signatures are used to confirm adsorption-induced reconstructions and to infer how the surface potential and atomic arrangement have been altered (Hove and Somorjai, 1994).

The preceding chapter established the physical framework that underpins this work. With this theoretical basis in place, the discussion now turns to the experimental design. The

vacuum layout, optical ray tracing, and surface preparation procedures are described first, followed by the calibration strategy used to reliably probe the electronic structure of manganese and manganese oxide nanoparticles.

Chapter 2

Novel HHG Experimental Setup and its Characterization

Investigating the electronic structure of manganese and manganese oxide nanoparticles with ultrashort laser pulses necessitated the construction of a custom HHG beamline. This light source provides access to XUV light, which tunes the kinetic energy of the emitted electrons to the region of the shortest electron mean free path. This is required to isolate the surface electronic states of the investigated nanoparticles from the bulk substrate. The construction and the progression of the experimental build becomes the central theme of this chapter: the design developments are presented first, following the chronological sequence of the build. Lastly, the molybdenum surface and magnesia thin film preparation, as well as the deposition of manganese, is detailed.

2.1 Vacuum and Chamber Design

The following section details the vacuum layout and chamber design, highlighting the engineering challenges resolved by the custom setup. The chamber's design is based on a blueprint kindly provided by Vaida and Leone (2016), which served as the robust foundation for the refined design presented in this work.

2.1.1 Vacuum Plan

Care was taken to develop a fail safe vacuum plan, which would protect the very costly optics at all times. An electrical design was constructed in house by G. Bräth, which entails the roughing pumps and turbomolecular pumps running on an independent power supply from the experimental system.

The vacuum system, as shown in the vacuum plan in Figure 2.1, is divided into four logical vacuum partitions. The chambers (1), (2,3,4), (5,6) are physically separated by a vacuum gate valve. The fourth partition spans the pumps for the gas line and rotary feedthrough of the surface science chamber. The equipment of these partitions is running on four separate electrical fuses, so that in the event of an equipment failure, only one segment of the apparatus is affected.

In the event of a power outage or phase failure, the affected system is brought to a safe state and unwanted re-powering is prevented. Additionally, with the addition of vacuum safety

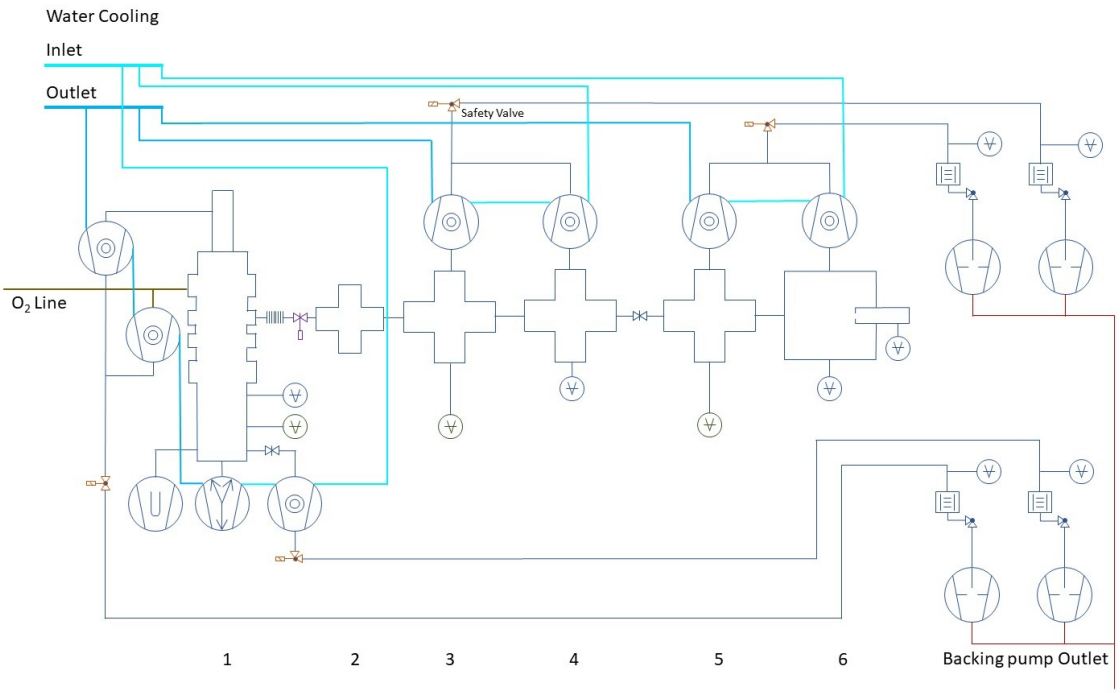


Figure 2.1: Schematic of the vacuum plan. the experimental setup is composed of six primary vacuum chambers, arranged from left to right: (1) surface science chamber, (2) pump beam injector chamber, (3) toroidal mirror chamber, (4) diagnostics chamber, (5) grating chamber, and (6) HHG chamber.

valves (Leybold Secuvac), which were placed into the roughing vacuum lines, shock venting or flooding of oil from the backing pumps into the chambers is prevented. The valves automatically detect power loss and pressure gradients, causing the valve to automatically shut and protect the vacuum, while subsequently venting the roughing lines.

2.1.2 Mechanical Design

With the physical and electrical design settled, Figure 2.2 shows the drafted Computer-Aided Design (CAD) to depict the complete beamline setup to easily identify the geometries for the optical design. The blue elements depict the gate valves, which separate the three vacuum partitions.

Custom-machined vacuum separation apertures (indicated in red in Figure 2.2) are machined into ConFlat (CF) 63 flanges which are installed along the beamline to limit vacuum conductance. The design is shown in Figure 2.3, which features a removable aperture disk (green) that can be set to diameters of 30 mm, 20 mm and 15 mm. This disk is held in place by a threaded plug (red) that screws in to secure it. This is necessary to isolate the high-pressure HHG chamber (6), which operates at 10^{-3} to 10^{-4} mbar, from the surface science chamber (1), which must be maintained at an ultra-high vacuum (UHV) pressure in the order of 10^{-10} mbar. For the experiments, the 15 mm aperture is used, as it caused no clipping to the light beam and enabled the lowest vacuum conductance.

Another custom beamline component is the HHG gas tube, shown in Figure 2.4, with a

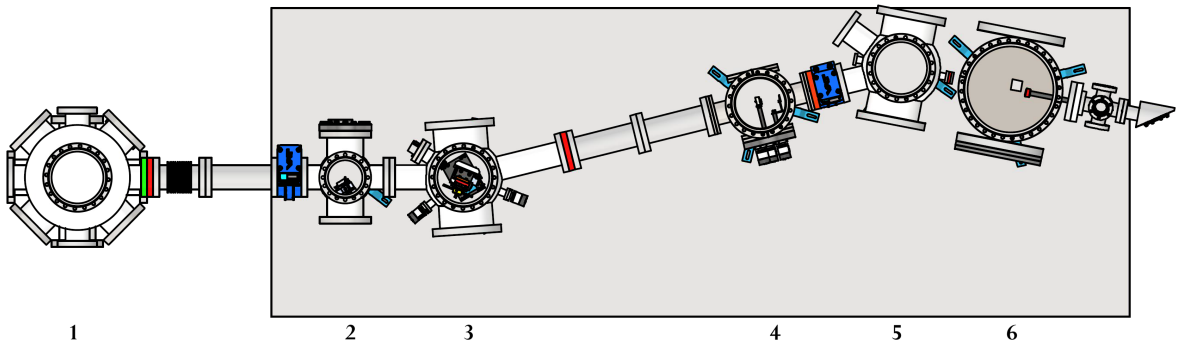


Figure 2.2: CAD design of the vacuum chambers. (1) surface science chamber, (2) pump beam injector chamber, (3) toroidal mirror chamber, (4) diagnostics chamber, (5) grating chamber, and (6) HHG chamber.

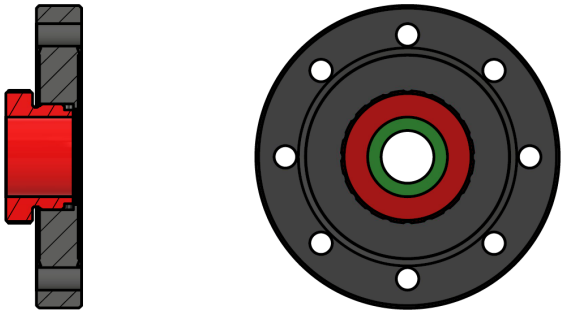


Figure 2.3: Technical drawing of the vacuum separation aperture, machined into a CF63 flange. Depicted in red is the screw ring holding the aperture, which is shown in green.

Brewster entry window depicted in the technical drawing in Figure 2.5 and in the experimental setup in Figure 2.6, which is discussed next.

2.1.3 Design of the Semi Infinite Gas Cell

For HHG, the laser is focused into a gas cell, isolated from the main vacuum system. This is achieved with a thin aluminum foil, shown in light grey in the magnified inset of Figure 2.4. The laser beam burns a small spot through the foil, that acts as an exit window, allowing the generated harmonics to pass into the beamline while separating the high-pressure gas from the vacuum. This gas cell assembly attaches to the large HHG chamber (6) via a

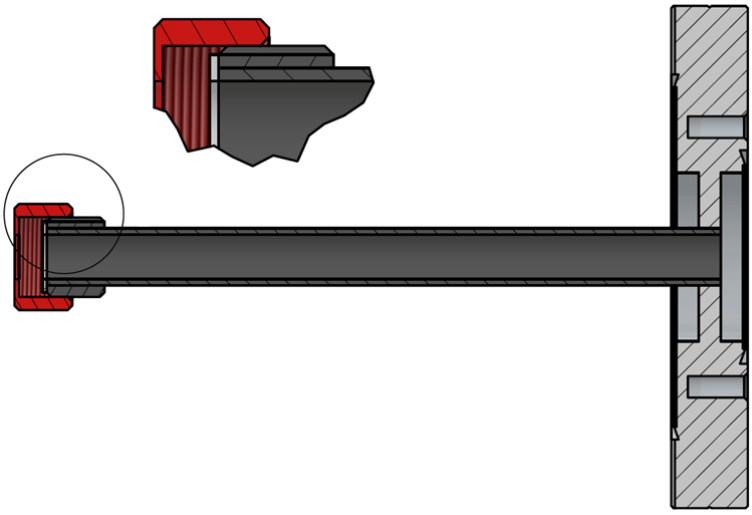


Figure 2.4: Technical drawing of the SIGC, the gas-filled tube for HHG. Inset: magnified view of the screw cap holding the aluminum foil that separates the gas-filled chamber from the vacuum.

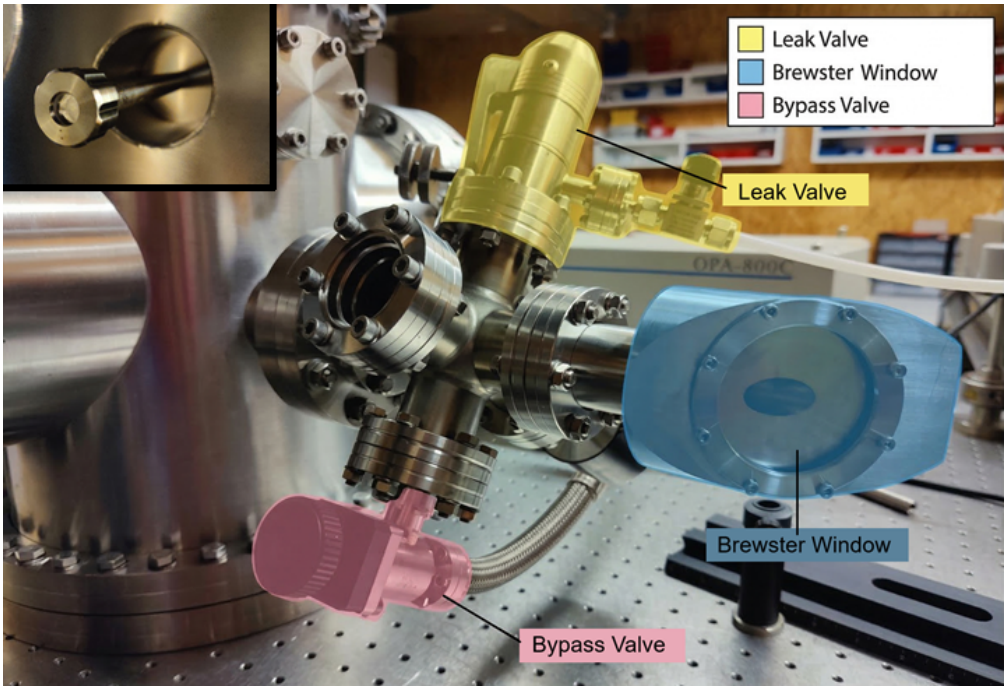


Figure 2.5: Start of the SIGC at the HHG 6-way cross, showing the gas inlet via leak valve, Brewster window, and bypass valve. Inset: End of the SIGC, with the gas tube from Figure 2.4.

CF 63 flange on the side. The other end connects to a 6-way CF 35 cross (Figure 2.5), which accommodates the Brewster window, a baratron for pressure monitoring, the gas inlet by a leak valve, and a bypass line for pumping the cell when not in use.

The Brewster window was engineered by Torr Scientific to minimize reflection losses for the p-polarized laser light. The Brewster's angle (θ_B) is given by Brewster's Law:

$$\theta_B = \arctan\left(\frac{n_2}{n_1}\right) \tag{2.1}$$

where n_1 is the refractive index of the surrounding atmosphere and n_2 is the refractive index of the window material. For fused silica at 800 nm wavelength, $n_2 = 1.4533$ and for air n_1 approximated with 1, the Brewster's Angle is roughly 55°.

In front of the Brewster entry window is a delay stage equipped with a 50 cm focal length lens, used to position the focal point of the 800 nm fs-laser near the aluminum foil exit window of the HHG SIGC.

With the mechanical geometry fixed, these constraints established the allowable optical

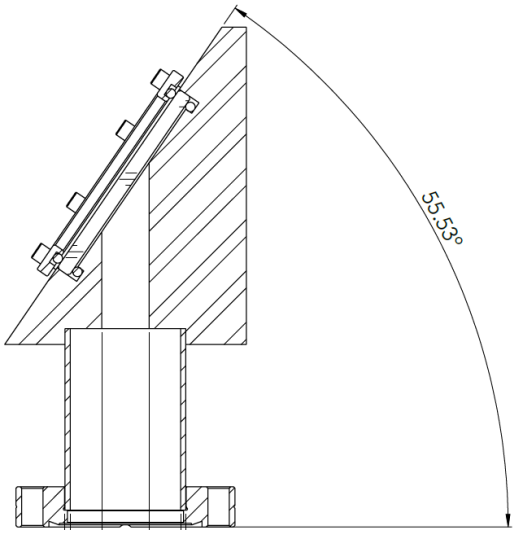


Figure 2.6: Brewster CF 35 flange by Torr Scientific Ltd.

path lengths and clearances. Combined with the parameters of the laser system, which are detailed in the next section, they provide the necessary input for the ray-tracing simulations presented thereafter.

2.2 fs-Laser System

The femtosecond laser system employed in the experiments is based on a Ti:Sapphire architecture and is described in detail in Vaida (2010). The key elements of the system are briefly outlined here. A continuous-wave Nd:YVO_4 laser (Spectra-Physics (2026) Millennia, 532 nm, 6 W) pumps a Ti:Sapphire oscillator (Spectra Physics Tsunami), which delivers pulses with a 35 fs duration, centered at 800 nm with a bandwidth of 60 nm a repetition rate of 77 MHz, and an average power of 500 mW.

The oscillator output is subsequently amplified using a chirped pulse amplification scheme in a regenerative Ti:Sapphire amplifier (Spectra Physics Spitfire XP), pumped by the second harmonic (527 nm) of a Q-switched Nd:YLF laser (Spectra Physics Empower). The amplified output beam, which is used to drive the HHG experiment, has a central wavelength of 800 nm, a pulse duration of 35 fs, a repetition rate of 1 kHz, and an average power of 3.5 W.

2.3 Raytracing of the HHG XUV Beamline

The high-harmonic beamline was designed and toleranced with a ray-tracing code RAY provided by Schäfers (1996) and RAY-UI (Baumgärtel et al., 2016). The point source of the HHG system is defined at the exit of an Argon-filled SIGC inside a gas-filled tube, where the coupled 800 nm driving laser is focused to an intensity of 10^{14} to 10^{15} Wcm^{-2}.

While multiple odd harmonics are observed, clear spectral signatures are resolved for the 9^{th} to 27^{th} orders, which will be discussed in Section 2.4.

Located 360 mm from this point source, a blazed diffraction grating spectrally disperses the generated harmonics. Further along the beamline, a toroid at 1680 mm from the focal point refocuses the diverging beam to a spot size of 200 µm. This is followed by a slit (Figure 2.2 green flange), 2 mm wide by 5 mm high, which is positioned 2590 mm from the source. Finally, the beam propagates onto the experimental surface located 2806 mm from the source. This configuration is summarized in Table 2.1.

Given the mechanical constraints, the optical train was optimized for flux, and wavefront quality with the program defining the mirror parameters 1 and 2 for the toroid.

Table 2.1: Specifications of the plane grating and the toroidal mirror.

Optical element	**Unit**	**Plane Grating**	**Toroidal Mirror**
Function	–	monochromatize	focus
Optical surface size	mm^2	40 × 40	50 × 30
Distance to source	mm	360	1680
Distance to preceding element	mm	360	1320
Bulk material	–	Si	Si
Roughness	nm	0.3	0.3
Slope σ mer./sag.	arcsec	0.1 / 0.1	0.5 / 1
Entrance arm hor./ver.	mm	–	827 / 827
Exit arm hor./ver.	mm	–	788 / 788
Mirror parameter 1	mm	–	R = 8530
Mirror parameter 2	mm	–	ρ = 98.4
Graz. incidence angle	deg	–	7.0
Total deviation angle	deg	155	166
Energy range	eV	10 – 17 / 29 – 32	–
Grating lines	1/mm	350 / 700	–

2.3.1 Material Selection for the Optical Elements

As listed in Table 2.1, silicon was selected as the bulk material for the optical elements. Comprehensive reviewing of adequate materials has been performed. Figure 2.7 shows the reflectance of select materials across the relevant energy range, calculated at a 12.5° grazing incidence angle. This angle, corresponding to the grating's least favorable position, serves as a worst-case calculation, since rotating the grating for harmonic selection only moves it towards more favorable angles. The reflectance values have been calculated with REFLEC, another tool by Schäfers (1996), with respect to p-polarized reflectance.

As discussed in great detail by Vaida (2010), experiments are conducted with p-polarized light as it creates a spatially uniform electric field near the sample surface. This uniformity is crucial for the experiment by avoiding a varying light coverage that s-polarized light would cause, due to interference of the incoming and outgoing light beam.

Considering the high reflectance and overall stable value, silicon has been chosen as the optical bulk material. Further coating would have increased cost, which was not desired. Silicon oxidizes, but no further than 2 nm, as detailed by Bohling and Sigmund (2016). Therefore, the calculation for silicon has been included above with a 2 nm SiO_2 layer to

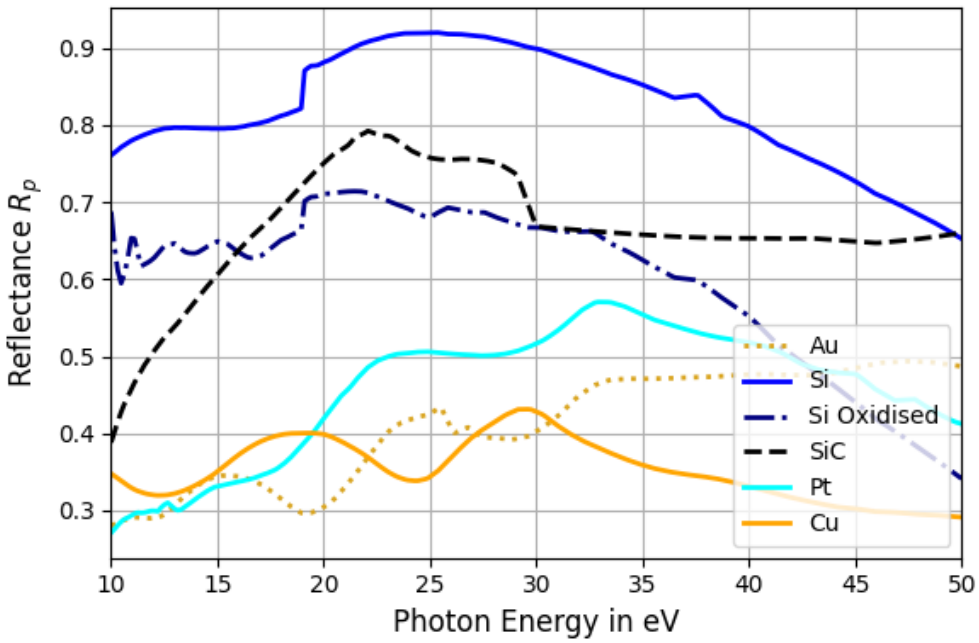


Figure 2.7: Reflectance of different materials at 12.5° grazing incidence angle.

attain a more realistic representation of the performance.

2.3.2 Diffraction Grating

The experimental setup utilized a dual-line grating, seen in Figure 2.8 and 2.9, featuring 350 and 700 lines/mm to maximize the intensities of the low (10 eV to 30 eV) and high (15 eV to 50 eV) energy spectral regions. See Figure A.3 in the Appendix for calculated reflection efficiencies for the corresponding line densities. Calculations with RAY-UI showed a 7.5 mm separation of harmonics for the 350 lines/mm grating and 15 mm for the 700 lines/mm grating. At the 2 mm slit situated before the surface science chamber, the HHG beam has a calculated width of 1 mm. It therefore cleanly isolates the desired harmonic while effectively suppressing neighboring harmonics.

Based on spot size calculations performed with RAY-UI at a 12.5° incidence angle, a maximum grating area of 30 × 30 mm was defined for the dual-track configuration. The final mechanical specifications were established in consultation with the silicon substrate supplier, PILZ OPTICS. The substrate thickness and clamping dimensions were optimized to ensure mechanical stability and minimize the risk of fracture during handling.

Because of the highly specialized nature of blazed gratings, the patterning and etching of

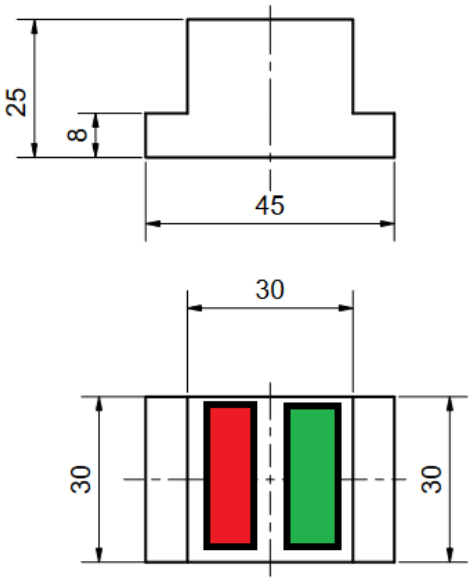


Figure 2.8: Technical drawing of the dual track (350 (red) and 700 (green) lines/mm) grating.

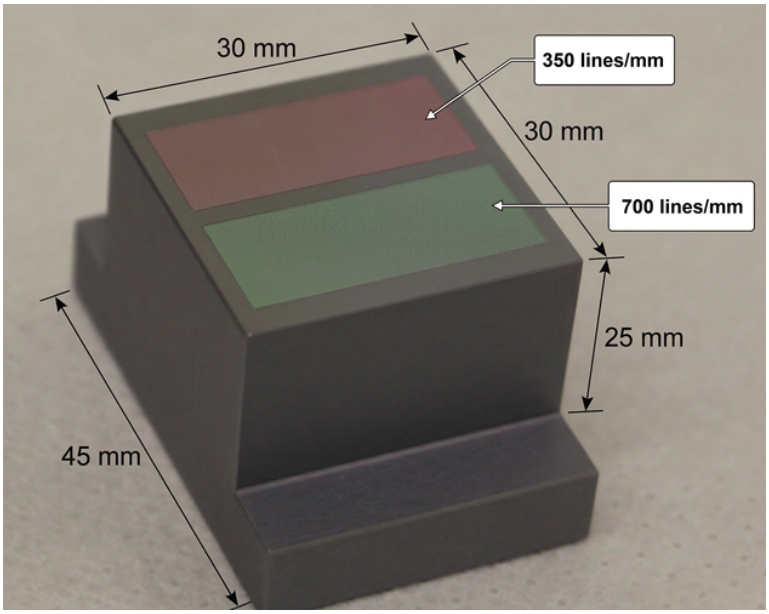


Figure 2.9: Diffraction grating with 350 lines/mm (highlighted in red) and 700 lines/mm (highlighted in green).

the provided silicon substrates were contracted to the Helmholtz-Zentrum Berlin (HZB). While the possibility existed to procure a grating from commercial suppliers, the exact blaze angle, grating dimensions, and desired dual track configuration would have not been available. Therefore, a custom solution was targeted. To avoid the extensive optical realignment required when swapping components, a dual-track configuration was selected. This approach also eliminated the logistical challenges and contamination risks inherent in handling, storing, and installing two highly sensitive gratings.

Using REFLEC simulations, the impact of blaze angle variation was analysed and it was determined that the optimal angles for both grating line densities fell within a compatible range. Based on this analysis and manufacturing expertise from the HZB Precision Gratings working group, a unified blaze angle of 3.6° was delivered. The complete information about the blaze angle can be found in Appendix A.

The production of the grating took place over several months under strict cleanroom conditions. The silicon substrate was first coated with a gold layer to serve as a mask. A two-axis precision ruling machine, operating in an environmentally isolated hutch, with strict vibration, temperature, and humidity controls, utilized a dynamically tilted diamond tool to shape the gold layer into the initial blazed line pattern.

Once the gold mask passed quality control, the pattern was transferred into the silicon substrate through ion beam etching in a vacuum chamber. Because gold and silicon have different etch rates, the final blaze angle was finely tuned through highly selective dry-etching processes.

The physical properties of the grating are ultimately constrained by the limits of the fabrication process. While standard soft X-ray gratings typically require blaze angles between 0.5° and 1.5°, this project required high blaze angles exceeding 3°. Operating at this manufacturing limit introduces specific geometric and surface constraints. At angles >3°, the blaze angle cannot be perfectly isolated and is subject to a wider manufacturing tolerance of ± 0.4°. Furthermore, because the etching results depend on the line density, slight variations in the final blaze angle between the 350 and 700 lines/mm tracks were expected.

Fabricating two distinct line densities on a single substrate carried the risk of requiring multiple production attempts; however, HZB successfully delivered the dual-track grating without compromising on quality. Exceeding expectations for such a challenging profile, they achieved the precise 3.6° blaze angle requested for both the 350 and 700 lines/mm tracks, perfectly fulfilling the beamline's specifications.

2.3.3 Toroidal Mirror

The final optical component of the beamline is the toroidal mirror, which serves to refocus the beam and to compensate for grating-induced divergence. The dimensions of the optic, shown in Figure 2.10, were defined via RAY-UI at 20 × 55 mm. The length is critical because the 7° grazing incidence angle significantly elongates the beam footprint along the optical axis. The setup utilizes a demagnification geometry. By placing the toroid further from the source (entrance arm length > exit arm length) than from the image plane, a reduction of the final spot size is achieved.

Similar to the dual-track diffraction grating, a highly customized manufacturing approach was mandatory for this component. Off-the-shelf toroidal mirrors could not meet the beamline's geometric and optical constraints. A toroidal surface is defined by two distinct radii of curvature, specifically by the meridional radius and the sagittal radius.

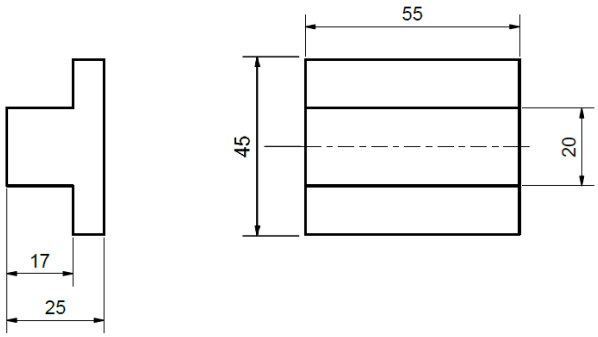


Figure 2.10: Technical drawing of the toroidal mirror.

To effectively eliminate astigmatism and focus the beam down to the desired spot size, both radii were precisely calculated with RAY-UI and manufactured to match the exact conjugate distances, defined by the specific entrance and exit arm lengths, at the designated 7° incidence angle. Commercial vendors do not stock optics with this exact intersection of customized radii and physical dimensions.

Furthermore, procuring a custom optic allowed for strict control over the surface quality, which is paramount in grazing incidence geometry. To minimize scattering losses and preserve the photon flux delivered by the grating, the mirror required exceptional surface finish tolerances. This necessitated advanced deterministic polishing techniques to achieve a minimal slope error and a micro-roughness in the sub-nanometer range of less than 1 nm rms. The specialized supplier PILZ OPTICS was selected for their proven expertise in this domain, successfully delivering an optic that met these stringent quality tolerances and ensured optimal reflectivity and beam uniformity at the final focal plane.

XUV Optical Holders

With the optical elements defined, the next step entailed the designing and construction the holders for the optics, depicted in Figure 2.11. This was a critical task because the significant length of the beamline imposes very strict alignment tolerances.

Given the distance between the grating and the surface probe of $L = 2446\,\text{mm}$, an angular

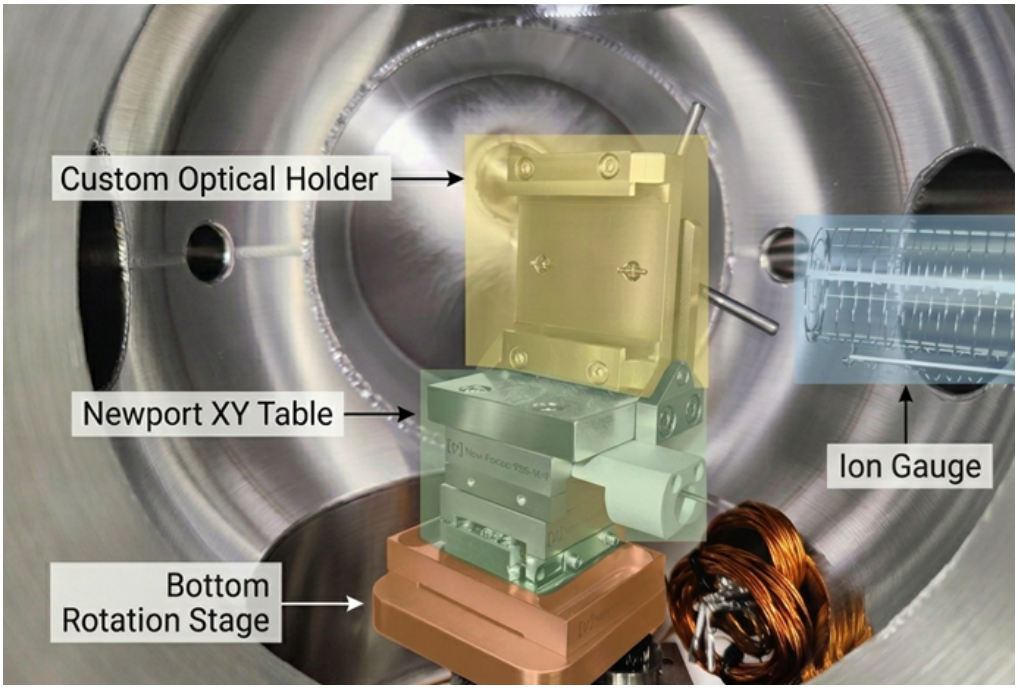


Figure 2.11: Custom optical holder assembly featuring a rotation stage, a Newport XY translation stage, and a toroidal top mount. An ion gauge for pressure measurements is also shown.

deviation of $\theta = 1^\circ$ leads to a lateral beam displacement (Δx) at the target of:

$$\Delta x \approx L \cdot \left(1^\circ \cdot \frac{\pi}{180^\circ}\right) \approx 2446\,\text{mm} \cdot 0.0175 = 42.7\,\text{mm} \tag{2.2}$$

To address this sensitivity, high-precision RSB30K rotation stages from Aurun Microelectronics are employed, which provide a fine step size of 0.012°. Seated on top of the stage, an X-Y table from Newport (9066-XY-M-R-V) is affixed to handle lateral positioning.

The top mount itself is a custom design fabricated by the university's workshop. It secures the optic using Teflon clamps to prevent damage to the substrate while allowing for yaw rotation. Both holders share this design, with one exception: the grating holder includes a vertical adjustment screw. This mechanism allows one to raise or lower the optic to access both line densities on the dual-line grating.

Initial Alignment of XUV Optics

The first phase of the alignment of the beamline was performed at atmospheric pressure using stainless steel replica optics. These replicas featured engraved center lines to aid

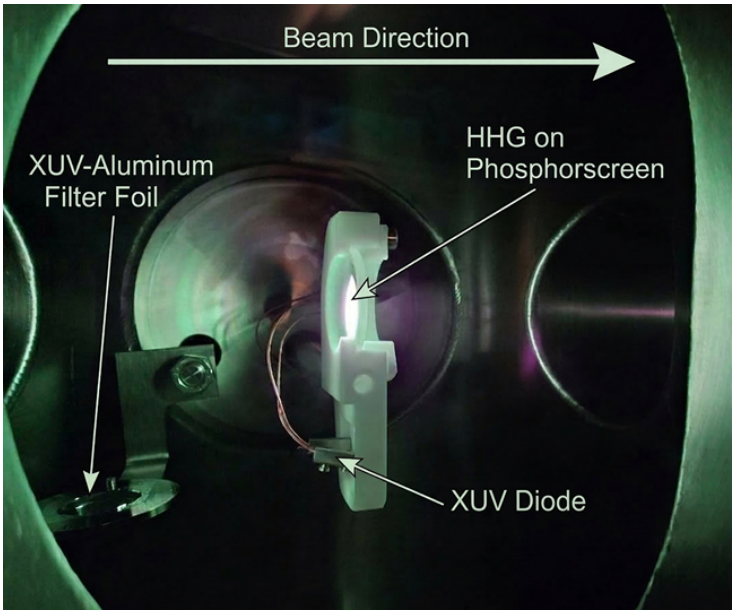


Figure 2.12: Diagnostic chamber with phosphor screen, XUV diode and XUV–aluminum filter foil. The HHG beam is clearly visible on the phosphor screen.

in visual positioning. A laser pointer was placed into the core of the HHG tube to point outwards and fix the position of the mirror leading into the HHG chamber to establish the optical axis. After this, the 800 nm fs-laser was coupled into the chamber through this first mirror and the beam was aligned to strike the center of the replica grating. Using the X-Y tables, the beam was then steered onto the phosphor screen in the diagnostics chamber to verify the lateral position as demonstrated in operation with HHG in Figure 2.12.

Afterward, the beam was centered on the toroid, and finally steered onto the target surface. When the replicas were swapped for the silicon optics, the alignment remained robust, requiring only minor fine tuning of the rotation stages.

2.4 HHG Characterization

With the optical components in place and aligned, the focus shifted to the characterization of the HHG beamline. To understand the spectral output of the HHG source, a systematic characterization was performed by varying the grating angle and the laser focal position within the SIGC. The resulting harmonic yield, seen in Figure 2.13, was monitored by measuring the total photoelectron signal from the molybdenum (100) surface. During

these measurements the sample was held at a bias of -15 V, to improve the signal quality by accelerating low-kinetic-energy electrons towards the analyzer. At the zeroth order reflection of the grating, the grating angle was defined as zero degrees. Negative angle corresponds to the grating turned so that the first negative order reflections are transmitted through the beamline.

Initial tests were undertaken with Argon, followed by a switch to Xenon to validate the system's results across a second gas. A qualitative comparison of these spectra at a constant cell pressure of 25 mbar, presented in Figures 2.14 and 2.15, highlights the distinct signatures produced by each gas under identical experimental conditions. The data reveals a clear trade-off: Argon produces a spectrum extending to significantly higher harmonic orders of the 800 nm (1.5 eV) laser fundamental, whereas xenon yields much higher signal intensities in the lower spectral region.

In Figure 2.14 at the very bottom left at 2.9°, the 27^{th} harmonic can be identified, followed by further lower odd harmonics until the 9^{th} harmonic. The intensity distribution reveals a clear spatial dependence: higher order harmonics are favored when the focus is positioned within the gas cell, whereas lower harmonics are more prominent when the focus is shifted towards the aluminum filter. This can be explained due to the reduced path length through the gas, which minimizes the absorption of the lower energy photons.

This behavior is rooted in the fundamental atomic properties of the gases. Xenon, with its lower ionization potential ($I_p \approx 12.1$ eV), is more easily ionized than Argon ($I_p \approx 15.8$ eV) (Kramida et al., 2024). While this allows for a high conversion efficiency and a bright signal at lower energies, it also causes the gas to saturate at lower laser intensities. Essentially, the majority of the gas atoms become ionized before the laser pulse reaches its peak field strength, limiting the maximum photon energy that can be produced. In contrast, Argon can withstand higher laser intensities before saturation occurs, allowing the electrons to be accelerated to higher kinetic energies. The highest harmonic detected using Xenon is the 19^{th} harmonic.

Varying the focal spot of the laser relative to the exit window of the semi infinite gas cell revealed the expected behaviour as reported in literature (Sutherland et al., 2004). The

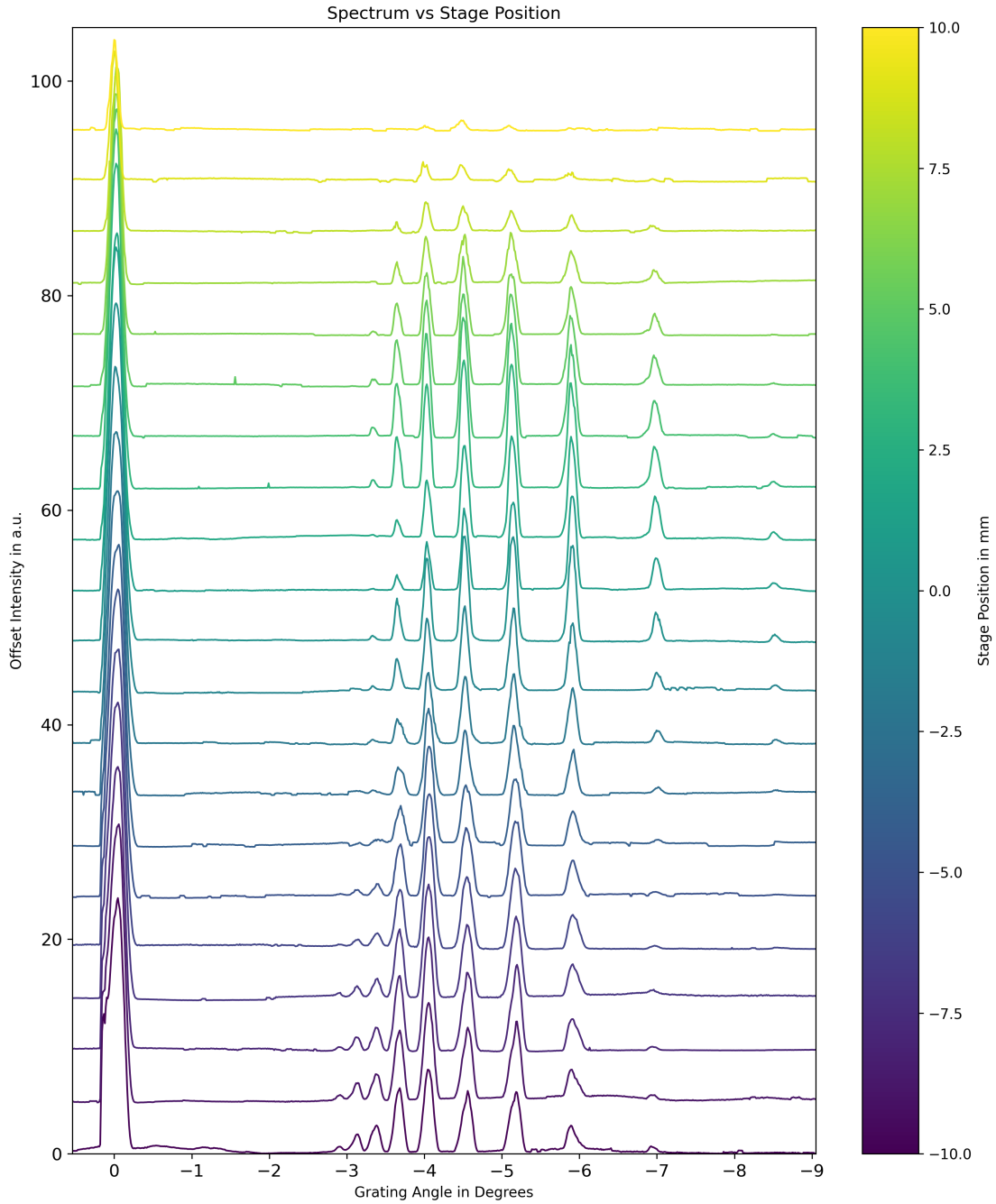


Figure 2.13: Argon HHG-spectrum as a function of laser focus position in HHG-cell and grating angle.

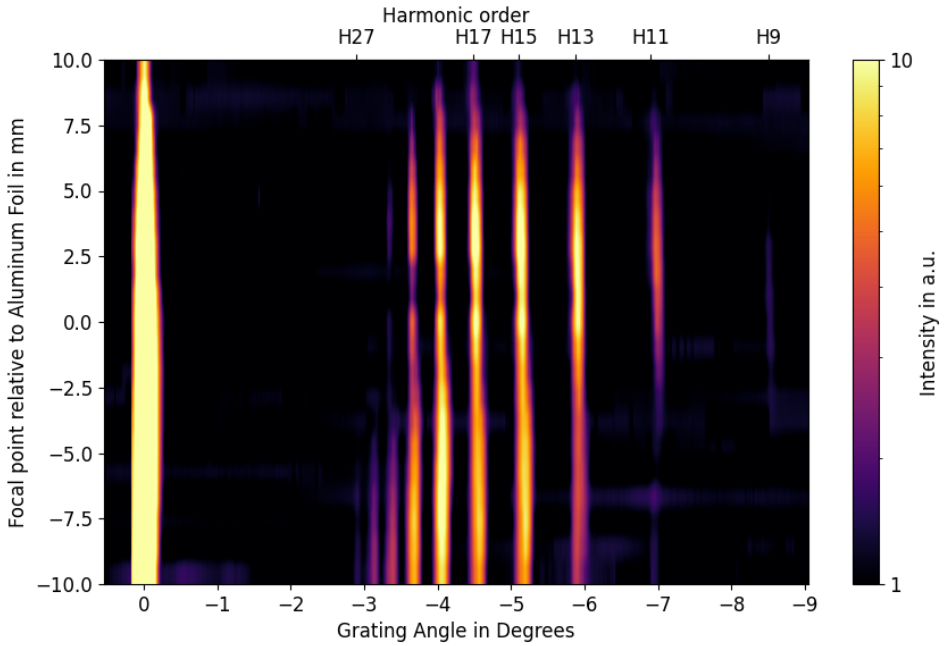


Figure 2.14: Heatmap of HHG-Generation in Argon as a function of grating angle and laser focus position.

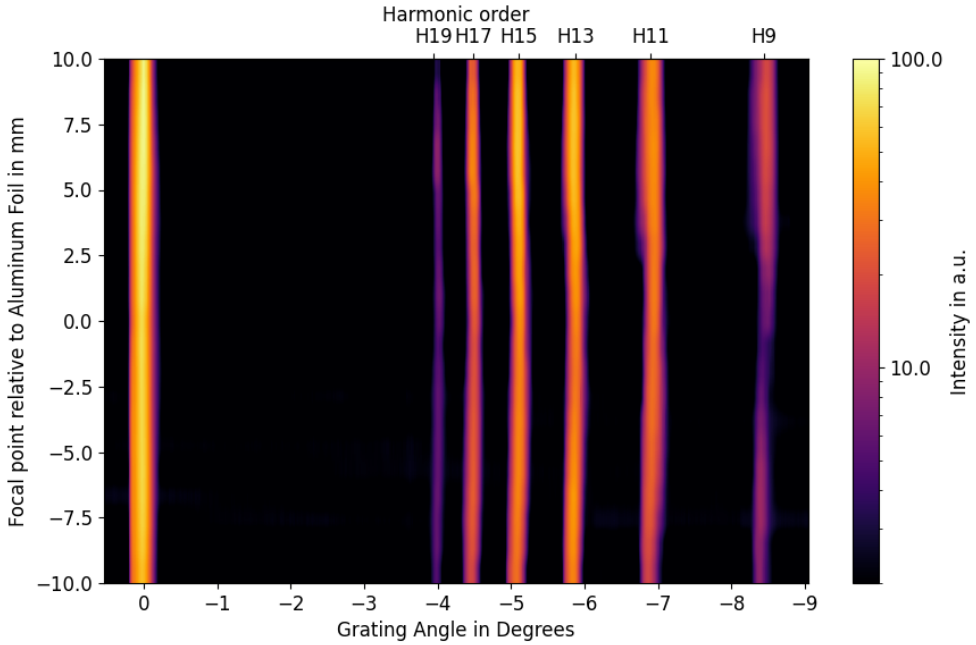


Figure 2.15: Heatmap of HHG-Generation in Xenon as a function of grating angle and laser focus position.

focal position resembles a tradeoff between generation efficiency and re-absorption.

When the laser focus is placed deep inside the gas cell, the high harmonics are generated within a dense medium, favoring the higher energy photons due to improved phase matching conditions. While the generation efficiency is high at the focus, these XUV photons must then propagate through the remaining length of the neutral gas to reach the exit. According to the Lambert-Beer law, the intensity of radiation decays exponentially as it travels through an absorbing medium. Since the neutral gas has a high absorption cross-section for XUV wavelengths, a focus placed within the cell results in significant signal loss (Constant et al., 1999). Essentially for the low energy photons, the gas re-absorbs the very photons it just created before they can escape into the vacuum. To mitigate this absorption, the focus is typically moved towards the exit of the cell. As the interaction region shifts closer to the vacuum interface, the path length through the neutral gas approaches zero, allowing the generated harmonics to escape without being attenuated.

The second tested variable was that of gas pressure. This is the primary variable for controlling phase matching. With increasing gas pressure, the HHG signal rises quadratically; however, this gain is eventually capped by two mechanisms: absorption and phase mismatch. The results of varying gas pressure at -1 mm focal position for the 23^{rd} harmonic are shown in Figure 2.16.

With increasing pressure, similarly to the focal position being far in the gas cell, the process enters the absorption-limited regime. As described by Constant et al. (1999), the coherence length of the process eventually becomes shorter than the absorption length of the medium. Beyond this critical pressure, adding more gas does not increase the output flux; instead, the generated XUV photons are re-absorbed by the medium faster than they are replenished. Therefore, the optimal pressure observed in the scans corresponds to the point where the medium is dense enough to maximize emitters but remains below the threshold where absorption and plasma-induced defocusing degrade the beam quality.

Phase matching is another critical factor of efficient High Harmonic generation. With increasing pressure, the density of neutral atoms raises the refractive index, while the concurrent increase in ionized gas atoms lowers it. Optimal generation occurs at a phase-

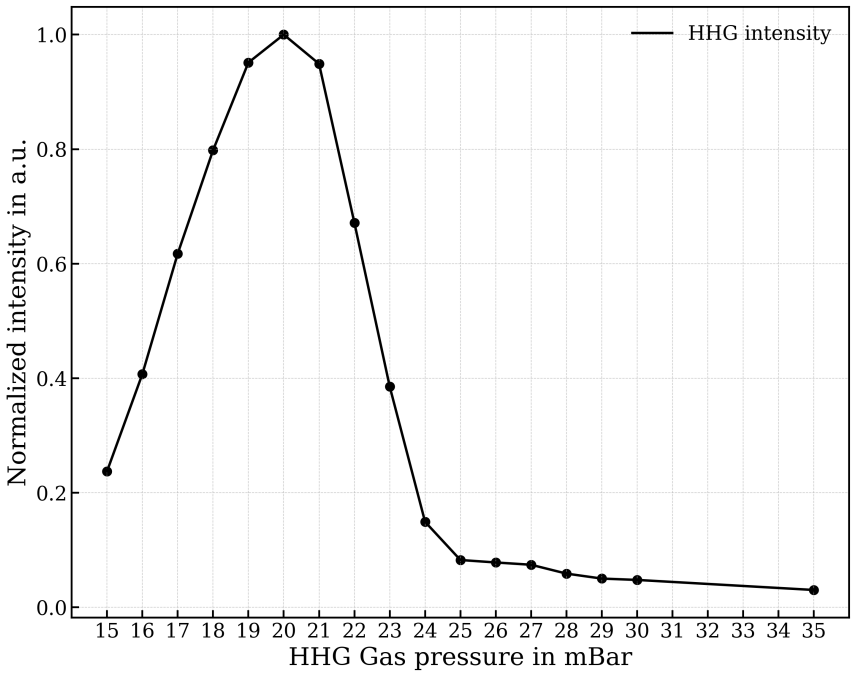


Figure 2.16: Measured beam intensity of the 23rd harmonic versus HHG cell pressure at -1 mm focal position relative to aluminum foil.

matching pressure where the dispersion from the neutral gas balances the dispersion from the free-electron plasma and the geometric Gouy phase (Salières et al., 1999).

2.5 Surface Preparation

2.5.1 Molybdenum Substrate

For this work, the experiments were conducted on a single-crystal molybdenum surface with a (100) orientation from MaTecK GmbH with a roughness of less than 0.01 µm, and a miscut of less than 0.4°. The metal was used as a substrate for the epitaxial growth of insulating magnesium oxide ultra-thin films, which serve as inert substrates for investigating the electronic structure of manganese and manganese oxide nanoparticles. This selection was driven largely by the extensive prior expertise established within the working group regarding this material system (Vaida et al., 2010).

The interface between Mo and MgO has been the subject of vast literature due to the high structural compatibility of the two materials (Benia et al., 2010). Both the Mo(100)

surface and MgO have a fourfold symmetry and a small lattice mismatch of 5.4% (Corneille et al., 1994). This relatively small lattice mismatch allows for the growth of high-quality, well-ordered oxide films, making the MgO/Mo system a classic prototype for studying metal-oxide interfaces (Xu et al., 1996).

A further reason for using molybdenum is its simplicity of cleaning in UHV. Unlike silver, which is also a candidate material for magnesia thin films (Wollschläger et al., 1998), the Mo(100) surface can be restored to a clean state primarily through thermal treatment, avoiding the need for repeated ion sputtering cycles (Santis et al., 2021). The standard cleaning procedure noted by Musket et al. (1982), involves cycles of annealing in oxygen at 1500 K, followed by rapid flashing to temperatures above 2000 K. This method is sufficient to desorb surface contaminants such as carbon, sulfur and oxygen.

Molybdenum Cleaning

Prior to experimental procedures, the new molybdenum surface underwent the cleaning treatment previously described. The surface was resistively heated to 1500 K in a $3x10^{-7}$ mbar oxygen background for 5 minutes with subsequent flashing to 2200 K.

Figure 2.17 depicts the Auger electron spectra acquired from the molybdenum surface, illustrating the spectra before and after the cleaning. The highlighted markers along the abscissa correspond to standard transition energies referenced from the Handbook of Auger Electron Spectroscopy authored by Davis et al. (1976). The clean substrate is characterized by the distinct molybdenum peaks located at kinetic energies of 186 eV and 221 eV. In contrast, the very first untreated spectrum recorded of a new Mo crystal, reveals an attenuation of the characterizing molybdenum peaks and a significant peak at 273 eV, which identifies the presence of carbon contamination prior to the cleaning treatment. The cleaning cycle was repeated on the order of fifty times to remove the visible contaminant signals in the auger electron spectrum.

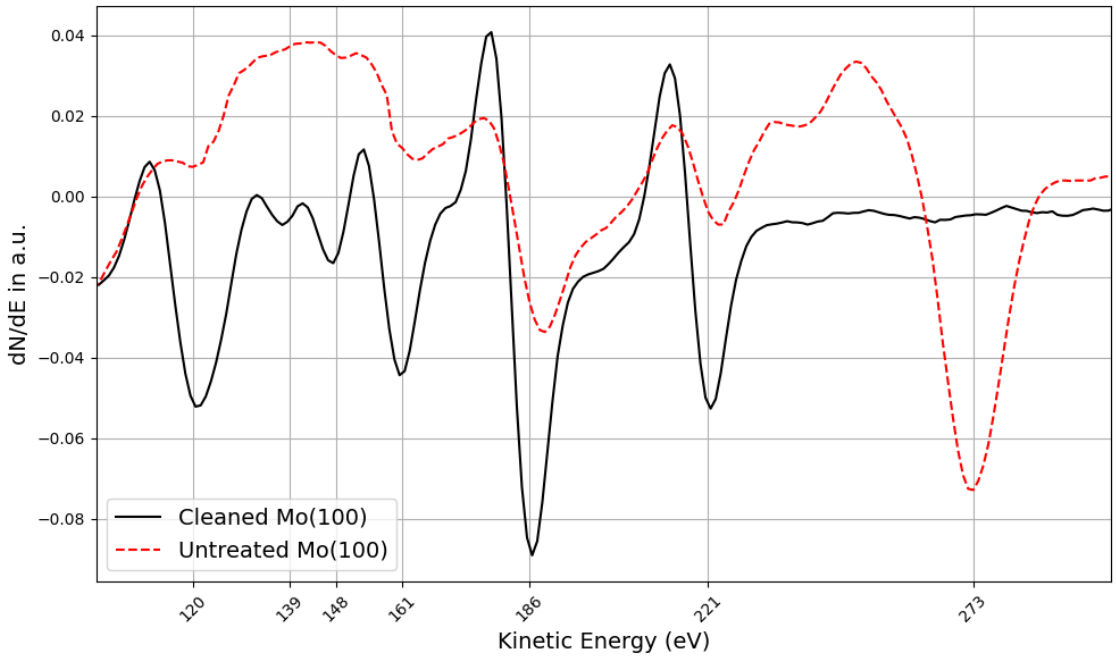


Figure 2.17: Auger Spectrum before (dashed red) and after cleaning (solid black) of the Mo(100) surface.

The surface quality is further characterized with LEED to ensure both surface cleanliness and structural integrity. Figure 2.18 shows an LEED image taken at 87 eV while the surface is held at liquid nitrogen temperature.

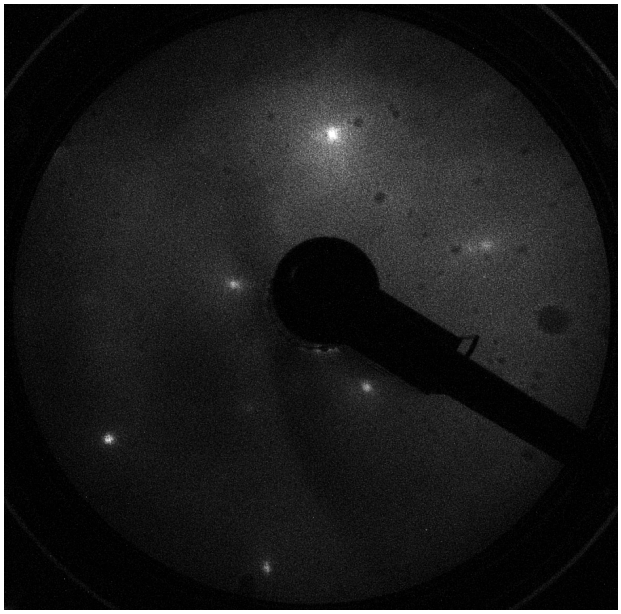


Figure 2.18: LEED pattern of clean Mo(100) recorded at 87 eV with the sample held at LN_2 temperature.

As previously reported by Wu et al. (1991); Vaida and Bernhardt (2010) the clean Mo(100) surface exhibits a sharp 1x1 diffraction pattern in LEED, indicating that the crystal lattice is periodic and free from amorphous contaminants.

2.5.2 Mg Oven Calibration and MgO Thin Film Preparation

With the cleanliness and crystallinity of the molybdenum surface verified, the magnesium deposition rate was first calibrated to ensure reproducible film preparation. Following the established procedures of the working group, based on the methods of Wu et al. (1991), magnesium is deposited onto the surface at liquid nitrogen temperatures. Using higher temperatures during Mg evaporation, directly lead to the desorption of the deposited magnesium, which proved to make calibration impossible.

Following the cooling of the surface, the surface is positioned directly in front of a Knudsen Evaporation Cell from Chell Instruments Ltd (2026), using a laser pointer to align the center of the surface with the opening of the thermal evaporator. The crucible is equipped with a 99.98% magnesium rod of 3 mm diameter from Mateck GmbH (2026). See Appendix B for XPS analysis of the purity of the magnesium.

The crucible was then heated to 300°C, which is measured using the internal thermocouple of the device. The temperature is held constant with a CAL 9900 PID Temperature controller (West Control Solutions Ltd, 2018). Prior to deposition, the set temperature was held for 10 minutes to ensure an uniform temperature profile within the evaporator.

After each deposition step of 20 seconds, an auger electron spectrum was recorded. This allowed for the simultaneous observation of the attenuation of the peaks of the molybdenum substrate and the growth of the magnesium peak, which is expected at 45 eV (Davis et al., 1976).

By using the method described in earlier Section 1.4.1, the peak-to-peak intensities of the 45 eV and 186 eV signals were put into ratio, to determine the completion of the first monolayer.

Quantifying the low-energy Mg signal presented a challenge because it overlaps with the tail of the Mo feature at 28 eV in the molybdenum spectrum. To ensure consistency, the

p-p amplitude is defined symmetrically around the signal's inflection point at 42.5 eV. By extending the measurement interval equidistantly from this center, thus spanning 40 eV to 45 eV, a quantifiable p-p distance is established for the Mg intensity.

Figure 2.19 shows the AES spectra acquired of the sample with respect to the deposition time. The characteristic molybdenum peaks at 28 eV, 186 eV and 221 eV show the expected attenuation, while the magnesium peak at 45 eV emerges.

The peak-to-peak ratios of the molybdenum substrate and the deposited magnesium were plotted as a function of deposition time. A least-squares linear regression was applied to the data. As shown in Figure 2.20, a breakpoint occurs at a deposition time of 110 seconds, indicating the completion of the first magnesium monolayer. The Mg calibration remains valid also for the magnesium oxide deposition rate. This is because the oxide forms via the insertion of oxygen into the interstitial sites between the Mg atoms. Since oxygen is supplied in excess, the final film thickness depends solely on the magnesium flux.

The successful calibration allowed for the reproducible deposition of 10 ML MgO films, acting as a substrate for the subsequent manganese experiments. This thickness was chosen to screen the molybdenum substrate, as the short inelastic mean free path of electrons at the apparatus' XUV wavelengths suppresses the substrate signal.

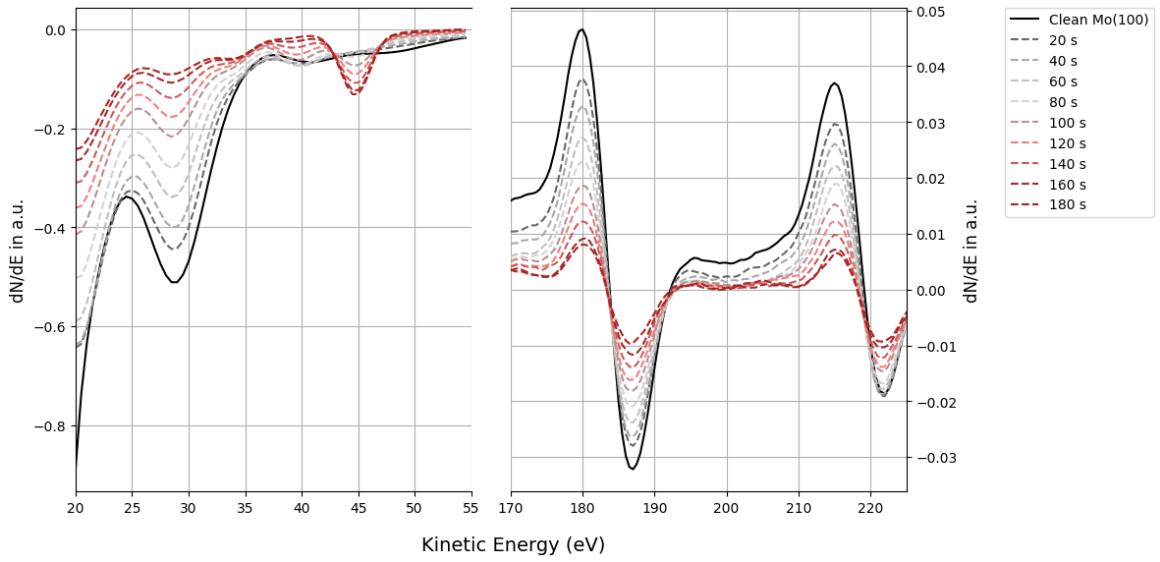


Figure 2.19: Auger Electron Spectra of molybdenum during Mg deposition.

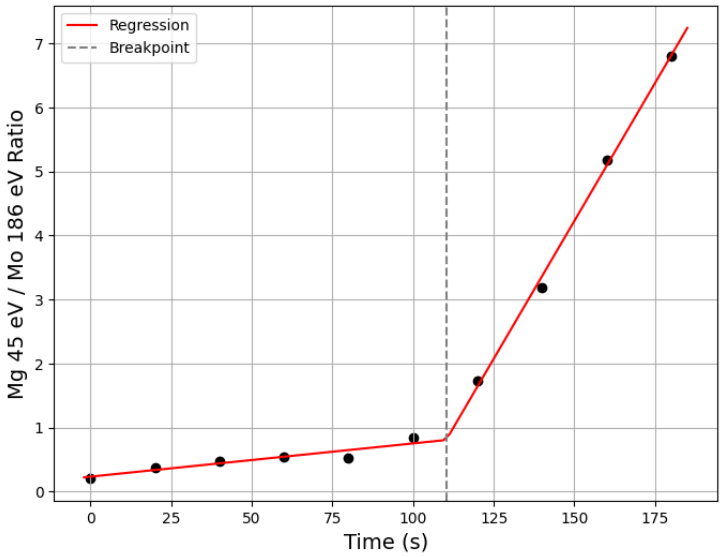


Figure 2.20: Plotted ratios of the AES peaks of magnesium and molybdenum as a function of deposition time.

The structural order of the 10 Monolayer Equivalent (ML) coverage was verified by LEED. As shown in Figure 2.21, the diffraction spots obtained prior to annealing appear diffuse, indicating a degree of disorder in the as-deposited film.

After annealing at 1000°C for 10 minutes, the diffraction spots become significantly clearer and sharper (Figure 2.22). This improvement confirms that the MgO film crystallizes and grows epitaxially on the Mo(100) surface, in agreement with previous findings by Vaida (2010) and Wu et al. (1991).

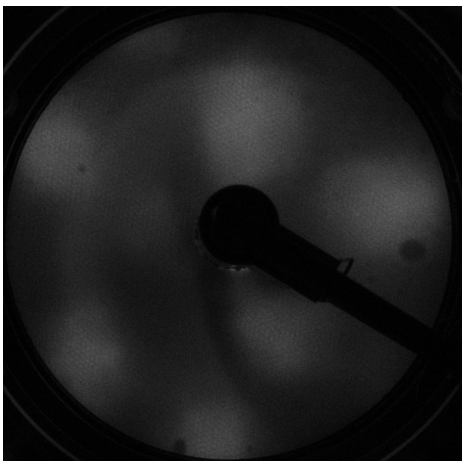


Figure 2.21: LEED pattern of a 10 ML MgO film prior to annealing, recorded at 87 eV with the sample held at liquid-nitrogen temperature.

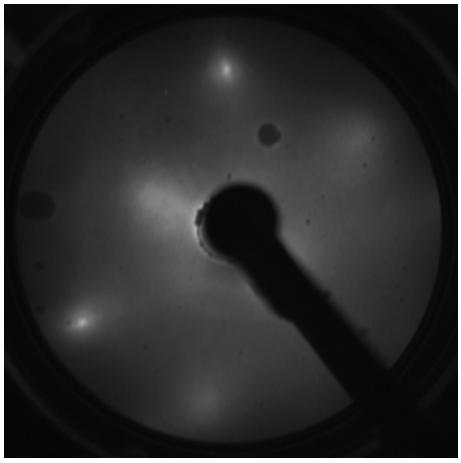


Figure 2.22: LEED pattern of a 10 ML MgO film after annealing, recorded at 87 eV at LN_2 temperature.

AES was recorded of the MgO thin film, which can be seen in Figure 2.23. The characteristic molybdenum peaks are strongly attenuated, while the Mg peak at 32 eV and the oxygen peak at around 500 eV are very pronounced, as presented for MgO in the Handbook of Auger Electron Spectroscopy Davis et al. (1976).

Additionally, a clean spectrum after flashing the Molybdenum crystal to 2000 K is shown in the same graph of Figure 2.23. Hence, the conclusion is reached, that MgO coatings can be removed and reapplied, providing a reliable reproducibility of the surface conditions between experimental runs.

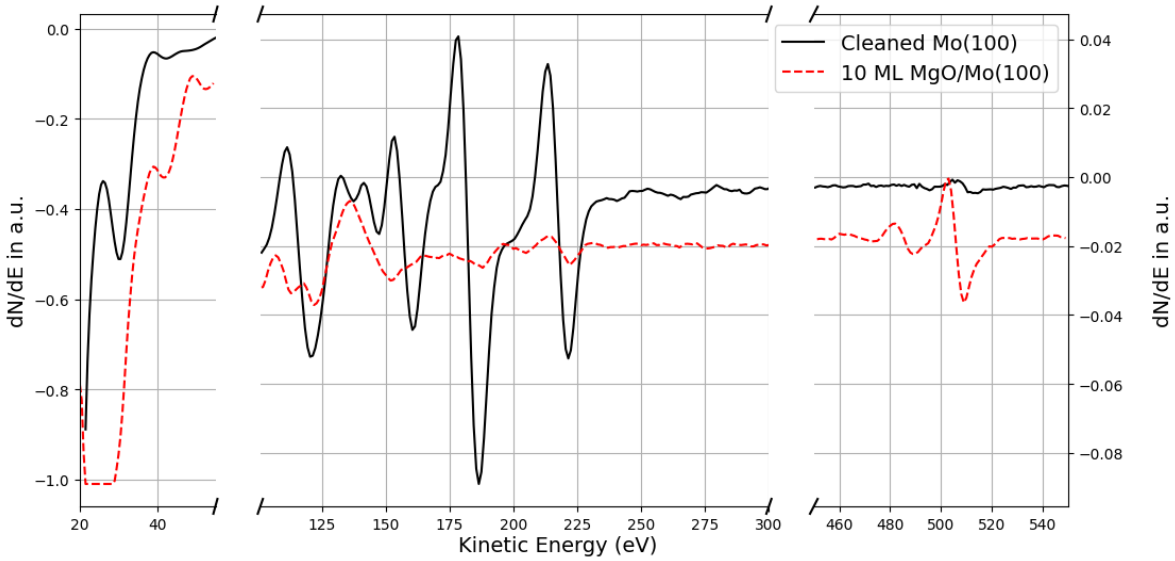


Figure 2.23: AES Spectrum after MgO Deposition (red dashed) and re-cleaning (black solid).

2.5.3 Mn Oven Calibration

Manganese is a transition metal with a wide influence on both the environment and industry. Its versatility comes largely from its ability to adopt multiple oxidation states, which allows it to drive various chemical processes (Greenwood and Earnshaw, 1997). Mn is a hard and brittle metal with a melting point of 1246°C and a boiling point at roughly 2061°C (Lide, 2000).

The manganese deposition was calibrated using the same method from the magnesium oven. An identical second Knudsen Cell from Chell has been equipped with 99,5% purity manganese rod with a 2 mm diameter from Goodfellow Cambridge Ltd (2026). See Appendix B for XPS analysis of the purity of the manganese.

Guided by the experimental conditions of Shukla et al. (2004) and Nayak et al. (2012), the Knudsen cell was held at 700°C using the same CAL 9900 PID temperature controller as the magnesium evaporator. After cleaning, the molybdenum substrate was cooled to liquid nitrogen temperature. Mn deposition was then performed in 1-minute steps, with the surface laser-aligned before each iteration while recording AES to document surface conditions. A Mn growth time of 5.5 min/ML was determined by least-squares regression of the peak-to-peak ratios of the molybdenum 186 eV and manganese 589 eV peaks.

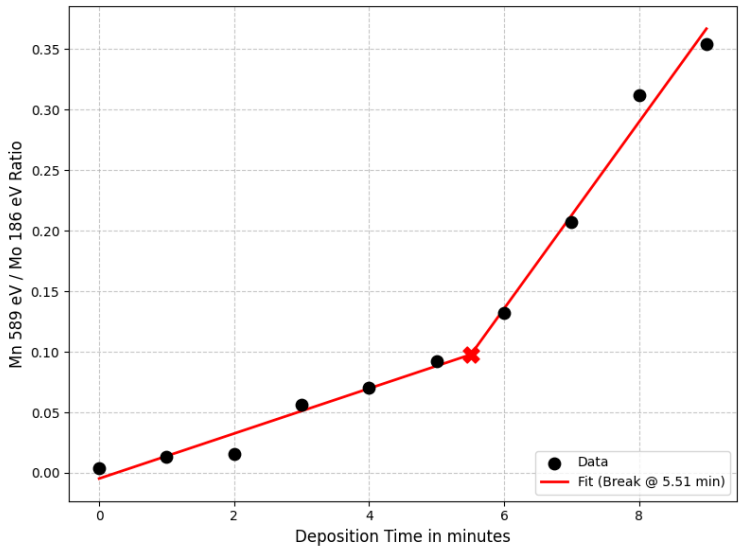


Figure 2.24: Plotted ratios of the AES peaks of manganese and molybdenum as a function of deposition time.

2.6 Integration of the Photoelectron Spectrometer

With the calibration of the evaporation sources completed, the focus shifted to the deployment of the photoelectron spectrometer, with which the electronic structure of manganese and manganese oxide nanoparticles was probed. A full disassembly of the instrument and cleaning of all parts was undertaken. Select parts were cleaned in an ultrasonic bath. The components were then dried in an oven at 300°C for an hour. Upon reassembly, all electrical connections were tested for continuity. To maintain a defined work function of the spectrometer, all internal components were coated with graphite.

2.6.1 MCP Detector of the PES

The spectrometer's microchannel plate (MCP) assembly, shown in Figure 2.25, operates on a potential gradient ranging from ground to +2.3 kV at the anode and was sourced from Photonis (2024). Consequently, signal extraction requires capacitive decoupling to isolate the high voltage from the measurement electronics. The corresponding circuit diagram is shown in Figure 2.26

The circuit is connected with a high voltage power supply HV, which provides the necessary supply for operation. This potential is applied across the microchannel plate stack through the MSP IN terminal and the MSP OUT, creating the gradient required for

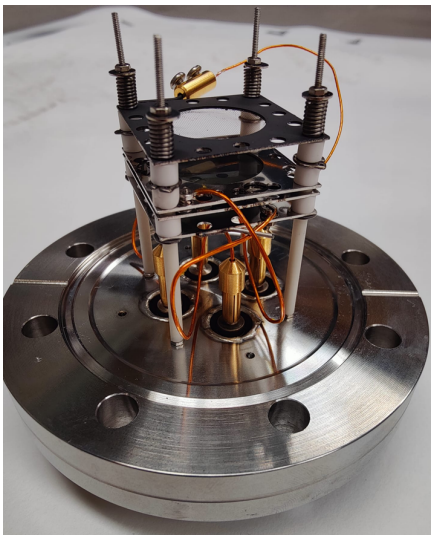


Figure 2.25: MCP stack of the PES detector.

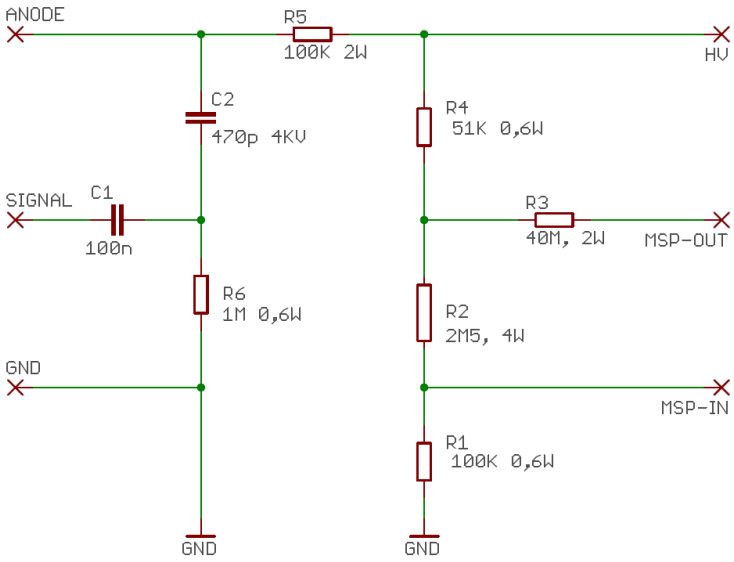


Figure 2.26: Initial MCP high voltage divider and signal decoupling schematic.

electron multiplication. The resulting multiplied photoelectrons are collected by the anode, which serves as the bottom plate of the PES detector. To extract the signal and protect the measurement electronics from the high voltage, the signal is decoupled with a capacitor. While the initial design implemented this decoupling using two capacitors C1 and C2, the design built for this work reduced the coupling to one capacitor to improve signal quality.

MCP Detector's Upgrade and Characterization

To understand the detectors count signal and to evaluate the performance of the decoupling network, impulse response measurements were performed. A low-intensity 400 nm laser beam was reflected off the sample surface into the detector to simulate a Dirac excitation (DIN, 2014), with the resulting signal traces captured using a Rohde & Schwarz (2025) MXO 4 oscilloscope.

In an effort to improve signal quality and reduce electrical noise, a voltage divider and decoupling circuit, as shown in the schematic of Figure 2.27, was custom designed with Surface Mounted Device (SMD) in this thesis. The finished PCB is shown in Figure 2.28. The design includes high quality ceramic C0G/NP0 capacitors from KEMET Electronics Corporation (2025) to minimize temperature drift and ensure a low equivalent series resistances. A compact layout of the components was chosen to suppress parasitic inductance.

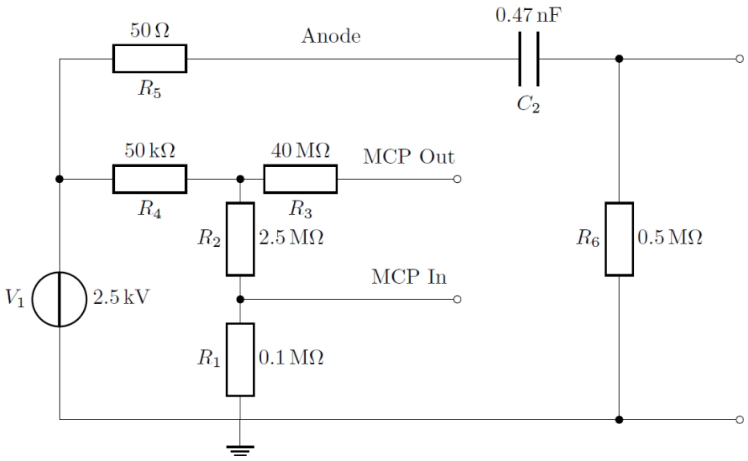


Figure 2.27: Updated MCP HV divider and signal decoupling schematic.

The dimension of the printed circuit board (PCB) with 35 mm × 45 mm, was chosen to mount directly onto the Miniature High Voltage (MHV) feedthroughs of the vacuum flange, eliminating the need for cabling.

The main difference, besides the removal of C1, is the change of R5 to 50 Ohm and R6 to 500 kOhms. The reasoning behind the adaption of R5 is the impedance matching of the circuit to the 50 Ohm measurement electronics. R6 was changed, as it reduces the time constant $\tau = R_6 \cdot C_2$ of the low pass filter. The capacitor C2 can charge faster, and the ringing of the circuit decays faster. This behaviour is shown by simulation in Figure 2.29. A 10 mV step was chosen to simulate the amplitude of the electron signal from the MCPs. The quicker decay of the 500 kOhm resistor is evident from the plot, decaying twice as fast as the 1 MOhm resistor. In the bode plot below, it is highlighted, that the 500 kOhm resistor dampens lower frequency signals more, while allowing the high frequency

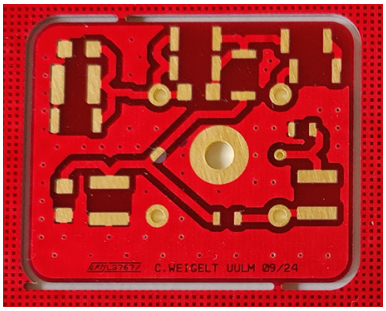


Figure 2.28: PCB of the custom HV divider and signal decoupler. The center hole allows for mounting to a case, whereas the other four smaller bores are to connect the PCB to the electrical feedthroughs.

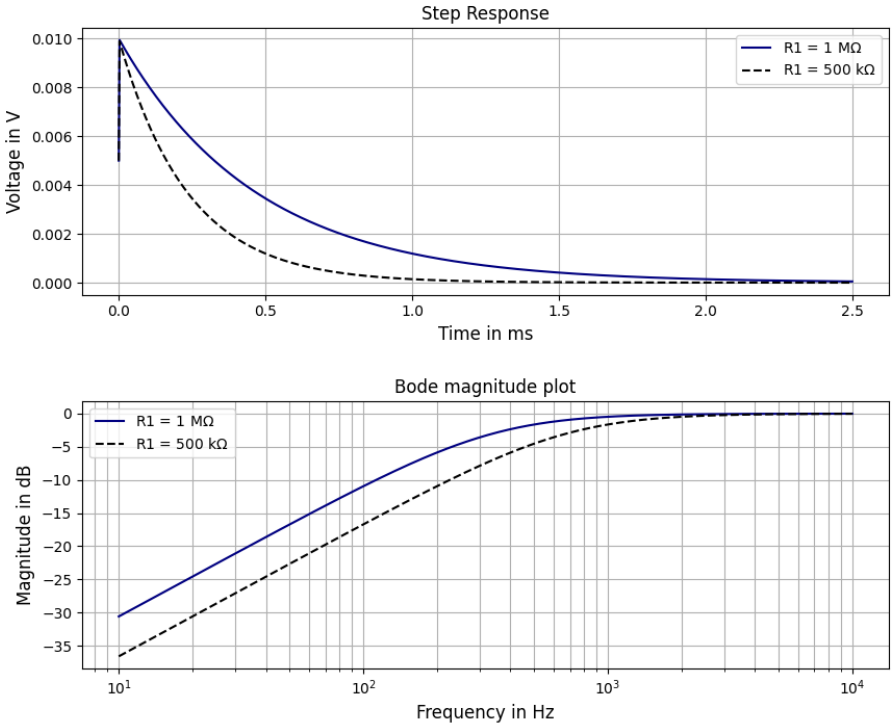


Figure 2.29: 10 mV step response and Bode magnitude plot of the decoupling circuit. The 500 kΩ configuration reaches steady state twice as fast as the 1 MΩ configuration.

components of the signal to pass with equal attenuation than the 1 MOhm resistor.

Figure 2.30 shows the impulse responses captured with the Rohde & Schwarz MXO 4 oscilloscope during the experiment, averaged over ten shots. The results show that the new PCB design reduced the ringing amplitude and has a narrower pulse width, indicating improved temporal resolution. Analysis reveals that the original circuit produced a peak-peak ringing amplitude of 7.6 mV with a Full Width at Half Maximum (FWHM) of the main peak of 2.08 ns. The optimized PCB circuit, on the other hand, achieved a reduced ringing peak-peak amplitude of 4.1 mV with a tighter FWHM of 1.95 ns.

The reduction of the strong negative transients is the most beneficial aspect of the new circuit, as it allows for a more sensitive count threshold of the detection electronics. The old circuit in such sensitive settings, would trigger the discriminator twice, leading to double counting. Thus, the overall sensitivity was enhanced without introducing detection artefacts.

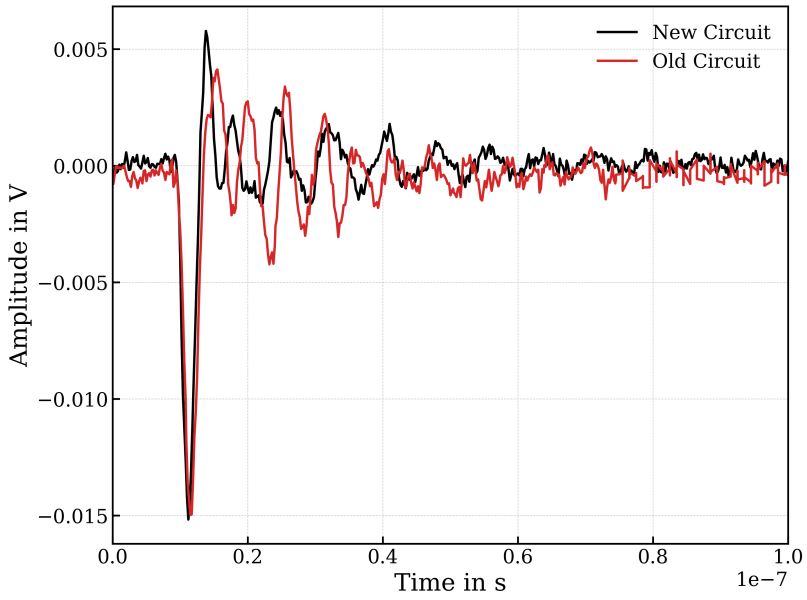


Figure 2.30: Experimental plots of the impulse response of the PES detector with the old (red) and new circuit (black).

2.6.2 PES Calibration for HHG

Following the procedure from Section 1.3.3, an initial calibration of the TOF spectrometer was performed with a monochromatic visible source.

To extend and cross-validate this calibration, the experiment was repeated by recording arrival times with HHG. Instead of varying the bias voltage in this case, the discrete, well defined photon energies of the HHG were used for calibration.

For the laser's fundamental wavelength of $\nu_1 = 800$ nm, the odd harmonics of order q has the photon energy:

$$E^{(q)} = q\, h\nu_1 \qquad (q = 1, 3, 5, \ldots) \tag{2.3}$$

where h is Planck's constant.

Measured arrival times of these harmonic peaks were then converted to the photon energy using the previously established TOF transfer Equation 1.26. A correction subtrahend was added to account for the kinetic energy gained from the bias voltage, while the energy lost due to the work function Φ was added:

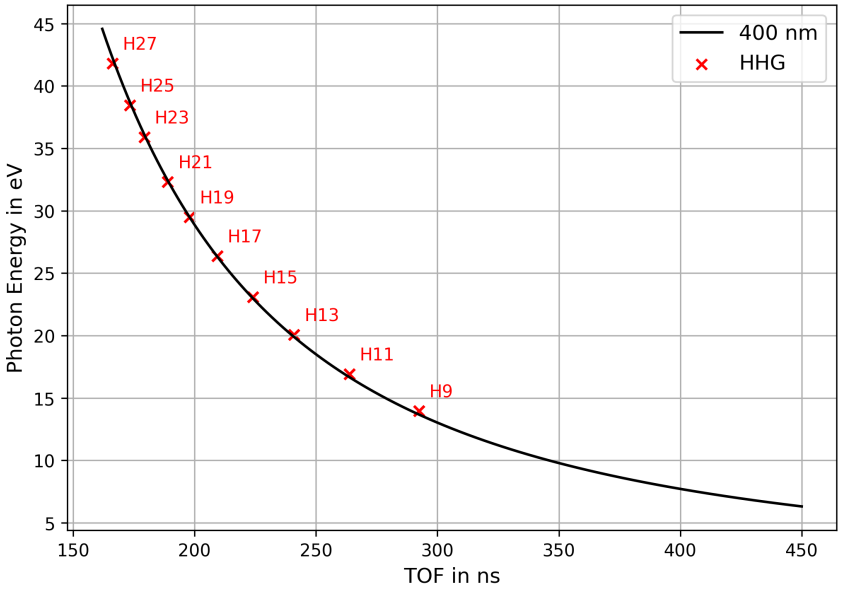


Figure 2.31: PES Calibration with 400 nm light while varying U_{bias} including overlayed HHG Calibration in the same plot.

$$E_{h\nu} = \frac{m_e L^2}{2e(t - t_0)^2} - U_{\text{bias}} + \Phi \tag{2.4}$$

where e is the elemental charge, to convert the answer to eV.

As depicted in Figure 2.31, the resulting HHG calibration both validates it against the visible light reference and simultaneously confirms the absolute photon energies of the accessible harmonics.

A mathematical mapping to convert raw TOF data into kinetic energy was created from this calibration, using below equations. One must not forget the intensity scaling with the Jakobian, as explained in Section 1.3.4.

$$E_{\text{kin}}(t) = \frac{m_e L^2}{2e(t - t_0)^2} - U_{\text{bias}} \tag{2.5}$$

$$I_{\text{E}}(E) = I_{\text{t}}(t) \cdot \frac{e(t - t_0)^3}{m_e L^2} \tag{2.6}$$

For the specific setup the mapping becomes:

$$m_{\mathrm{e}} = 9.11 \times 10^{-31}\ \mathrm{kg} \tag{2.7}$$

$$L = 0.59\ \mathrm{m} \tag{2.8}$$

$$e = 1.60 \times 10^{-19}\ \mathrm{C} \tag{2.9}$$

$$t_0 = 12.953\ \mathrm{ns} \tag{2.10}$$

$$U_{\mathrm{bias}} = 10\ \mathrm{V} \tag{2.11}$$

Following the completion of the chamber design, ray-tracing simulations, and initial alignment, the beamline is validated as operational. This is confirmed through the successful characterization of the spectra and the verification of expected HHG characteristics. With the beamline completed, the experimental setup was finalized by calibrating the deposition rates of the evaporation ovens, preparing the magnesia ultra-thin film surface, and deploying and calibrating the photoelectron spectrometer. The entire system is prepared for analyzing the electronic structure of manganese and manganese oxide nanoparticles.

Chapter 3

Experimental Results

This chapter presents the experimental results obtained using the surface science chamber coupled with the new HHG beamline. The experiments were performed under ultra-high vacuum (UHV) conditions with a base pressure of $\approx 1 \times 10^{-10}$ mbar. The study begins with measurements of the clean Mo(100) substrate and the epitaxially grown 10 monolayer magnesia thin film to establish a spectroscopic baseline. Following this, the primary focus of the investigation shifts to the characterization of manganese nanoclusters deposited onto this well defined support system.

To analyse the electronic properties of both manganese and manganese oxide nanoparticles, the study is divided into two distinct experiments. The first section details the systematic deposition of elemental manganese, while the second examines the subsequent interaction of these clusters with oxygen. Collectively, these experiments provide a comprehensive view of the hitherto unknown electronic structure evolution of manganese species on the magnesia surface.

3.1 Results of Molybdenum PES

To provide a reference for the system's electronic structure, this section presents the photoemission spectra obtained from the Mo(100) crystal following the cleaning procedures.

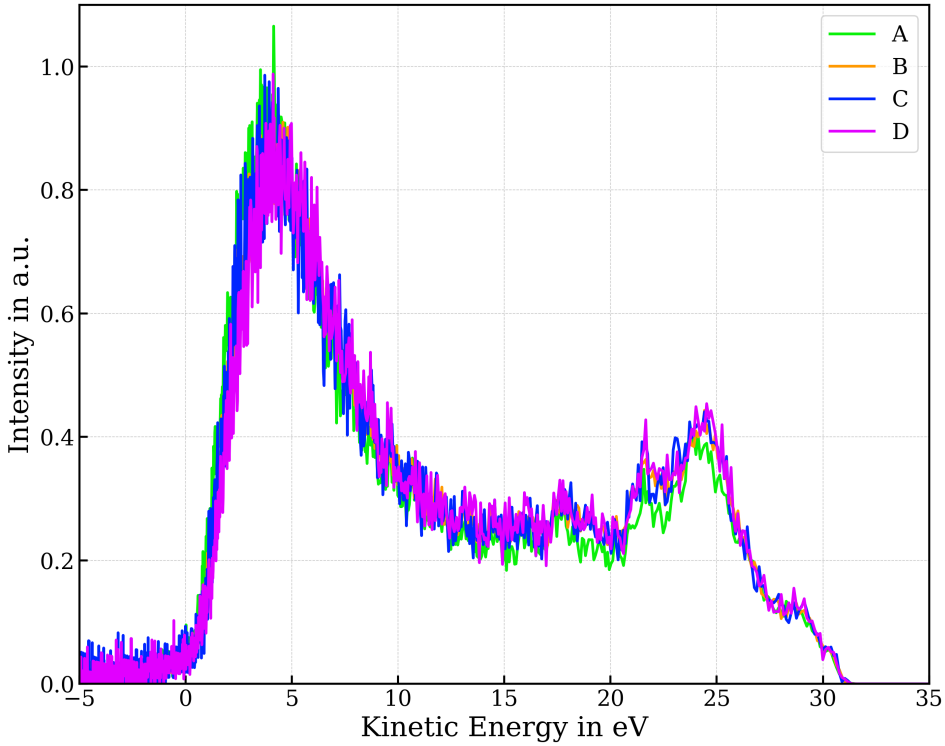


Figure 3.1: Spectra of cleaned molybdenum under varying conditions: (A) measurement at the optimal sample position, (B) measurement taken two hours later, (C, D) spectra recorded at reduced laser intensities.

3.1.1 Spectral Reproducibility

Clean Mo(100) photoemission spectra were recorded using the 23^{rd} harmonic of the 800 nm fundamental laser wavelength, corresponding to a photon energy of 35.6 eV. This harmonic has been chosen, as it sits in the minimum of the IMFP, as seen in Figure 1.5 previously. As illustrated in Figure 3.1, multiple measurements were acquired to verify that sample re-alignment and laser intensity do not introduce spectral variances. Spectrum A represents the measurement taken at the optimal sample position. To assess temporal stability, Spectrum B was acquired two hours after the initial measurement, showing virtually no deviation. Furthermore, Spectra C and D were recorded with reduced laser intensities. The consistent spectral features observed across these intensity variations rule out the presence of space charge effects, which would otherwise distort the kinetic energy distribution.

Figure 3.2 highlights the Fermi edge region of these recorded spectra. It is noteworthy that these datapoints are presented with no additional post-measurement energy correction or

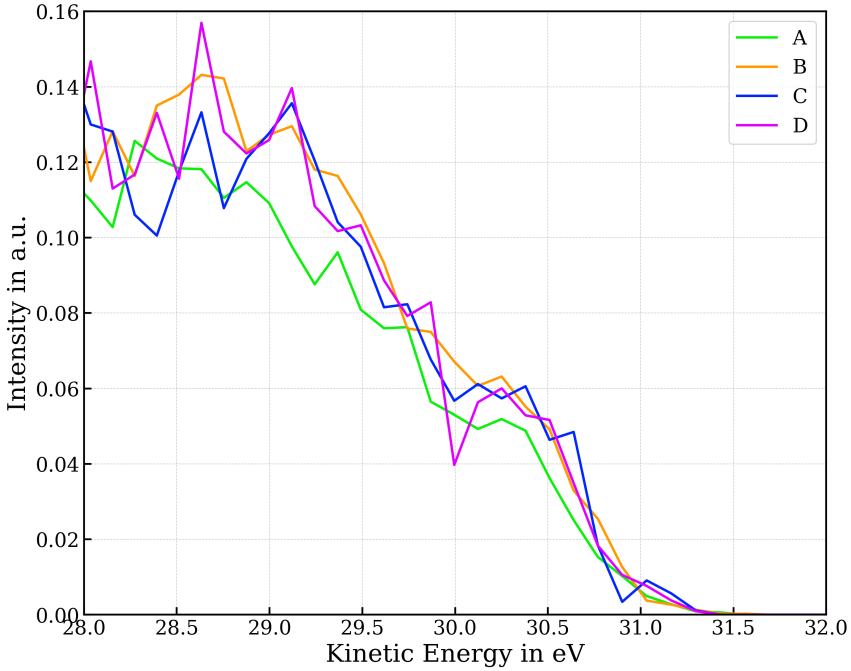


Figure 3.2: Zoomed Fermi edge region of Fig. 3.1

axis shifting. The flight times were converted to kinetic energy using the direct transfer function derived from the TOF calibration from Section 2.6.2, without further data manipulation or systematic correction. The precise alignment of the Fermi edges across the various measurement conditions show the setup's high alignment stability.

3.1.2 Data Processing

Figure 3.3 presents the full spectrum of the clean Mo(100) surface; raw dotted data points and the solid line which was smoothed with a Savitzky-Golay filter. The filter was employed to improve the signal-to-noise ratio by suppressing high-frequency noise without distorting the spectral line shapes or shifting peak positions (Savitzky and Golay, 1964). A window size of 21 points and a second-order polynomial were selected as a compromise between noise reduction and feature preservation, avoiding over-smoothing. The original data, plotted in the background as dots, confirms that the smoothing process introduces no significant distortion to the spectral features. Further spectra will be plotted with the Savitzky-Golay filter with these parameters going forward.

The Fermi level (E_F) is determined by locating the steepest edge in the spectrum via the

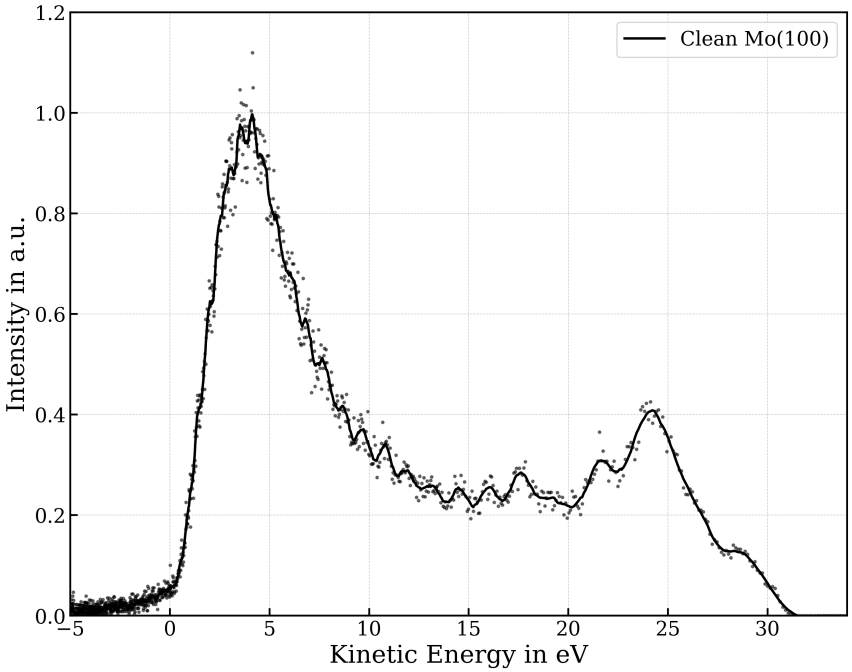


Figure 3.3: Clean Mo(100) spectrum with raw data shown as dots and the Savitzky–Golay filter as a solid line.

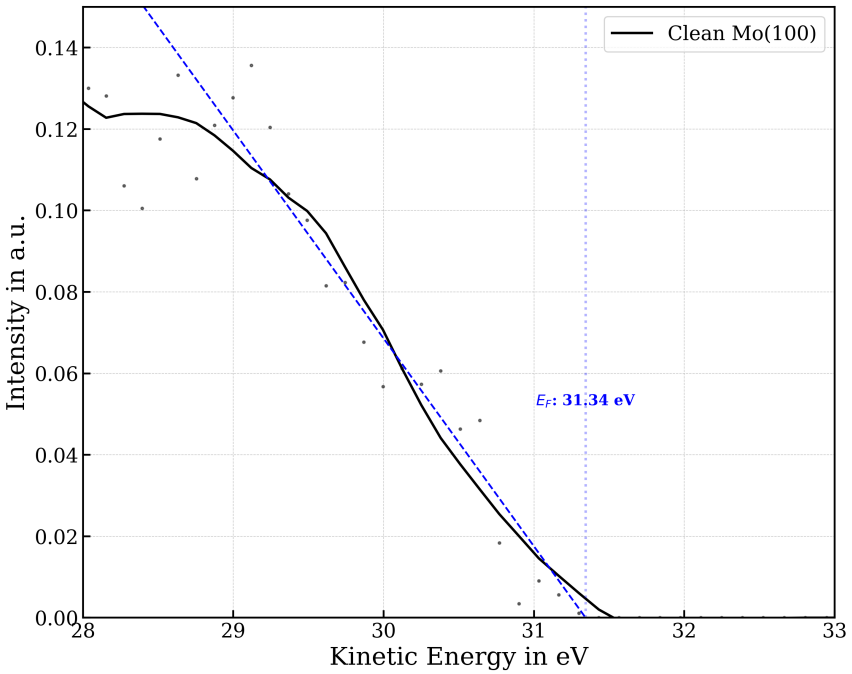


Figure 3.4: Fitted Fermi edge of a clean Mo(100) surface.

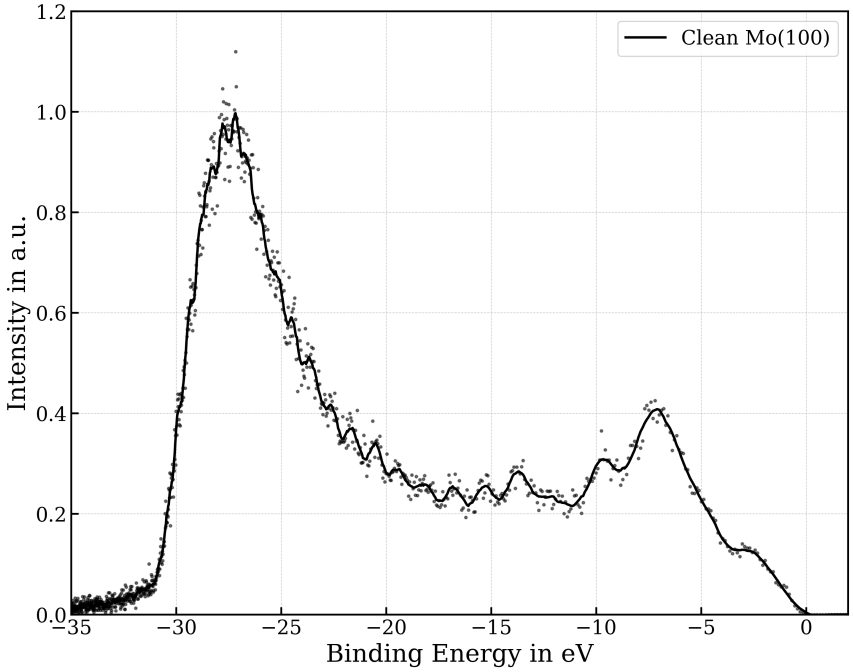


Figure 3.5: Clean Molybdenum spectrum with Savitzky–Golay filter applied in binding energy.

maximum of the first derivative with respect to kinetic energy. A linear regression was then applied to the data points within this edge region, and the x-intercept of the fitted line was taken as E_{F}. The result of this analysis for the clean Mo(100) surface are presented in Figure 3.4.

With this spectroscopic baseline established, the extracted Fermi edge serves as the zero-energy reference ($E_{\mathrm{B}} = 0$) for the system:

$$E_{\mathrm{B}} = E_{\mathrm{F}} - E_{\mathrm{kin}}. \tag{3.1}$$

By shifting the measured kinetic energy scale relative to this point, the entire spectrum is converted to binding energy. This transformation allows for a direct comparison of electronic features independent of the specific photon energy used during measurement. Figure 3.5 shows the resulting photoemission spectrum of the clean Mo(100) substrate on this calibrated binding energy scale.

3.2 Results of Magnesia PES

Following the characterization of the molybdenum substrate, a 10 ML MgO thin film was epitaxially grown on the surface. Because the MgO layer is sufficiently thin and in direct contact with the grounded metal substrate, the Fermi level of the oxide is pinned to that of the molybdenum. Consequently, the previously determined E_F continues to serve as the reference for the entire system, ensuring that all measured shifts in the intrinsic electronic states are isolated from experimental offsets.

The deposition of the oxide layer induces a fundamental transformation in the electronic structure, as evidenced by the PES measurements in Figure 3.6.

It can be seen, the spectra exhibit the characteristic of an insulating material. In contrast to the metallic substrate, the MgO film displays a complete suppression of the density of states at the Fermi level and the emergence of a wide bandgap, which corresponds to the portion of the MgO band gap that can be accessed via photoemission spectroscopy.

The film was characterized both after deposition and again following an annealing cycle at 1000°C for 10 minutes. The thermal treatment was undertaken to desorb any excess

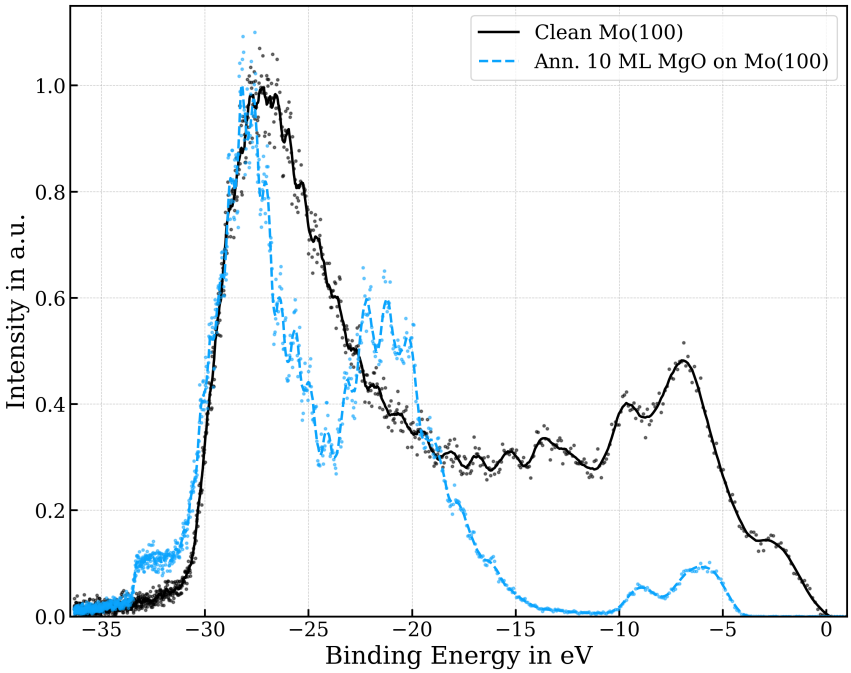


Figure 3.6: 10 ML of MgO deposited on Mo(100) vs. Clean Mo(100).

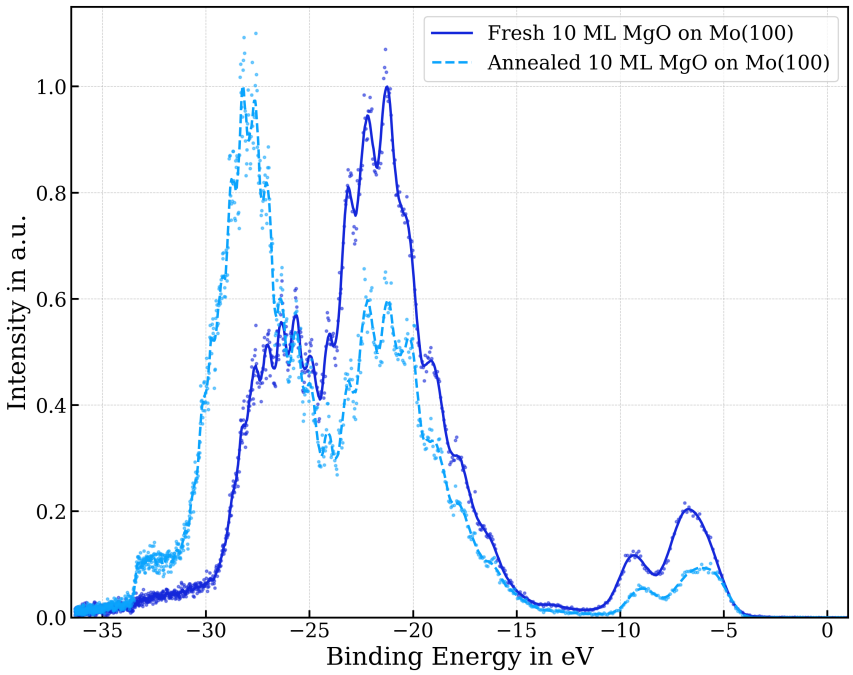


Figure 3.7: 10 ML of MgO deposited on Mo(100) prior to annealing and post anneal. Annealing was performed for 10 minutes at 1000°C.

oxygen, and to ensure a high crystalline quality. Figure 3.7 compares the spectrum of the as-deposited film with one recorded after the annealing.

3.3 Results of coverage dependent Manganese PES

Following the preparation of the clean Mo(100) surface and the subsequent growth and annealing of the 10 ML MgO film, the investigation proceeded with the systematic deposition of manganese.

A stepwise approach was employed to monitor the evolution of the electronic structure. Immediately following each manganese deposition step, a PES spectrum was recorded. To ensure high signal-to-noise ratios and comparability between datasets, the acquisition parameters were kept constant for every measurement. An event preset of 600,000 counts was set, corresponding to approximately one electron count per laser shot and a collection time of about 10 minutes per measurement.

Figures 3.8 and 3.9 show the results of Mn deposition and characterization across the coverages listed in Table 3.1.

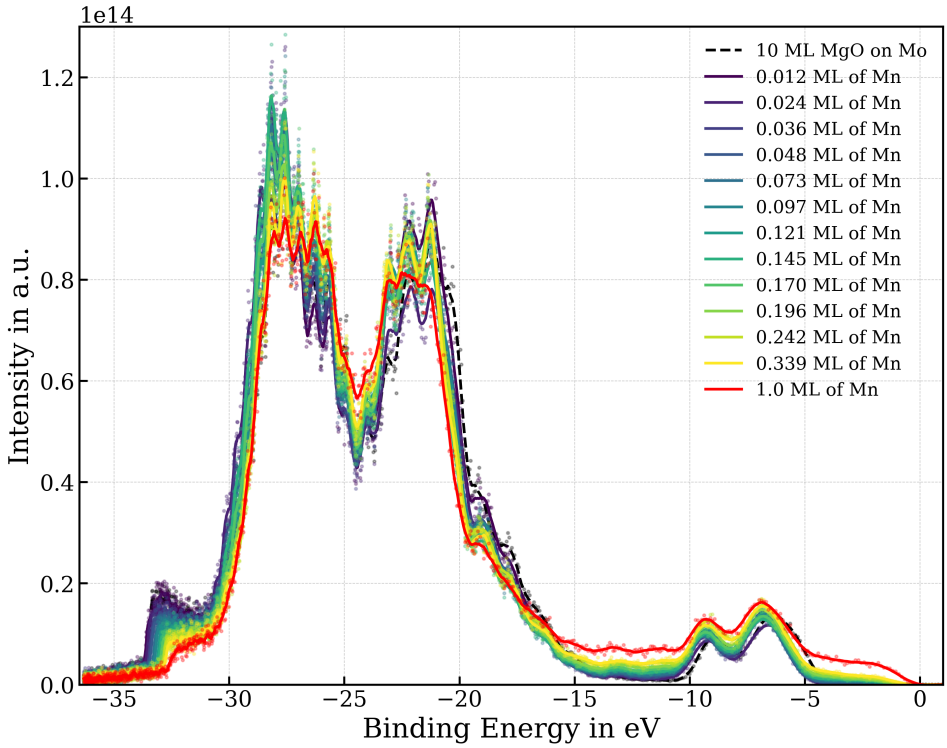


Figure 3.8: Mn Coverage dependent PES Spectra on 10 ML MgO on molybdenum.

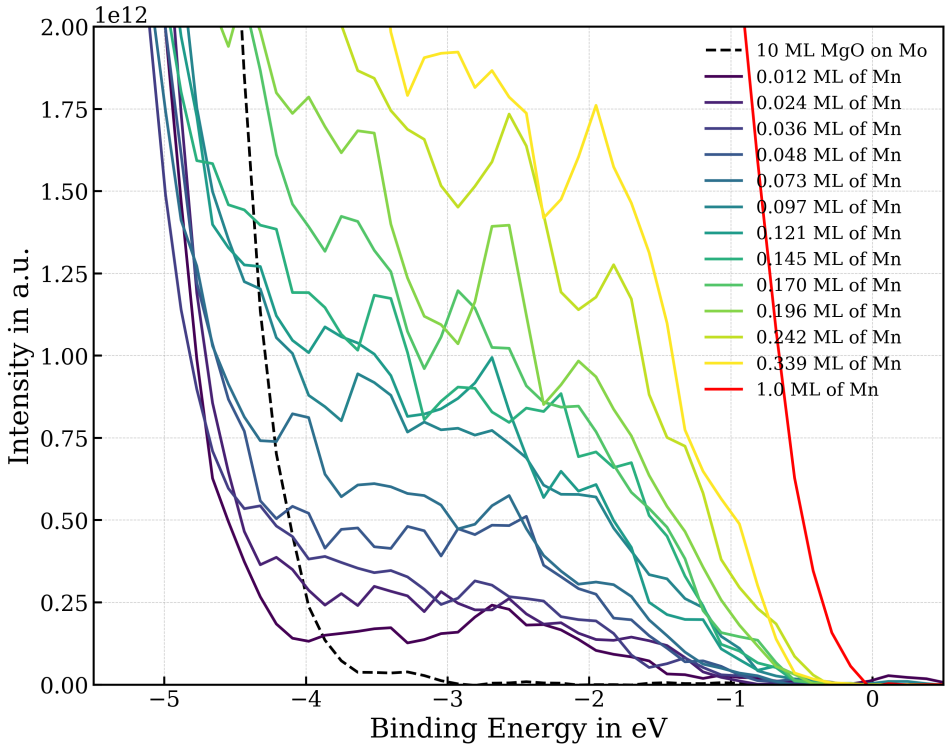


Figure 3.9: Zoomed Mn Coverage dependent PES Spectra on 10 ML MgO on molybdenum.

Table 3.1: Summary of manganese deposition steps.

Total Deposition Time in s	**Coverage in ML**
4	0.012
8	0.024
12	0.036
16	0.048
24	0.073
32	0.097
40	0.121
48	0.145
56	0.170
64	0.196
80	0.242
112	0.339
330	1.000

The zoomed measurements reveal the consecutive increase of the density of states at the Fermi edge, indicating that the bandgap formed after MgO deposition on molybdenum gradually closes as the manganese coverage increases. The Table 3.1 shows the specific deposition times and the corresponding calculated manganese coverages examined in this study. A detailed discussion will be provided in the following chapter.

Figure 3.10 shows the LEED pattern recorded at the end of this experiment.

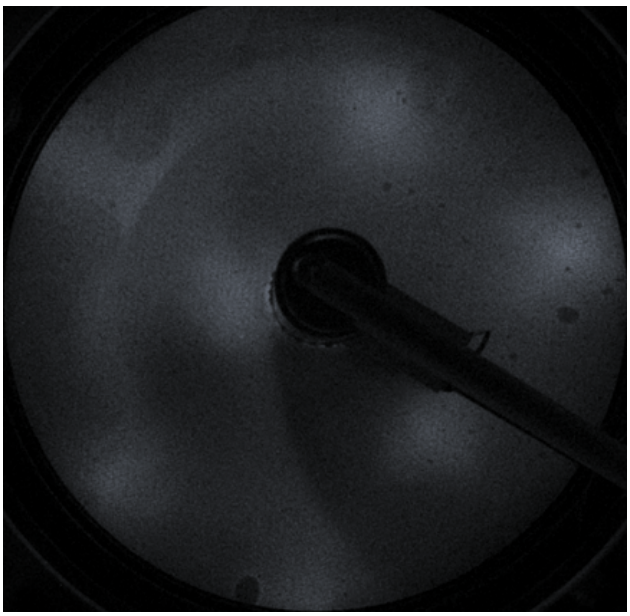


Figure 3.10: LEED after Deposition of 1ML Mn on 10 ML MgO.

The persistence of the MgO diffraction spots indicates that the Mn overlayer lacks long-range order, consistent with island growth or a disordered structure. The observed broadening of these spots is attributed to surface contamination that accumulated from the background vacuum during the $\approx$ 3 hour experiment.

3.4 Results of oxidized Manganese PES

Following the characterization of the metallic clusters, the second experimental series investigates the oxidation behavior of the non-epitaxial manganese nanoclusters. For this study, a fixed coverage of 1.0 ML manganese was prepared and then exposed to oxygen in controlled steps.

The oxygen partial pressure was strictly maintained at 2.0×10^{-8} mbar using a sapphire leak valve and monitored with an Aurun Microelectronics ion gauge set to an emission current of 5.0 mA. The gas correction factor of 1.0 was taken from the manufacturer's specifications for oxygen (Arun Microelectronics Ltd., 2022), allowing the gauge reading to be treated as the true pressure.

The leak valve was opened to a pre-calibrated distance, measured with a vernier caliper, to instantly establish the target pressure. A timer was utilized to track the exposure duration; upon completion of the countdown, the valve was closed, and a PES spectrum was acquired.

Table 3.2: Summary of oxygen exposures.

Time (s)	**Exposure (L)**
50	0.75
100	1.50
200	3.00
300	4.50
400	6.00
500	7.50
600	9.00
700	10.50
800	12.00
1000	15.00
1250	18.75
1500	22.50

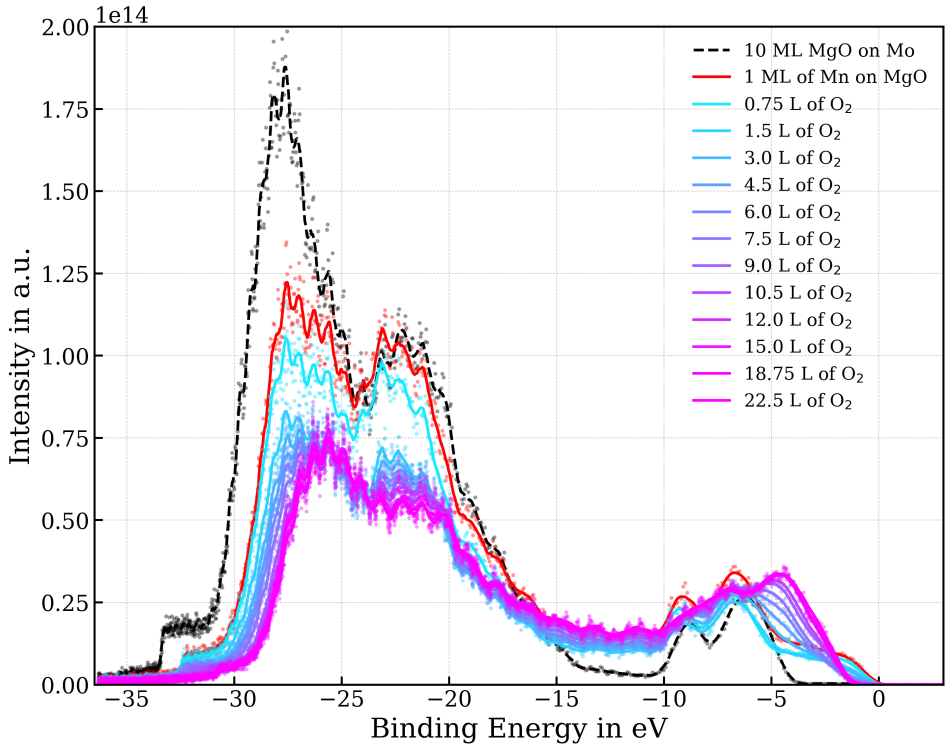


Figure 3.11: Photoelectron spectra of 1 ML Mn coverage on 10 ML MgO/Mo(100) after exposure to varying oxygen doses (in Langmuir).

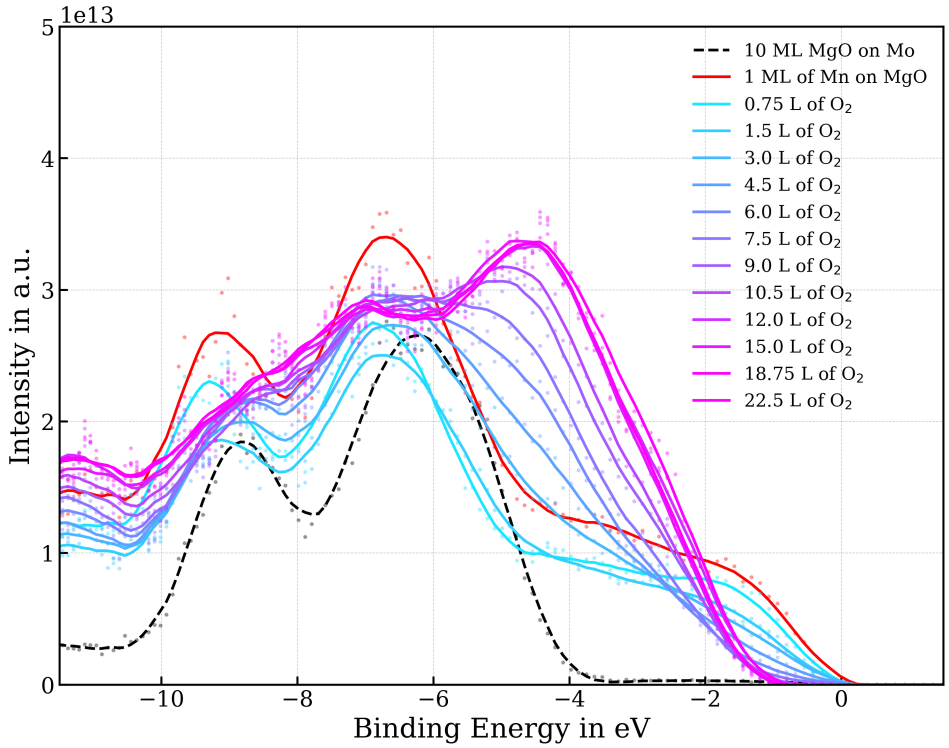


Figure 3.12: Detail of the Fermi edge in PES spectra for 1 ML Mn on 10 ML MgO/Mo(100) at varying oxygen doses.

Table 3.2 summarizes the specific exposure times and the calculated Langmuir (L) dosages applied to the surface. With the controlled exposure of oxygen to the surface, the evolution of the electronic structure was tracked relative to the oxygen dosage. The resulting PES spectra in Figure 3.11 illustrate the progressive oxidation of the manganese nanoparticles and the associated changes in their electronic states.

Figure 3.12 provides a magnified view of the Fermi edge region extracted from the full spectra in Figure 3.11. This detailed perspective allows for a clearer analysis of the density of states at the Fermi level and its suppression during the progressive oxidation steps. A detailed discussion will be provided in the following chapter.

Chapter 4

Discussion

Following the experimental findings, a critical interpretation is presented. The discussion begins with an evaluation of the clean Mo substrate, followed by the MgO thin film analysis. The coverage dependent evolution of the manganese electronic structure is reviewed, as well as the examination of the oxidation behaviour observed upon controlled oxygen exposure. Throughout this analysis, the experimental findings are contextualized with relevant literature citations.

4.1 Mo Substrate Characterization

The work function of the clean Mo(100) surface was determined from the spectral width between the Fermi-level cutoff and the secondary-electron cutoff (SECO). The secondary electron cutoff energy (E_{SECO}) was determined in the same manner as the Fermi edge, by fitting the steepest edge of the spectrum and taking the x-intercept of the linear regression, as shown in Figure 4.1. Due to the finite background intensity arising from secondary electrons and analyzer transmission, the linear extrapolation of the SECO does not intersect the baseline exactly at zero intensity (Schultz, 2022).

Using the spectral width between the two cutoffs, the work function is obtained as:

$$\Phi = h\nu - (E_{\mathrm{F}} - E_{\mathrm{SECO}})\,. \tag{4.1}$$

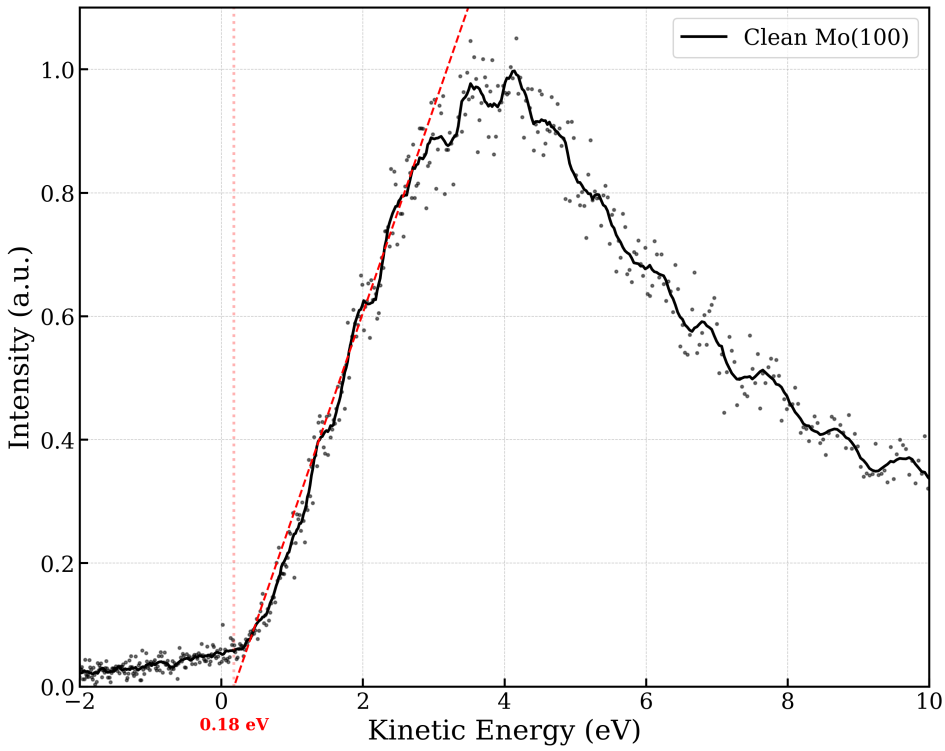


Figure 4.1: Fitted secondary electron cutoff of a clean Mo(100) surface.

Using $h\nu = 35.65$ eV, $E_F = -31.34$ eV and $E_{SECO} = 0.18$ eV, as taken from Figure 4.1 and Figure 3.4, yields $\Phi_{Mo} = 4.49$ eV. The uncertainty in the work function (Φ_{Mo}), determined from the detector time-bin width ($\Delta t = 250$ ps), is fully explained in Appendix C.

The complete measurement result for the molybdenum crystal for this measurement is thus given by $\Phi_{Mo} = 4.49 \pm 0.04$ eV, which is consistent with reported work functions for Mo(100) single crystals (Berge et al., 1974). It should be noted, that the work function Φ is highly sensitive to the exact state of the surface. Even with careful preparation, residual contaminants like trace oxygen or carbon can significantly shift the value. Minor surface defects and local variations in the surface potential also play a role. Additionally, limitations in how the spectrometer handles very slow electrons can influence the E_{SECO} measurement, leading to the small deviations observed (Helander et al., 2010).

The valence-band spectrum of clean Mo(100) measured at $h\nu = 35.65$ eV exhibits characteristic metallic behavior, with a clear Fermi cutoff at $E_F = 31.34$ eV. Consistent with the findings of Sundar et al. (2016) at similar photon energies, the spectrum in Figure 3.3 is defined by broad features rather than discrete peaks: a weak shoulder at $E_B \approx$ -4 to -5 eV

and a prominent maximum at $E_B \approx$ -7 to -8 eV.

While high resolution UPS can resolve discrete states near E_F, the feature at $E_B \approx$ -4 eV to -5 eV is intrinsically broad, comprising both bulk and surface-resonance contributions (Mikušik et al., 1981). The spectral line shape is highly sensitive to both photon energy and emission geometry. As noted by Werfel and Minni (1983), UV-excited spectra often deviate from the initial density of states due to matrix-element effects, cross-section variations, and depth sensitivity. Directional UV photoemission from Mo(100) shows that energy distribution curves change significantly with photon energy, even at normal emission (Cinti et al., 1976). Consequently, when comparing HHG-excited spectra to He I/II references, one should expect agreement in the general spectral envelope and peak positions rather than identical relative intensities.

The strong intensity at low kinetic energies (large E_B) in the molybdenum spectra shown in Figure 3.3, as well as in the following experimental spectra, is attributed to secondary-electron background and inelastic scattering. It is therefore not interpreted in terms of intrinsic valence-band states.

4.2 Magnesia Thin Film Characterization

Deposition of 10 ML MgO results in a characteristic insulator spectrum, as seen in Figure 3.6. The complete suppression of the intensity at the Fermi level confirms the formation of a band gap. As shown in Figure 4.2, the occupied MgO valence band, dominated by O $2p$ states, terminates -4.01 eV below E_F, in agreement with Jaouen et al. (2010).

The O $2p$ valence band features, resolved between -10 eV and -4 eV binding energy Figure 4.2, are assigned to the P_1 and P_2 transitions, which are described by Tjeng et al. (1990). According to them, this split reflects a superposition of angle-integrated and direct bulk transitions within the MgO band structure. The O $2s$ states appear as a peak centered near -21 eV binding energy, as shown in Figure 3.6, which corresponds to $\approx$ 18 eV below the Valence Band Maximum (VBM) consistent with Lu et al. (2006).

The energy level diagram in Figure 4.3 illustrates the electronic structure of an MgO film

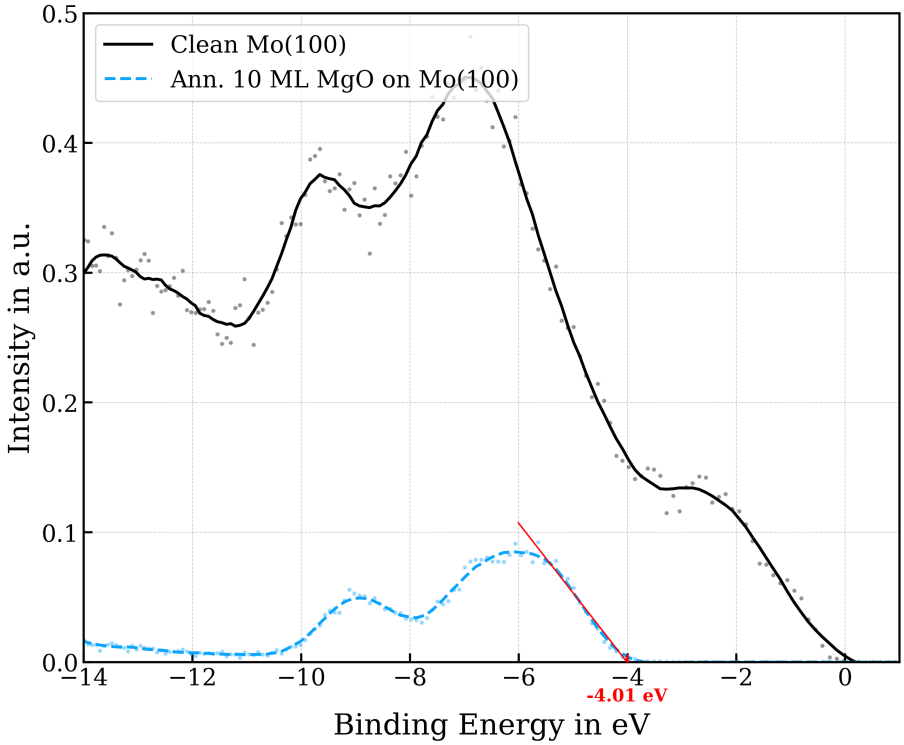


Figure 4.2: Zoomed spectra of Mo E_F and MgO VBM in binding energy scale.

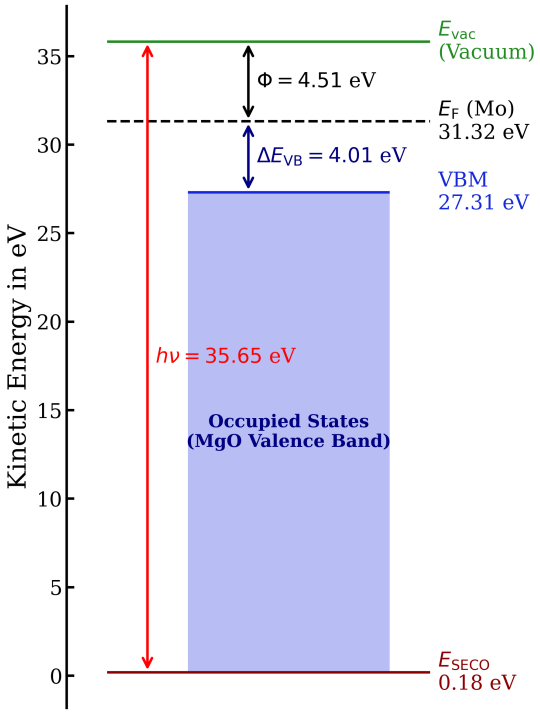


Figure 4.3: Energy level diagram of Mo E_F and MgO VBM.

on a Mo(100) substrate. Here, the work function (Φ_{Mo}) is determined to be 4.51 ± 0.04 eV.

4.2.1 Resolving the MgO Bandgap

The distinct observation of a wide bandgap in the photoemission spectra following the deposition of 10 ML of MgO on the clean Mo substrate validates the efficacy of utilizing the higher harmonic generated light for this system. This advantage is a direct consequence of the strong surface sensitivity granted by the XUV probe. Consequently, the photoemission signal is dominated by the topmost atomic layers. The 35.6 eV XUV light is perfectly tuned to isolate the electronic structure of the MgO overlayer without the spectra being overwhelmed by the bulk Mo substrate, allowing for the direct and unambiguous observation of the MgO bandgap.

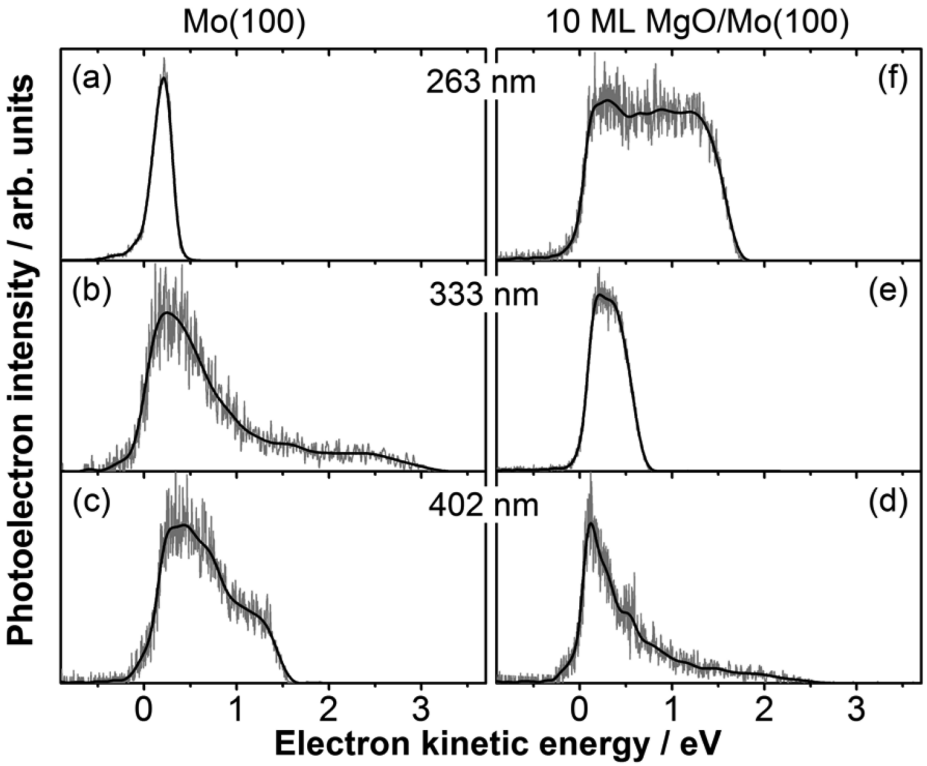


Figure 4.4: Fs-laser photoemission spectra obtained at excitation wavelengths of 263, 333, and 402 nm from a bare Mo(100) surface (a–c) and from a Mo(100) surface covered by a 10 ML MgO(100) ultrathin film (d–f). Thin gray lines represent the experimental data; bold black lines were obtained by applying a low pass FFT filter to the data. The laser pulse energies employed to obtain the spectra were (a) 0.4, (b) 52, (c) 62, (d) 7, (e) 0.1, and (f) 0.1 nJ. Reprinted with permission from (Vaida et al., 2009) E. Vaida, T. Gleitsmann, R. Tchitnga, and T. M. Bernhardt, J. Phys. Chem. C 2009, 113, 10264. Copyright 2009 American Chemical Society.

In contrast, earlier investigations by our group (Vaida et al., 2009) lacked the necessary surface sensitivity to probe the intrinsic electronic structure of the oxide layer. Standard photoemission spectroscopy in the ultraviolet to visible laser light range generates photoelectrons with very low kinetic energies. At these low kinetic energies, the electron mean free path drastically increases, meaning the probing depth extends significantly deeper into the bulk Mo. Therefore, the spectral features captured in those earlier experiments were fundamentally limited by the bulk-dominant nature of the emitted electrons, effectively masking the valence band signatures of the ultra-thin MgO film.

This difference in probing depth provides valuable context for interpreting the previous group's findings. When examining the spectra presented in Figure 4.4 of their publication (Vaida et al., 2009), their results suggest that the low-energy laser setup was primarily sensitive to the macroscopic electrostatic changes at the sample surface. Specifically, the reported shifts align perfectly with a work function reduction of the supporting Mo(100) substrate. As extensively detailed in the theoretical frameworks established by Prada et al. (2008), the deposition of ultra-thin, polarizable oxide films like MgO onto transition metal substrates induces a strong interfacial dipole moment due to charge compression and redistribution at the metal-oxide interface. This interface dipole acts to lower the overall work function of the system.

Therefore, the shifts observed in Figure 4.4 of their prior study likely reflect the lowering of the photoemission threshold caused by this interface dipole. Because the photon energies used in that study were situated within the bulk-dominated inelastic mean free path regime, the methodology was highly effective for observing this work function reduction, but less optimal for probing the internal electronic states of the oxide itself. By transitioning to the XUV light, the current experimental setup achieves the rigorous surface sensitivity required to build upon those earlier electrostatic measurements. This allows us to directly capture the true valence band structure and bandgap of the MgO adlayer, providing a more complete picture of the system's electronic properties.

4.2.2 Momentum-Dependent Oscillations in MgO PES

Figure 4.5 displays a section of Figure 3.7 in the -15 to -32 eV binding energy range. Upon closer inspection of the data, a series of satellite peaks appear superimposed on top of the broad background with their frequency noticeably increasing towards higher binding energies.

Initially, it seemed plausible that these ripples were plasmon replicas. Literature from Hengehold and Pedrotti (1976) and Mendis (2021) establishes that collective excitations, like the MgO bulk plasmon at 22 eV, can create satellite copies of the primary valence band. However, a pure plasmon loss model cannot fully explain the behavior seen here. Plasmon replicas are rigid energy shifts, meaning they should create an exact, linearly spaced copy of the original valence band structure. Furthermore, the 22 eV bulk plasmon is simply too far away to account for the sheer number of peaks and the complex spacing observed in this intermediate region, ranging from -16 to -30 eV binding energy.

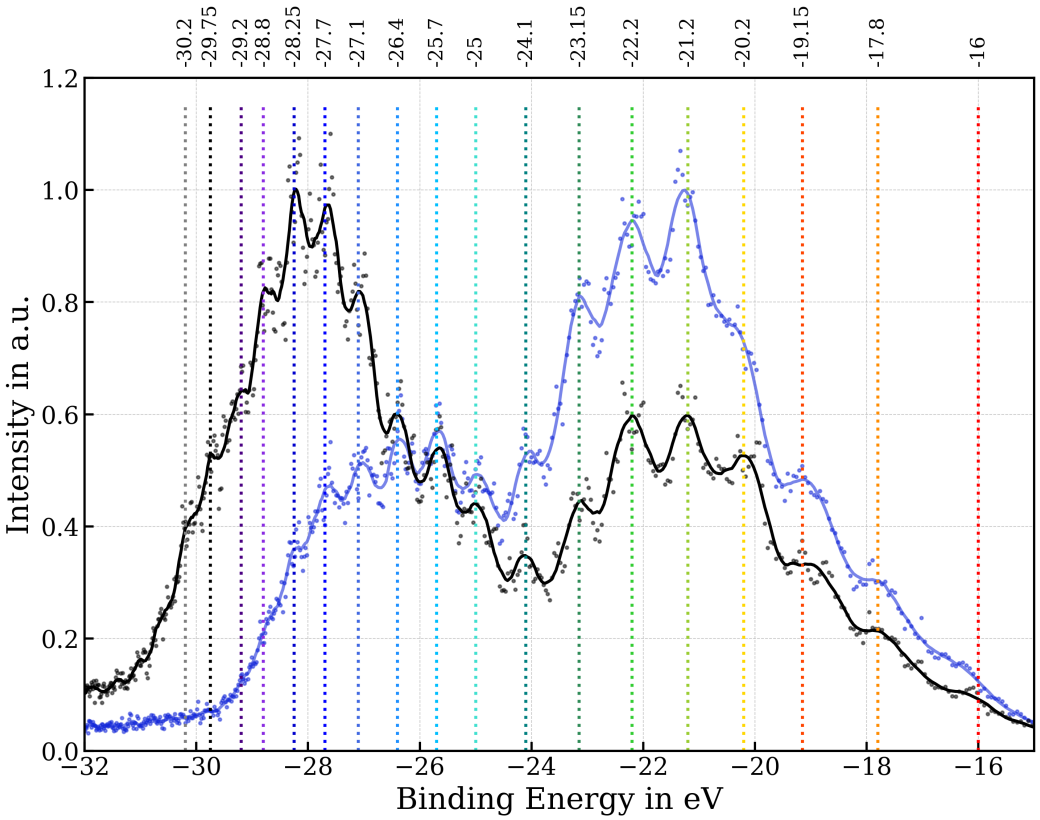


Figure 4.5: As-deposited (blue) and annealed (black) spectra for 10 ML MgO/Mo(100). Dashed lines highlight satellite peaks caused by suspected photoelectron interference.

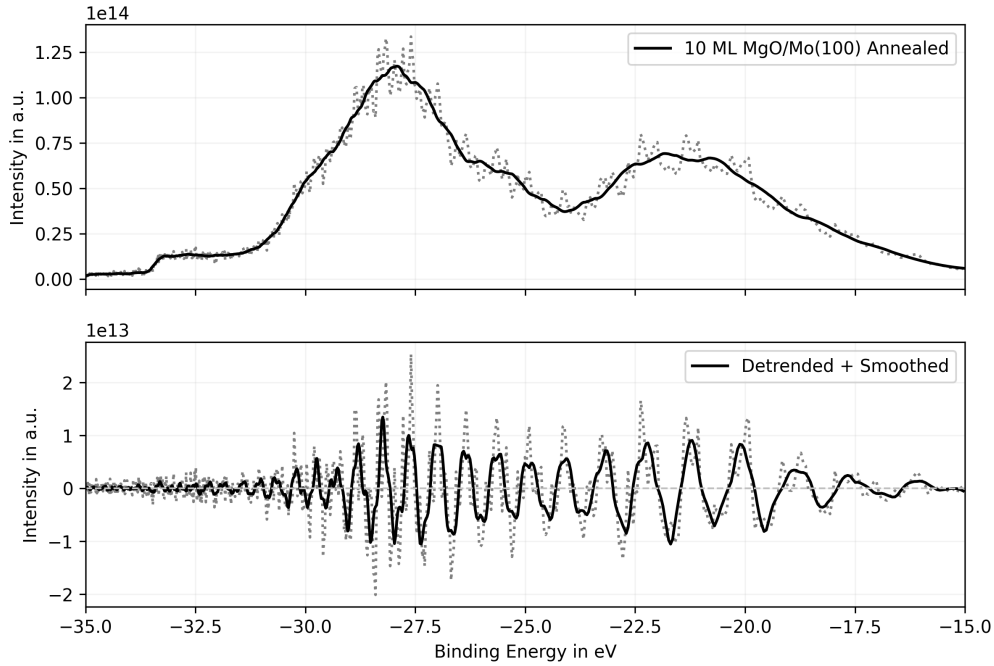


Figure 4.6: PES of 10 ML MgO (top) and baseline-subtracted spectrum (bottom), revealing oscillatory features. A Savitzky–Golay filter was applied to the oscillations for clarity.

The determining factor in ruling out an instrumental or electronic origin for these features was the energy-dependent peak spacing evident in Figure 4.6; the oscillations become visibly closer together as the spectrum moves towards lower kinetic energies. Electronic artifacts such as circuit ringing or detector resonances would produce peaks with constant spacing in energy, independent of the electron kinetic energy. The observed spacing instead grows systematically with kinetic energy, which is the hallmark of momentum-based interference. Similar spectroscopic fine structures, arising from the quantum confinement and boundary reflection of electron waves, have been documented in other ultra-thin epitaxial systems by Müller et al. (2016). As the photoelectrons escape the sample, their quantum mechanical waves scatter and reflect between two boundaries, creating a thin-film interference pattern characteristic of a Fabry-Pérot resonator.

As demonstrated by Paggel et al. (1999) for analogous epitaxial systems, these discrete quantum-well states are governed by Bohr-Sommerfeld quantization (Cohen-Tannoudji et al., 2020), dictating that the interference fringes must be evenly spaced in momentum (k) space rather than energy space. Consequently, the intervals between the observed peaks must be proportional to the square root of the kinetic energy ($\sqrt{E_{\text{kin}}}$). When plot-

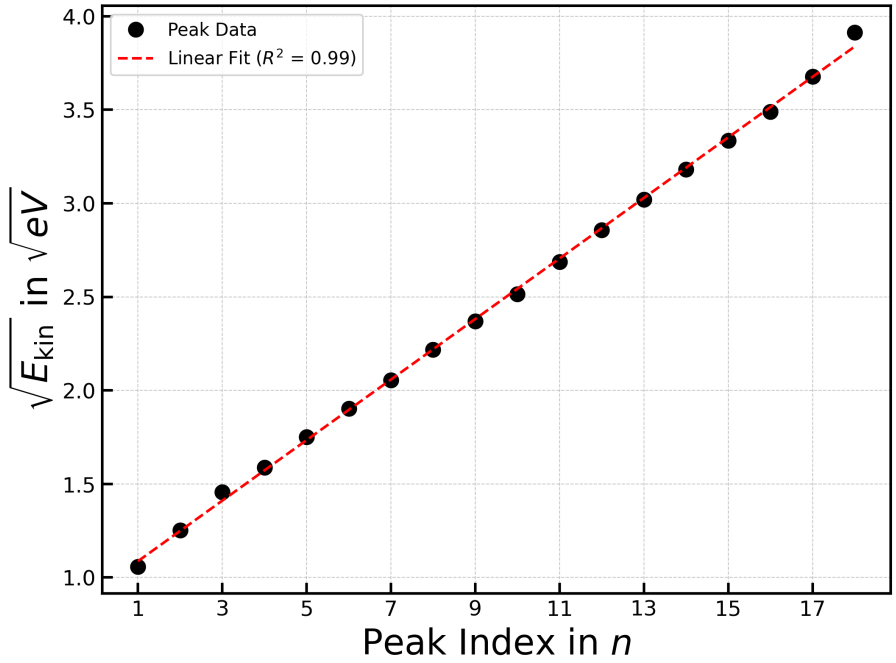


Figure 4.7: Linear fit (red dashed line) of the square roots of the identified peak energies, $\sqrt{E_{\text{kin}}}$ from Figure 4.5 versus the observed peak index n.

ting the peak index against $\sqrt{E_{\text{kin}}}$, the data shown in Figure 4.7, yields a highly linear fit ($R^2 = 0.99$), confirming that the periodicity is momentum-dependent and inconsistent with an electronic artifact. Helmreich et al. (2021) reported quantum-well resonances in epitaxial MgO films, which at first appeared to offer a plausible explanation for the observed peaks.

However, upon closer examination, an similar oscillatory pattern with the same extracted periodicity was found in spectra recorded from clean Mo(100) and from Mn/MgO/Mo(100) samples measured under identical experimental conditions. Although the peak positions were shifted by a few eV in both cases, the equidistant peaks in momentum space remained consistent across all measurements. The most plausible interpretation is that the periodicity reflects a property of the Mo(100) substrate itself, either arising from standing waves formed between the surface barrier and a reflective feature within the Mo(100) final-state band structure that persists regardless of the thin overlayer.

In all three measurements the Mo substrate lies within or just beyond the photoelectron sampling depth. At a photon energy of 35.6 eV, the electrons at which the oscillations

predominantly occur have kinetic energies below 15 eV, corresponding to inelastic mean free paths exceeding 10 Å. Keeping in mind the thickness of the 10 ML MgO film of approximately 21 Å, a contribution from the Mo substrate to the observed oscillation therefore cannot be excluded.

Two experiments would help resolve the origin of this periodicity. First, repeating the measurement at a different harmonic of the HHG source would change the photon energy and therefore shift the absolute kinetic energies of all features. Genuine quantum-well states tied to the film or substrate band structure would shift their positions in binding energy as the photon energy changes, while an instrumental artifact would not. Second, measuring a significantly thicker MgO film, well beyond 10 ML, would increase the electron path length within the oxide and attenuate the contribution of the Mo substrate to the final state. If the periodicity changes or disappears with increasing MgO thickness, the Mo substrate is the source. If it persists unchanged, an instrumental origin cannot be excluded. At present the interpretation of these experimental results remains ambiguous and is therefore left for future investigation, as it does not contribute to the primary aim of this scientific endeavor.

4.2.3 Annealing of MgO Thin Film

Figure 3.7 illustrates the spectral evolution between the as-deposited and annealed MgO films. Following Pal et al. (2014), these differences indicate a transition from an oxygen-rich initial state to a stoichiometric surface. The elevated work function of the fresh 10 ML film stems from excess oxygen incorporated during growth, creating a strong surface-polarizing dipole, which manifests in the spectrum as a reduced spectral width. Annealing at 1000°C desorbs this excess species and promotes crystalline ordering, thereby lowering the work function and shifting the secondary electron cutoff.

The signal observed below 0 eV indicates a patched surface where MgO islands have formed due to lattice mismatch. This leads to the coexistence of distinct work functions, a phenomenon detailed by Baddorf (2023), who explains how such surface inhomogeneities result in multiple contributions to the measured secondary electron cutoff.

This well-characterized MgO/Mo(100) system provides an ideal support for the subsequent

deposition of manganese nanoclusters. The insulating nature of the oxide layer ensures electronic decoupling of the deposited metal clusters from the underlying metallic substrate.

4.3 Electronic Structure of Mn and MnO Nanoparticles

4.3.1 Coverage Dependent Spectral Evolution

The systematic evolution of the photoemission spectra with increasing manganese coverage, as shown in Figure 3.8 and Figure 3.9, indicates a continuous modification of the surface electronic structure. At the lowest nominal coverages of 0.012 to 0.036 ML, the spectra remain dominated by MgO-derived valence features, with only weak Mn-related intensity, consistent with the small number of Mn emitters in the sub-monolayer regime. In a closely related Mn/MgO/Ag(001) system, DFT+U predicts pronounced site dependence: Mn adsorbed on the O-top site retains a near-atomic spin moment of approximately 2.4 μ_B, whereas adsorption at hollow or Mg-top sites reduces the moment and increases the crystal-field splitting of the Mn d levels. Importantly, the atom-projected DOS for the O-top configuration shows negligible Mn-d and O-p spectral weight in the immediate vicinity of E_{F}. Gangopadhyay et al. (2020) provide this natural explanation for why the lowest-coverage spectra remain essentially insulating, as confirmed by our spectra in Figure 3.9.

At intermediate coverages of 0.073 to 0.242 ML, spectral weight in the previously depleted energy window between the MgO valence-band maximum and the Fermi level becomes increasingly pronounced. This behaviour signals the growing contribution of Mn-derived states within the MgO band gap, attributable to the developing Mn 3d manifold and metal-induced gap states (MIGS).

Above approximately 0.1 ML, shoulders appear at $E_{\mathrm{B}} \approx -3.4$ eV and $E_{\mathrm{B}} \approx -4.4$ eV (ref. Figure 3.9), consistent with occupied Mn-derived states entering the MgO gap (Gangopadhyay et al., 2020). At higher coverages of 0.242 to 0.339 ML, an additional local maximum becomes apparent near $E_{\mathrm{B}} \approx -1.7$ eV as the intensity extends closer to E_{F}.

The 1.0 ML spectrum shows the most pronounced change, with substantial intensity persisting up to the Fermi cutoff, consistent with the onset of band formation and electronic delocalization as Mn aggregates grow and the overlayer becomes increasingly connected. Minor changes in apparent peak position and line shape with coverage are expected in this regime, since the measured spectrum represents an ensemble average over a distribution of cluster sizes and local adsorption environments on an insulating support.

The development of near-E_F intensity with coverage is consistent with a size-driven transition from localized electronic states in isolated adatoms or small clusters toward more delocalized states in larger aggregates. Size-dependent effects in Mn clusters are well established: Stern–Gerlach experiments on gas phase Mn_n clusters report net magnetic moments far below the atomic value, typically in the range of approximately 0.4 to 1.7 μ_B per atom for n spanning a few to tens of atoms, indicating strong size-dependent quenching and nontrivial spin coupling Knickelbein (2001, 2004). Complementary first-principles calculations for Mn_n with $n = 2$ to 20 predict a transition from ferromagnetic ordering in the smallest clusters to ferrimagnetic ground states from $n \approx 5$ onward, together with coordination-driven broadening and reduced localization of the Mn d states (Kabir et al., 2006).

Within this framework, the coverage at which a clear Fermi-edge intensity emerges provides an experimental proxy for the critical cluster size and electronic connectivity required for metallization on MgO-supported Mn, as can be seen in Figure 3.9. Such size-dependent electronic transitions are well-documented for noble metals on oxide supports (Vaida et al., 2022). The present observations extend this understanding to the case of manganese on magnesia.

Complementary evidence for the tunability of the Mn electronic structure comes from conductance spectroscopy measurements on MnO and Mn_3O_4 islands grown on Au(111), where the band gap and the energy position of localized Mn 3d in-gap states were found to vary systematically with oxide phase and surface termination (Möller et al., 2019), consistent with the picture emerging from the present coverage series.

The absence of epitaxial ordering, as determined from LEED analysis, is significant in

interpreting these spectroscopic observations. Unlike systems where epitaxial growth produces well-defined layer-by-layer structures, the disordered or three-dimensional growth mode of manganese on MgO leads to a distribution of cluster sizes at any given coverage. Consequently, the spectroscopic signatures represent an ensemble average over this size distribution, and the observed transition to metallic behavior reflects the point at which a sufficient fraction of the deposited material resides in clusters large enough to exhibit bulk-like electronic properties.

4.3.2 Progressive Oxidation of Manganese Nanoparticles

The controlled exposure of the nominal 1.0 ML Mn overlayer to oxygen, as presented in Table 3.2 and Figure 3.11, provides a systematic probe of the initial oxidation process.

The photoemission spectra exhibit a clear transformation in the electronic structure of the Mn deposits with increasing oxygen exposure. At low exposures (0.75 to 3.00 L), the dominant change is a rapid reduction of low-binding-energy (near-E_{F}) spectral weight relative to the pristine Mn-on-MgO spectrum. A similarly rapid suppression of the metallic Mn valence response upon initial oxygen exposure has been reported for Mn surfaces, where oxidation proceeds directly towards an MnO-like valence structure at room temperature (Lescop, 2006). This behaviour indicates early-stage passivation of Mn-derived metallic states, consistent with the onset of oxygen chemisorption and Mn–O bond formation.

At intermediate exposures (4.50 to 12.00 L), the valence-band lineshape evolves from a Mn-on-MgO response, which contains low-binding-energy spectral weight, towards an oxide-like electronic structure characterised by pronounced band features and a suppression of intensity near E_{F}. Such suppression aligns with the classification of MnO as a correlated insulating monoxide; indeed, combined valence- and conduction-band spectroscopies have established an experimental gap of $\sim$ 3.9 eV (van Elp et al., 1991). Across the same exposure range, progressive Mn–O bond formation suggests the growth of an MnO-like overlayer within the photoemission probing depth. This interpretation is further supported by prior UPS/MIES studies, which observed MnO formation upon O_2 exposure without detecting intermediate Mn_xO_y states in the valence-band response (Lescop, 2006).

The persistence of MgO-like spectral weight over this range indicates that the measured signal remains a superposition of contributions from MgO, Mn-rich regions, and MnO-rich regions. Accordingly, the intermediate-dose changes are most naturally attributed to an increasing MnO fraction and effective oxide thickness, together with attenuation of the magnesia contribution, rather than to a sequence of distinct intermediate Mn_xO_y phases resolvable from valence-band spectra alone. In this sense, the residual MgO-derived valence-band intensity provides a practical continuity indicator, implying incomplete lateral closure of the Mn-derived overlayer and/or a probing depth that still samples the buried MgO interface.

At the highest exposures, the magnesia O 2p-derived valence-band features are strongly attenuated while a dominant oxide feature emerges near $E_B \approx -4.7$ to -4.2 eV. Simultaneously, the metallic near-E_F spectral weight is negligible, and the spectra converge to a stable MnO-like lineshape. This behaviour is consistent with an MnO-dominated near-surface electronic structure and an increased effective oxide thickness within the photoelectron escape depth, such that the buried MgO contribution becomes negligible. The emergence and saturation of the MnO-like valence response therefore provides a practical spectroscopic marker for tracking Mn oxidation in subsequent catalytic experiments (Fujimori et al., 1990).

4.4 Tuneability of the Electronic Structure of Mn and MnO for OER

It was shown by van Oversteeg et al. (2017) that the metal-centered character of the transition metal oxide radical, and therefore the preferred reaction pathway in water oxidation, depends directly on the oxidation state and electronic structure of the Mn site. This places the spectroscopic characterization presented here in a broader context: the coverage-dependent evolution of the Mn valence structure and the progressive oxidation series are not merely descriptive observations but represent a systematic demonstration that the electronic structure of these surfaces is tuneable.

The catalytic implications of this tunability are well illustrated by the work of Indra et al. (2013), who showed that nanostructured MnO particles are essentially inert toward water oxidation but become active upon partial oxidation to a mixed-valent MnO_x phase. Critically, this activation could not be attributed to changes in surface area or morphology alone, pointing instead to the oxidation state as the decisive variable.

Given that the OER constitutes the kinetically limiting step in water splitting, the ability to drive and monitor precisely this kind of oxidation state transition through the experimental approach developed in this thesis suggests a viable route toward the rational optimization of MnO_x-based catalyst surfaces. This work provides the spectroscopic foundation for developing relationships between structure and activity.

Chapter 5

Conclusions

The experimental investigation presented in this work has successfully addressed the central scientific questions regarding the electronic structure of manganese nanoclusters deposited on magnesia thin films and their evolution upon oxidation. The systematic approach, beginning with thorough substrate characterization and proceeding through coverage-dependent and oxidation-dependent measurements, provides a comprehensive picture of this model system.

The primary experimental objectives have been achieved. The photoemission spectroscopy measurements, facilitated by the custom built HHG beamline, have provided new and unprecedented detailed information about the electronic structure evolution of manganese and manganese oxide nanoparticles throughout the deposition and oxidation processes.

A significant finding of this investigation concerns the growth behavior of manganese on the magnesia surface. LEED analysis has demonstrated that manganese does not grow epitaxial on MgO. This observation indicates that the interaction between manganese atoms and the MgO surface does not favor the adoption of the substrate lattice spacing, leading instead to disordered or three-dimensional island growth. This growth mode has important implications for both the electronic properties of the deposited clusters and their reactivity, as the resulting morphology will feature a distribution of cluster sizes and a high density of undercoordinated surface sites.

The coverage-dependent measurements have revealed a clear transition from localized, non-metallic electronic states at low manganese coverages to metallic behavior as the coverage approaches 1.0 ML. This transition, evidenced by the progressive development of spectral weight at the Fermi level, reflects the fundamental size-dependence of electronic structure in nanoscale metal clusters. The critical coverage for this transition provides an estimate of the cluster size at which bulk-like metallic properties emerge in the Mn/MgO system.

The systematic oxygen exposure of the 1.0 ML Mn nanoclusters has shown a clear and controllable transition from metallic to MnO-like electronic structure, evidenced by the progressive suppression of Fermi-level spectral weight and the opening of a bandgap. This provides a reliable spectroscopic handle for monitoring the manganese oxidation state in future reactivity experiments.

5.1 Future Investigations

The characterization work presented here establishes the essential foundation for subsequent investigations of chemical reactivity on this well-defined model system. The ability to prepare manganese nanoclusters with controlled coverage and oxidation state, combined with the spectroscopic methods to monitor their electronic structure, provides the necessary prerequisites for performing and documenting chemical reactions at these surfaces.

The correlation of reactivity with cluster size and oxidation state, made possible by the systematic characterization approach demonstrated in this work, promises to yield fundamental insights into the structure-activity relationships that govern heterogeneous catalysis on oxide-supported metal nanoparticles.

Future experiments can exploit this established framework to investigate catalytic reactions relevant to industrial and environmental applications. Expanding the current PES setup with the integration of a mass spectrometer would enable the detection and identification of reaction products, as previously explored by the working group using visible light. By utilizing the XUV light from this beamline, a more complete understanding of the reaction mechanism could be obtained.

The origin of the oscillatory peaks detected in the MgO spectra also warrants further investigation. Determining whether the observed periodicity is intrinsic to the Mo(100) substrate, transferable to other coating materials, or dependent on film thickness would clarify the physics of the interference. Measurements at different HHG harmonics would be a natural first step, since genuine quantum-well states shift with photon energy while instrumental artifacts do not. Beyond this, the HHG-based setup is inherently suited for time-resolved pump-probe experiments, where an optical pump pulse excites the system and the HHG pulse probes the transient electronic structure. This would open the possibility of directly tracking electron dynamics in excited states of the MgO film or the Mn clusters on femtosecond timescales.

In conclusion, this investigation has provided a comprehensive characterization of the Mn/MgO/Mo(100) model system using photoemission spectroscopy with High Harmonic Generation excitation. The results establish the electronic structure baseline, reveal the coverage-dependent transition to metallic behavior, and document the spectroscopic signatures of manganese oxidation. These findings position this model system as a well-characterized platform for future studies of surface chemical reactions, with particular potential for investigations that exploit mass spectrometric detection of reaction products.

Appendix A

Determining the Blaze Angle for the Grating

Blaze-angle-dependent reflection efficiencies were simulated using the Looper tool from REFLEC from F. Schäfers (Schäfers, 1996). The calculations were performed to quantify how the grating blaze condition impacts the usable photon flux under the experimental geometry and polarization, and to guide the selection of grating parameters for the target photon-energy range.

Figure A.1 presents the simulated reflection efficiency for p-polarized light using a 350 lines/mm grating as a function of blaze angle. The results for a 700 lines/mm grating are shown in Figure A.2. Since the goal was to achieve two grating line densities on a single substrate, a common blaze angle for both gratings was the simplest and most robust manufacturing choice.

Figure A.3 compares multiple groove densities at a fixed blaze angle of 3.5°.

Following discussions with the grating manufacturer, a blaze angle of 3.6° was targeted as it represented a value for which they could guarantee reliable performance and production tolerances for both line densities.

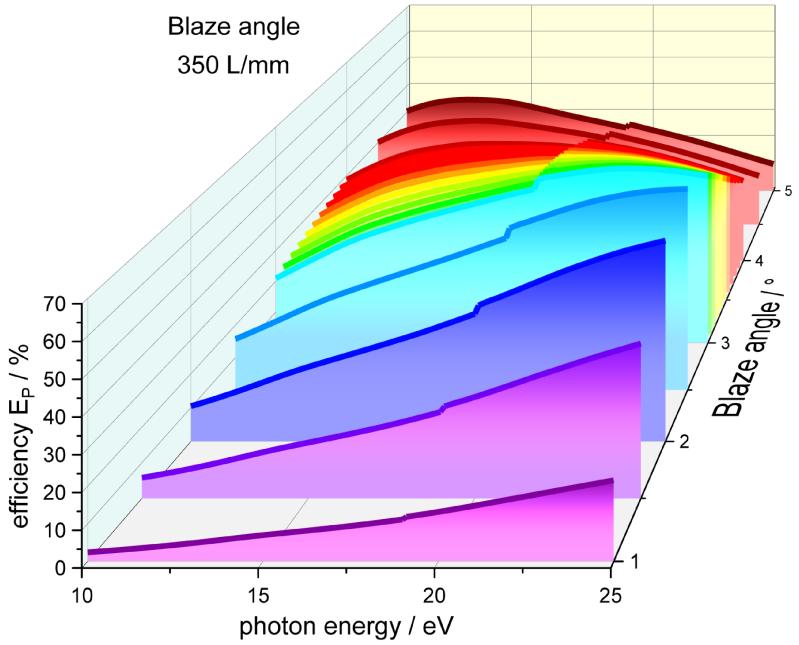


Figure A.1: Blaze Angle variation for 350 lines/mm.

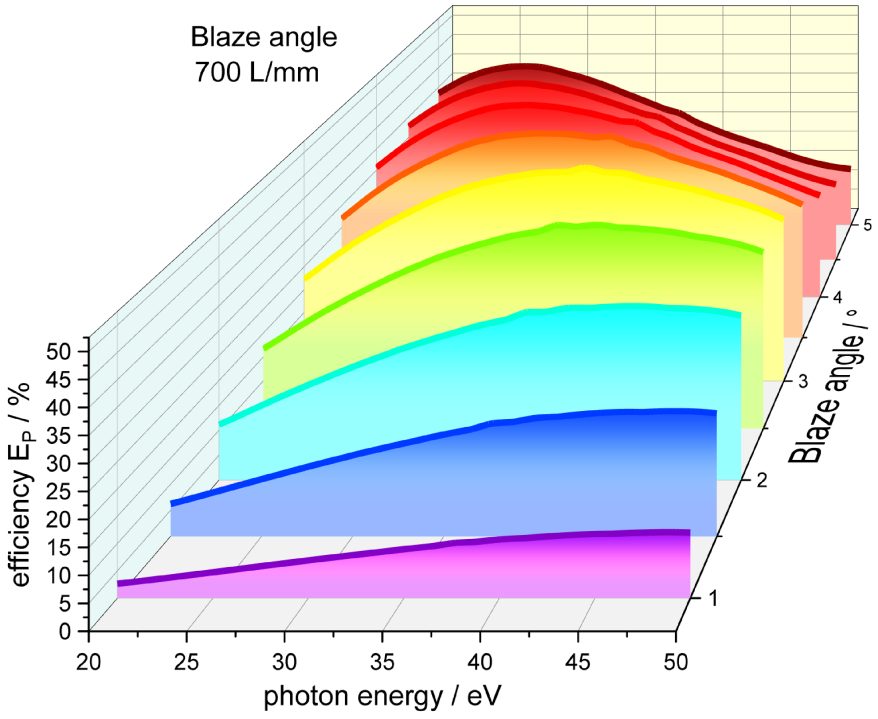


Figure A.2: Blaze Angle variation for 700 lines/mm.

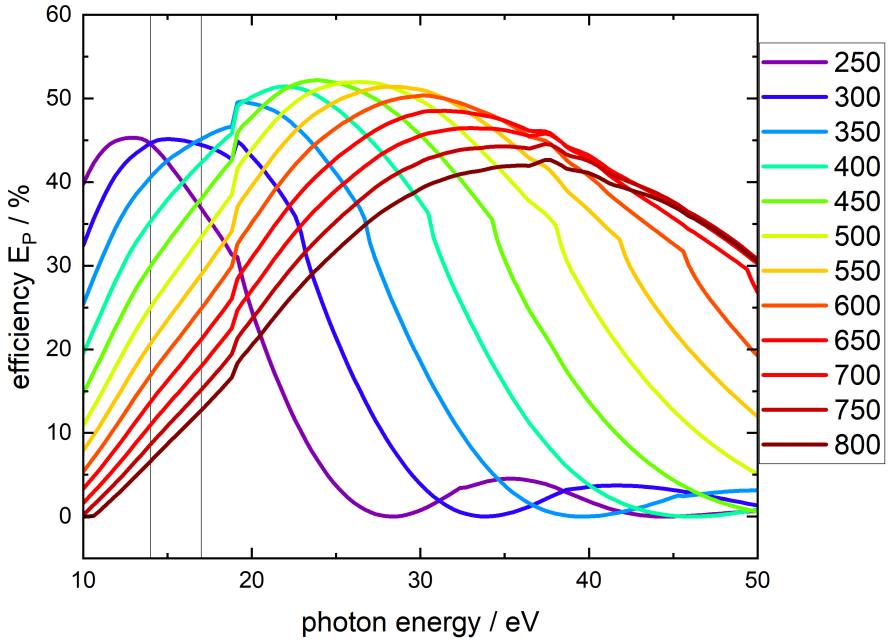


Figure A.3: Varying line densities and their efficiency for a 3.5° Grating.

Appendix B

Purity Analysis of Mg and Mn through XPS

To assess whether the source materials introduce impurities that could compromise subsequent surface experiments, both the Mg and Mn rods were analysed by X-ray Photoelectron Spectroscopy (XPS) prior to deposition. The purpose of this screening step was to verify that the source materials do not contain unintended metallic impurities that could be co-deposited and interfere with the surface experiments. In the survey spectra, only the expected signals from the base metals (Mg or Mn) and common UHV background related species (C, O, N, and Ar) were observed. No additional elements were detected.

The elemental concentrations are reported as XPS-derived atomic percentages (at.%), obtained from survey spectra using sensitivity-factor corrections.

The spectrum seen in Figure B.1 shows the magnesium measurement. It is dominated by Mg core levels and a dense manifold of Mg Auger features. In particular, when using Al Kα excitation, Mg Auger peaks populate the binding-energy range from $\sim$ 220 to 420 eV, which overlaps the expected positions of several frequently observed contaminant peaks (Ar 2p at $\sim$ 242 eV, C 1s at $\sim$ 285 eV, Ar 2s at $\sim$ 320 eV, and N 1s at $\sim$ 400 eV). As a consequence, a quantitative determination of N and Ar on the Mg rod is not reliable from survey data alone, whereas the C content can still be estimated. The compositional analysis of the Mg rod (MaTeck, 99.98%) yields predominantly Mg (89.36 at.%) with a minor oxygen

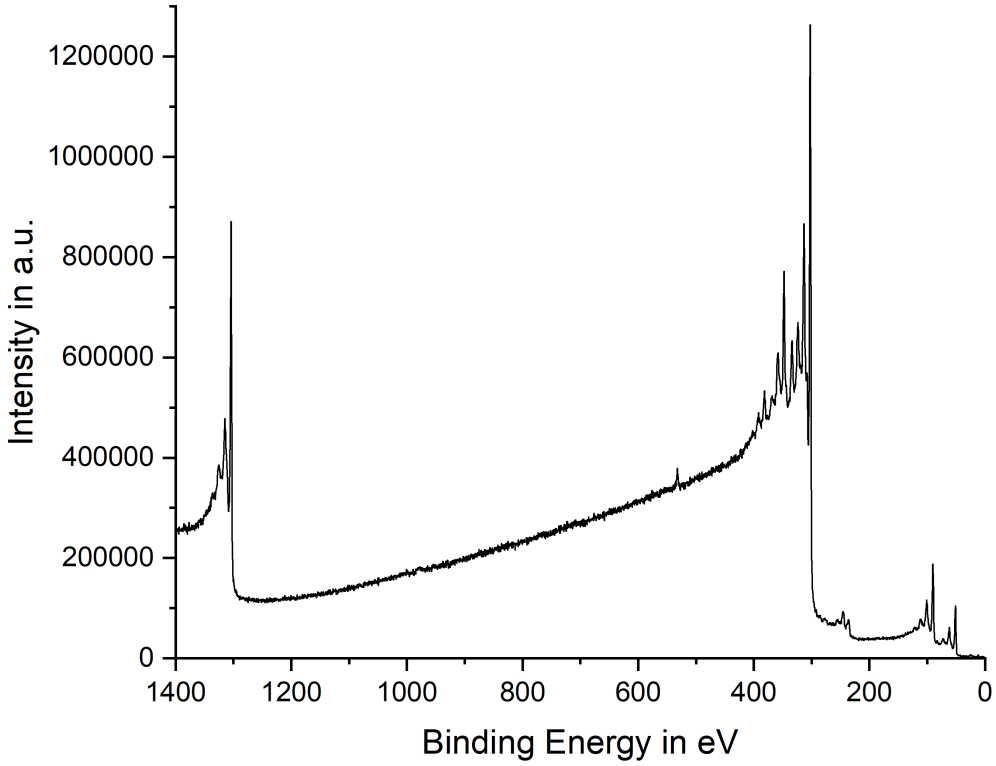


Figure B.1: XPS spectrum of Mg rod used in evaporator for preparing MgO ultra-thin films.

(6.49 at.%) and carbon (4.16 at.%) contribution. Comparison to the Moulder et al. (1995) indicates that the Mg spectral line positions and relative intensities are consistent with clean Mg, with the notable exception of an O 1s component at $\sim$ 531 eV, attributed to a thin native oxide contribution at the rod surface.

The Mn rod (Goodfellow, 99.5%) shows a similarly clean metallic composition in the sense that no additional metals are detected beyond Mn and light-element contaminants (Figure B.2). The survey spectrum contains the expected Mn features together with identifiable contributions from typical residual-gas: C 1s at $\sim$ 285 eV, Ar 2p at $\sim$ 242 eV and Ar 2s at $\sim$ 320 eV, as well as an N 1s signal near $\sim$ 398 eV. In addition, an oxygen signal is observed at $\sim$ 530 eV. Quantitatively, the Mn rod is dominated by Mn (82.3 at.%) with minor C (7.02 at.%), O (5.72 at.%), N (3.13 at.%), and Ar (1.87 at.%).

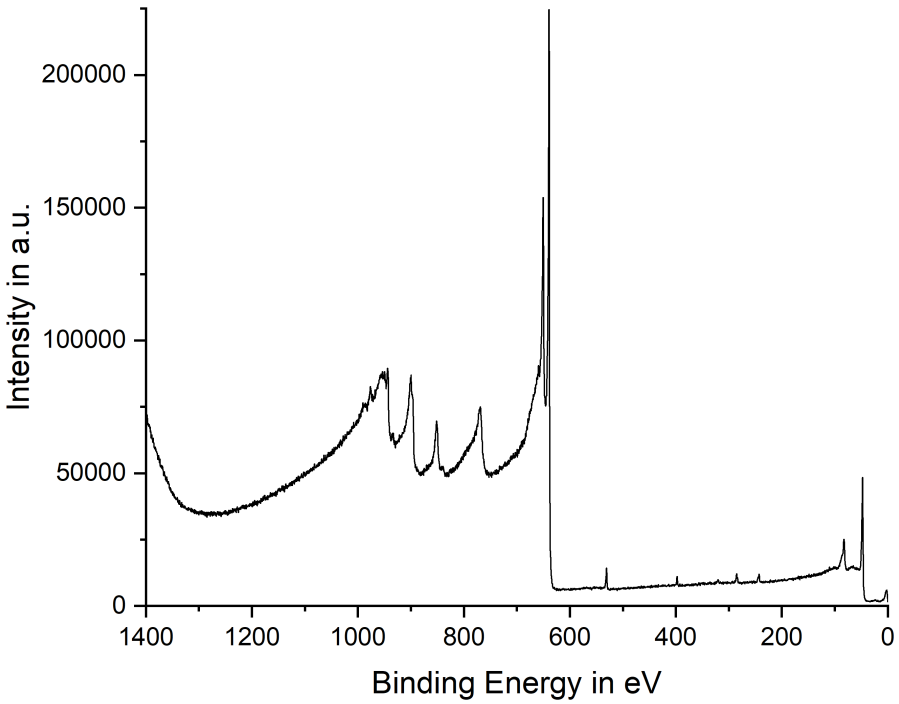


Figure B.2: XPS spectrum of Mn rod in evaporator for preparing Mn and MnO nanoparticles.

Overall, only the expected metals and the frequently found UHV species (C, O, N, Ar) were detected in the survey spectra. No additional elements were observed, in particular no foreign metals in either source material. The light element signals are attributed to surface contamination from handling and vacuum background, and Ar from sputter implantation. Therefore, the source rods are not expected to introduce unintended metallic impurities into the deposited films, and the measured purity is sufficient for the subsequent preparation and experiments.

Many thanks to the Core Facility, especially Dr. Konstantin Schüttler, for the in-house XPS Measurements.

Appendix C

TOF Uncertainty Calculation

The digitisation error was modelled as uniform within one bin, giving a standard timing uncertainty:

$$\sigma_{\mathrm{t}} = \frac{\Delta t}{\sqrt{12}} = \frac{250 \text{ ps}}{\sqrt{12}} = 72.2 \text{ ps}. \tag{C.1}$$

The electron kinetic energy E_{det} is determined from the drift time t_{drift} according to:

$$E_{\mathrm{det}} = \frac{m_{\mathrm{e}} L^2}{2e \cdot t_{\mathrm{drift}}^2}. \tag{C.2}$$

To determine the sensitivity of the energy measurement to timing uncertainties, we differentiate E_{det} with respect to t_{drift}:

$$\frac{dE_{\mathrm{det}}}{dt_{\mathrm{drift}}} = \frac{d}{dt_{\mathrm{drift}}} \left(\frac{m_{\mathrm{e}} L^2}{2e} \cdot t_{\mathrm{drift}}^{-2} \right) \tag{C.3}$$

$$= \frac{m_{\mathrm{e}} L^2}{2e} \cdot (-2 t_{\mathrm{drift}}^{-3}) \tag{C.4}$$

$$= -\frac{m_{\mathrm{e}} L^2}{e \cdot t_{\mathrm{drift}}^3}. \tag{C.5}$$

By expressing the derivative in terms of the original energy function, the relationship simplifies to:

$$\left|\frac{dE_{\mathrm{det}}}{dt_{\mathrm{drift}}}\right| = \frac{2E_{\mathrm{det}}}{t_{\mathrm{drift}}}. \tag{C.6}$$

Since the timing is governed by the kinetic energy in the drift region, the applied bias U_{bias} needs to be considered by:

$$E_{\mathrm{det}} = E_{\mathrm{sample}} + U_{\mathrm{bias}}. \tag{C.7}$$

For the Fermi cutoff this gives:

$$E_{\mathrm{max,det}} = 31.34\ \mathrm{eV} + 10\ \mathrm{eV} = 41.34\ \mathrm{eV}, \tag{C.8}$$

and for the SECO:

$$E_{\mathrm{SECO,det}} = 0.18\ \mathrm{eV} + 10\ \mathrm{eV} = 10.18\ \mathrm{eV}. \tag{C.9}$$

The drift time is calculated by:

$$t_{\mathrm{drift}} = t_{\mathrm{meas}} - t_0. \tag{C.10}$$

With $t_0 = 12.953$ ns, the measured arrival times $t_{\mathrm{max,meas}} = 167.782$ ns and $t_{\mathrm{SECO,meas}} = 324.959$ ns, are calculated to yields drift times $t_{\mathrm{max,drift}}$ and $t_{\mathrm{SECO,drift}}$:

$$t_{\mathrm{max,drift}} = 167.782\ \mathrm{ns} - 12.953\ \mathrm{ns} = 154.829\ \mathrm{ns}$$
$$t_{\mathrm{SECO,drift}} = 324.959\ \mathrm{ns} - 12.953\ \mathrm{ns} = 312.006\ \mathrm{ns}.$$

The corresponding digitisation-limited energy uncertainties follow from $\sigma_E = \left|\frac{dE}{dt}\right| \sigma_t$:

$$\sigma_{E_{\mathrm{max}}} = \frac{2E_{\mathrm{max,det}}}{t_{\mathrm{max,drift}}}\sigma_t = \frac{2 \times 41.34\ \mathrm{eV}}{154.829\ \mathrm{ns}}\,(72.2\ \mathrm{ps}) = 0.0386\ \mathrm{eV}, \tag{C.11}$$

$$\sigma_{E_{\mathrm{SECO}}} = \frac{2E_{\mathrm{SECO,det}}}{t_{\mathrm{SECO,drift}}}\sigma_t = \frac{2 \times 10.18 \text{ eV}}{312.006 \text{ ns}} (72.2 \text{ ps}) = 0.0047 \text{ eV}. \tag{C.12}$$

Finally, propagating these independent uncertainties through $\Phi = h\nu - E_{\mathrm{max}} + E_{\mathrm{SECO}}$ gives:

$$\sigma_\Phi = \sqrt{\sigma_{E_{\mathrm{max}}}^2 + \sigma_{E_{\mathrm{SECO}}}^2} = \sqrt{(0.0386 \text{ eV})^2 + (0.0047 \text{ eV})^2} \approx 0.04 \text{ eV}. \tag{C.13}$$

It is important to note, the standard uncertainty (1σ) is a lower bound set by the detector time-bin width and does not include systematic contributions from cutoff fitting or low-energy transmission.

Acknowledgments

Above all, I would like to thank Professor Dr. Thorsten Bernhardt from the bottom of my heart, for having offered me the opportunity to delve into physical chemistry without hesitation. His open door policy, perennial fascination and undying curiosity have kept me motivated to put this project together even in the toughest of times.

I would not be writing this if it were not for Dr. Alahmed Qutaish. Thank you for your repeated insisting of me to return to academia.

To my fearless colleagues and their apparatuses: Prof. Dr. Sandra Lang (on Claudette), and Dr. Pavol Mikolaj (on Wuhan) and our former colleague Bianca Ghejan, who have never stopped offering their support, good company and food, even on the worst of days. To our newcomers Robert Koch (on Claudette) and Leo Niedringhaus (on Otto) I wish the very best.

I must also thank PD Dr. Joachim Bansmann for introducing me to his former colleague Dr. Franz Schäfers[13]. His programs Ray and Reflec have caused me an incredible ammount of headaches during my first year. As I had the great honour of meeting Franz in person, I was able to confront him with all my questions, as we both figured out the best possible raytracing for this project. I was in tears after understanding and mastering "the program with the many questions" as Ray is often referred to. I will remember Franz as an incredibly kind and humble man.

An extraordinarily big thank you to Alexander Pilz from Pilz Optics, who has not only connected me to the optics world, but also helped me in specifying my optics and manufacturing them. He introduced me to Prof. Dr. Marcus Lörgen and Dr. Stephanie Lemke, whose Team has manufactured the dual track precision grating for my beamline.

The whole apparatus has Tom Hall's[25] fingerprints all over it. Thank you so much for the caring support and kind phonecalls.

A very big thanks to Bartek Checinski[5] for his patience in supporting me to operate the AES/LEED device. Without his fast aid, I would have never managed to record a single spectra.

Allow me to thank the students I had the privilege of supervising. They have furthered my learning and growth over the course of the last few years and have aided me tremendously:

Bachelor: Vanessa Traub (2022), Nina Hornberger (2023), Luca Pallini (2024), Leonie Hintermayr (2025), Leni Lauber (2025), Julia Fokt (2025)

Master: Jessica Loske (2021), Darius Hübner (2022), Kim Junginger (2022), Michael Kohler (2023), Silvia Katolla (2024), Dana-Marie Koll (2025)

I would be remiss not to mention my sincere thanks to the following individuals, whose contributions greatly lead to the realization and success of my work:

Prof. Dr. Mihai Vaida
Dr. Aakash Gupta
Prof. Dr. Markus Gühr
Prof. Dr. L. Robert Baker
Dr. Emily Hruska
Prof. Dr. Philip Howard Bucksbaum
Dr. Frederick August Weihe
Prof. Dr. Angus Bain
Prof. Dr. Ulf Kleineberg
Prof. Dr. Anne Harth
Dr. Andrey Sokolov[13]
Dr. Peter Baumgärtel[13]
Dr. Grzegorz Gwalt[13]
Dr. Konstantin Schüttler
Dr. Rolf Follath
Dr. Bruno Nelles

Jakob Hirlinger-Alexander
Agnes Keller & Laurin Wolf
Iris Terwedow-Müller & Inge Kasberger
Jochen Mannes

Our Technicians and Workshop members:

Gerd Bräth
Thomas Häring
Bernd Folli
Christian Weich
Jürgen Steck
Wolfgang Rapp
Hartmut Steeb
Thomas Kraft
Jonas Geißel
Reinhard Liske
Jürgen Haringer
Klaus Mammel
Leonhard Waigel
... and many more behind the scenes.

My Industry Contacts:
Norman Niewrzella[1]
Johannes Weiss[2]
Phil Marston[3]
Jürgen Enzinger & Ilka Priest[4]
Thomas Niedermayer[5]

Uwe Hasse[5]
Sebastian Glasl[6]
Martin Steck[7]
Jürgen Hartmann[8]
Julia Soschinski & Petra Schöttner[9]
Lina Calderon[10]
Didem Sener[11]
Harry & Margot Juraschek[12]
Lioba Zeiss[13]
Henner Befort[14]
Michaela Prinz[15]
Mareike Schmelz[6]
Domantas Čiapas[16]
Tomofumi Seto[17]
Dr. Daniela Kern-Michler[18]
Dr. Vincenzo Talluto[18]
Dr. Ralf Tölle[19]
Dr. René Lewinski[20]
Dr. Wolfgang Wagner[21]
Dr. Sebastian Riese[22]
Dr. Patrizia Ferrero[23]
Dr. Christian Vetter[24]

I am endebted to all my former educators for all their time and teaching.
I want to specifically mention:

Prof. Dr. Norbert Kniffler
Prof. Dr. Dennis Trebbels
Prof. Dr. Götz Lipphardt
Prof. Dr. Klaus Iselborn
Prof. Dr. Steffen Elschner
Prof. Dr. Thomas Hunger
Prof. Dr. Hermann Merz
Prof. Dr. Al-Thaddeus Avestruz
Richard Butemann
Ina-Marie Gorgis
Gregor Slosarek
Steve Hopkins
Lucinda Scott-Kellermeier

To Yvonne Cupp and Lee Beckley, my high school teachers, who were kind (and brave) enough to review this draft.

Thanks to all companies that endured my peculiar requests and delivered custom solutions. Without their products, my work could not exist.

Thorlabs GmbH

Torr Scientific Ltd.[3]

Leybold GmbH[6]

Rohde und Schwarz International GmbH

SI Scientific Instruments GmbH

Tectra GmbH[5]

OCI Vacuum Microengineering Inc.[25]

arnotec GmbH

FAST ComTec Communication Technology GmbH[21]

Edmund Optics Ltd.

Carl Zeiss SMT GmbH[1]

Lebow Company[10]

TROTEC GmbH

FMB Feinwerk- und Meßtechnik GmbH

Helmholtz-Zentrum Berlin[26]

MKS Instruments[18]

Kurt J. Lesker Company Ltd.[4]

Rosch Computer GmbH[11]

Pfeiffer Vacuum[2]

OEC GmbH[12]

Scienta Omicron[9]

VACPRO ApS

Befort Wetzlar Optik - OD GmbH[14]

VWR International, LLC.[7]

Suflix

FRANTOS GmbH & Co. KG

MDC Precision[27]

HORNBACH Baumarkt AG

ARLT Computer-Produkte GmbH

Conrad Electronic SE

Thomann GmbH

MaTecK Material-Technologie & Kristalle GmbH[15]

EKSMA Optics[16]

Hartmann Business Solutions[8]

Shimadzu Europa GmbH[17]

WBS Tech GmbH

Pleiger Laseroptik GmbH & Co. KG[19]

ProxiVision GmbH[20]

Gaßmann GmbH

Farnell GmbH

HORST GmbH[13]

VACOM Vakuum Komponenten & Messtechnik GmbH[23]

RIEGLER & Co. KG

Zoch GmbH & Co. KG

HTM GmbH & Co. KG

foxiflex GmbH & Co. KG

DHL International GmbH

Gaßmann GmbH

Fraunhofer Institute for Applied Optics and Precision Engineering IOF[24]

Gebr. Rettberg GmbH

Arun Microelectronics Ltd.

Wissel GmbH

Carl Roth GmbH + Co. KG

Pegasus Solutions GmbH

Meyer Industrie Electronic GmbH

Becker & Hickl GmbH

Acal BFi Germany GmbH

Quantum Design GmbH

Schwer Fittings GmbH

WBS Tech GmbH

Thermo Fisher Scientific

LAYERTEC GmbH[22]

My final acknowledgments I address to my loving parents Lidija & Dirk and dear friends. Thank you for keeping me grounded, for believing in me when the work felt endless, and (gospodin O. Lakovic, and C.D.Diehm) for reminding me that there is a life outside the lab.

Bibliography

Agostini, P. and DiMauro, L. F. (2004). Corrigendum: The physics of attosecond light pulses. *Rep. Prog. Phys.*, 67:1563.

Arun Microelectronics Ltd. (2022). *AIGxG Ion Gauge: UHV Bayard–Alpert Ion Gauge, User Manual*. Issue 20220726.

Auger, P. (1925). Sur l'effet photoélectrique composé. *J. Phys. Radium*, 6:205.

Baddorf, A. P. (2023). Identifying the secondary electron cutoff in ultraviolet photoemission spectra for work function measurements of non-ideal surfaces. *Sci. Rep.*, 13:13452.

Baktash, E., Zaharieva, I., Schröder, M., Goebel, C., Dau, H., and Thomas, A. (2013). Cyanamide route to calcium–manganese oxide foams for water oxidation. *Dalton Trans.*, 42:16920.

Bauer, E. (1987). G. Ertl, J. Küppers: Low energy electrons and surface chemistry, second, completely revised edition, VCH Verlagsgesellschaft, Weinheim 1985. *Ber. Bunsenges. Phys. Chem.*, 91:167.

Bauer, M. (2005). Femtosecond ultraviolet photoelectron spectroscopy of ultra-fast surface processes. *J. Phys. D: Appl. Phys.*, 38:R253.

Bauer, M., Lei, C., Read, K., Tobey, R., Gland, J., Murnane, M. M., and Kapteyn, H. C. (2001). Direct observation of surface chemistry using ultrafast soft-X-Ray pulses. *Phys. Rev. Lett.*, 87:025501.

Baumgärtel, P., Witt, M., Baensch, J., Fabarius, M., Erko, A., Schäfers, F., and Schirmacher, H. (2016). Ray-UI: A powerful and extensible user interface for RAY. *AIP Conf. Proc.*, 1741:040016.

Benia, H. M., Myrach, P., Nilius, N., and Freund, H.-J. (2010). Structural and electronic characterization of the MgO/Mo(001) interface using STM. *Surf. Sci.*, 604:435.

Benigna, J. (2014). Photoelectron spectroscopy in advanced placement chemistry. *J. Chem. Educ.*, 91:1299.

Berg, J. M., Tymoczko, J. L., Gatto, G. J., and Stryer, L. (2018). *Stryer Biochemie*. Springer.

Berge, S., Gartland, P. O., and Slagsvold, B. J. (1974). Photoelectric work function of a molybdenum single crystal for the (100), (110), (111), (112), (114), and (332) faces. *Surf. Sci.*, 43:275.

Bernstein, R. B. and Zewail, A. H. (1989). Femtosecond real-time probing of reactions. III. inversion to the potential from femtosecond transition-state spectroscopy experiments. *J. Chem. Phys.*, 90:829.

Bohling, C. and Sigmund, W. (2016). Self-limitation of native oxides explained. *Silicon*, 8:339.

Brabec, T. and Krausz, F. (2000). Intense few-cycle laser fields: Frontiers of nonlinear optics. *Rev. Mod. Phys.*, 72:545.

Brimblecombe, R., Swiegers, G. F., Dismukes, G. C., and Spiccia, L. (2008). Sustained water oxidation photocatalysis by a bioinspired manganese cluster. *Angew. Chem. Int. Ed.*, 47:7335.

Carl Zeiss SMT GmbH (2016). Mirrors for Synchrotron Radiation: Technical Information. Technical report, ZEISS Gruppe, Rudolf-Eber-Straße 2, 73447 Oberkochen, Germany.

Casu, M. B. and Chassé, T. (2014). *Photoelectron Spectroscopy Applications to Materials Science*, chapter 45, page 1523. John Wiley & Sons, Ltd.

Chell Instruments Ltd (2026). Chell instruments.

Cinti, R. C., Khoury, E. A., Chakraverty, B. K., and Christensen, N. E. (1976). Directional UV photoemission from (100) and (110) molybdenum surfaces. *Phys. Rev. B*, 14:3296.

Coccia, E. and Luppi, E. (2022). Time-dependent ab initio approaches for high-harmonic generation spectroscopy. *J. Phys. Condens. Matter*, 34:073001.

Cohen-Tannoudji, C., Diu, B., and Laloë, F. (2020). *Quantenmechanik: Band 3: Fermionen, Bosonen, Photonen, Korrelationen und Verschränkung*. De Gruyter.

Constant, E., Garzella, D., Breger, P., Mével, E., Dorrer, C., Blanc, C. L., Salin, F., and Agostini, P. (1999). Optimizing high harmonic generation in absorbing gases: Model and experiment. *Phys. Rev. Lett.*, 82:1668.

Corkum, P. B. (1993). Plasma perspective on strong field multiphoton ionization. *Phys. Rev. Lett.*, 71:1994.

Corneille, J. S., He, J.-W., and Goodman, D. W. (1994). XPS characterization of ultra-thin mgo films on a Mo(100) surface. *Surf. Sci.*, 306:269.

Davis, J., Palmberg, P., Riach, D., and Weber, L. (1976). *Handbook of Auger Electron Spectroscopy*. Perkin-Elmer, Edina, Minnesota.

DIN (2014). International electrotechnical vocabulary – part 351: Control technology (IEC 60050-351:2013). Technical report, DIN / IEC.

Ede, S. R. and Luo, Z. (2021). Tuning the intrinsic catalytic activities of oxygen-evolution catalysts by doping: a comprehensive review. *J. Mater. Chem. A*, 9:20131.

Einstein, A. (1905). Über einen die Erzeugung und Verwandlung des Lichtes betreffenden heuristischen Gesichtspunkt. *Ann. Phys.*, 322:132.

Ferray, M., L'Huillier, A., Li, X. F., Lompré, L. A., Mainfray, G., and Manus, C. (1988). Multiple-harmonic conversion of 1064 nm radiation in rare gases. *J. Phys. B.*, 21:L31.

Frassetto, F., Cacho, C., Froud, C. A., Turcu, I. C. E., Villoresi, P., Bryan, W. A., Springate, E., and Poletto, L. (2011). Single-grating monochromator for extreme-ultraviolet ultrashort pulses. *Opt. Express.*, 19:19169.

Freund, A. K. (1989). *X-Ray Optics for Synchrotron Radiation*, page 255. Springer US, Boston, MA.

Frietsch, B., Carley, R., Döbrich, K., Gahl, C., Teichmann, M., Schwarzkopf, O., Wernet, P., and Weinelt, M. (2013). A high-order harmonic generation apparatus for time- and angle-resolved photoelectron spectroscopy. *Rev. Sci. Instrum.*, 84:075106.

Fujimori, A., Kimizuka, N., Akahane, T., Chiba, T., Kimura, S., Minami, F., Siratori, K., Taniguchi, M., Ogawa, S., and Suga, S. (1990). Electronic structure of MnO. *Phys. Rev. B*, 42:7580.

Gallmann, L., Cirelli, C., and Keller, U. (2012). Attosecond science: Recent highlights and future trends. *Annu. Rev. Phys. Chem.*, 63:447.

Gangopadhyay, S., Kaloni, T. P., Schwingenschlögl, U., and Jones, B. A. (2020). Site dependency of the magnetism for Mn adsorption on MgO/Ag(001): a combined DFT+U and STM investigation.

Geneaux, R., Marroux, H. J. B., Guggenmos, A., Neumark, D. M., and Leone, S. R. (2019). Transient absorption spectroscopy using high harmonic generation: a review of ultrafast X-raydynamics in molecules and solids. *Phil. Trans. R. Soc. A.*, 377:20170463.

Godowski, P. J. and Hardegree, E. L. (1994). Determination of submonolayer coverages using auger escape depths. *Acta Phys. Pol. A.*, 85:843.

Goodfellow Cambridge Ltd (2026). Manganese rod.

Gorlin, Y. and Jaramillo, T. F. (2010). A bifunctional nonprecious metal catalyst for oxygen reduction and water oxidation. *J. Am. Chem. Soc.*, 132:13612.

Greenwood, N. N. and Earnshaw, A. (1997). *Chemistry of the Elements*. Butterworth-Heinemann, 2nd edition.

Gunawardane, R. P. and Arumainayagam, C. R. (2006). *Auger Electron Spectroscopy*, page 451. Springer US, Boston, MA.

Hecht, E. (2023). *Optik*. De Gruyter Oldenbourg, 8 edition.

Helander, M. G., Greiner, M. T., Wang, Z. B., and Lu, Z. H. (2010). Pitfalls in measuring work function using photoelectron spectroscopy. *Appl. Surf. Sci.*, 256:2602.

Hellmann, S., Rossnagel, K., Marczynski-Bühlow, M., and Kipp, L. (2009). Vacuum space-charge effects in solid-state photoemission. *Phys. Rev. B*, 79:035402.

Helmreich, R., Classen, A., and Fauster, T. (2021). Negative electron affinity opens quantum well in MgO layers on Ag(100). *J. Phys. Condens. Matter*, 34:045001.

Hengehold, R. L. and Pedrotti, F. L. (1976). Plasmon excitation energies in ZnO, CdO, and MgO. *J. Appl. Phys.*, 47:287.

Hentschel, M., Kienberger, R., Spielmann, C., Reider, G. A., Milosevic, N., Brabec, T., Corkum, P., Heinzmann, U., Drescher, M., and Krausz, F. (2001). Attosecond metrology. *Nature*, 414:509.

Hertz, H. (1887). Ueber einen Einfluss des ultravioletten Lichtes auf die electrische Entladung. *Ann. Phys.*, 267:983.

Hove, M. A. V. and Somorjai, G. A. (1994). Adsorption and adsorbate-induced restructuring: a LEED perspective. *Surf. Sci.*, 299-300:487.

Hruska, E., Husek, J., Bandaranayake, S., and Baker, L. R. (2022). Visible light absorption and hot carrier trapping in anatase TiO2: The role of surface oxygen vacancies. *J. Phys. Chem. C*, 126:10752.

Hüfner, S. (1996). *Photoelectron Spectroscopy: Principles and Applications*, volume 82 of *Springer Series in Solid-State Sciences*. Springer, Berlin, Heidelberg.

Hüfner, S. (2007). *Very High Resolution Photoelectron Spectroscopy*. Springer Berlin Heidelberg, Berlin, Heidelberg.

Ikeda, K., Tachibana, T., and Manome, Y. (2017). The applications, neurotoxicity, and related mechanisms of manganese-containing nanoparticles. In *Neurotoxicity of Nanomaterials and Nanomedicine*, page 205. AP.

Imhof, R. E., Adams, A., and King, G. C. (1976). Energy and time resolution of the 180 degrees hemispherical electrostatic analyser. *J. Phys. E: Sci. Instrum.*, 9:138.

Indra, A., Menezes, P. W., Zaharieva, I., Baktash, E., Pfrommer, J., Schwarze, M., Dau, H., and Driess, M. (2013). Active mixed-valent MnOx water oxidation catalysts through partial oxidation (corrosion) of nanostructured MnO particles. *Angew. Chem. Int. Ed.*, 52:13206.

Itatani, J., Levesque, J., Zeidler, D., Niikura, H., Pépin, H., Kieffer, J. C., Corkum, P. B., and Villeneuve, D. M. (2004). Tomographic imaging of molecular orbitals. *Nature*, 432:867.

Itatani, J., Quéré, F., Yudin, G. L., Ivanov, M. Y., Krausz, F., and Corkum, P. B. (2002). Attosecond streak camera. *Phys. Rev. Lett.*, 88:173903.

Jackson, J. D. (1975). *Classical Electrodynamics*. Wiley, second edition.

Jaouen, T., Jézéquel, G., Delhaye, G., Lépine, B., Turban, P., and Schieffer, P. (2010). Work function shifts, schottky barrier height, and ionization potential determination of thin MgO films on Ag(001). *Appl. Phys. Lett.*, 97:232104.

Kabir, M., Mookerjee, A., and Kanhere, D. G. (2006). Structure, electronic properties, and magnetic transition in manganese clusters. *Phys. Rev. B*, 73:224439.

Kapteyn, H. C., Murnane, M. M., and Christov, I. P. (2005). Extreme nonlinear optics: Coherent x rays from lasers. *Phys. Today.*, 58:39.

KEMET Electronics Corporation (2025). *Surface Mount Multilayer Ceramic Chip Capacitors (SMD MLCCs) – C0G with KONNEKT™ Technology, 10–3,000 VDC*.

Knickelbein, M. B. (2001). Experimental observation of superparamagnetism in manganese clusters. *Phys. Rev. Lett.*, 86:5255.

Knickelbein, M. B. (2004). Magnetic ordering in manganese clusters. *Phys. Rev. B*, 70:014424.

Kolasinski, K. W. (2012). *Surface Science: Foundations of Catalysis and Nanoscience*. John Wiley & Sons, Ltd.

Kothe, A., Metje, J., Wilke, M., Moguilevski, A., Engel, N., Al-Obaidi, R., Richter, C., Golnak, R., Kiyan, I. Y., and Aziz, E. F. (2013). Time-of-flight electron spectrometer for a broad range of kinetic energies. *Rev. Sci. Instrum.*, 84:023106.

Kramida, A., Ralchenko, Y., Reader, J., and Team, N. A. (2024). Nist atomic spectra database (ver. 5.12). National Institute of Standards and Technology, Gaithersburg, MD.

Kruit, P. and Read, F. H. (1983). Magnetic field paralleliser for 2π electron-spectrometer and electron-image magnifier. *J. Phys. E: Sci. Instrum.*, 16:313.

Kumar, J. (2018). Photoelectron spectroscopy: Fundamental principles and applications. In *Handbook of Materials Characterization*. Springer International Publishing.

Kurahashi, N., Thürmer, S., Liu, S. Y., Yamamoto, Y., Karashima, S., Bhattacharya, A., Ogi, Y., Horio, T., and Suzuki, T. (2021). Design and characterization of a magnetic bottle electron spectrometer for time-resolved extreme UV and X-ray photoemission spectroscopy of liquid microjets. *SDY*, 8:034303.

Labaye, F., Gaponenko, M., Modsching, N., Brochard, P., Paradis, C., Schilt, S., Wittwer, V. J., and Sudmeyer, T. (2019). Xuv sources based on intra-oscillator high harmonic generation with thin-disk lasers: Current status and prospects. *IEEE J. Sel. Top. Quantum Electron.*, 25:1.

Lescop, B. (2006). Initial oxidation of mn surface studied by ultraviolet photoelectron spectroscopy and metastable induced electron spectroscopy. *Appl. Surf. Sci.*, 252:2276.

Lewenstein, M., Balcou, P., Ivanov, M. Y., L'Huillier, A., and Corkum, P. B. (1994). Theory of high-harmonic generation by low-frequency laser fields. *Phys. Rev. A.*, 49:2117.

León, I., Yang, Z., Liu, H.-T., and Wang, L.-S. (2014). The design and construction of a high-resolution velocity-map imaging apparatus for photoelectron spectroscopy studies of size-selected clusters. *Rev. Sci. Instrum.*, 85:083106.

Lide, D. R., editor (2000). *CRC Handbook of Chemistry and Physics*. CRC Press, Boca Raton, FL, 81st edition.

Lu, Y., Assi, C. K., Breton, J. C. L., Turban, P., Lépine, B., Schieffer, P., and Jézéquel, G. (2006). Electronic properties of metal/MgO(001) interfaces. *J. Phys. IV France*.

MacRae, A. U. (1963). Low-energy electron diffraction. *Science*, 139:379.

Mateck GmbH (2026). Mateck products.

McPherson, A., Gibson, G., Jara, H., Johann, U., Luk, T. S., McIntyre, I. A., Boyer, K., and Rhodes, C. K. (1987). Studies of multiphoton production of vacuum-ultraviolet radiation in the rare gases. *J. Opt. Soc. Am. B*, 4:595.

Melder, J., Bogdanoff, P., Zaharieva, I., Fiechter, S., Dau, H., and Kurz, P. (2020). Water-oxidation electrocatalysis by manganese oxides: Syntheses, electrode preparations, electrolytes and two fundamental questions. *Z. Phys. Chem.*, 234:925.

Mendis, B. G. (2021). Surface core hole electron energy-loss fine structure in MgO: Experiment and theory. *Microsc. Microanal.*, 27:1316.

Mikušik, P., Nyholm, R., and Mårtensson, N. (1981). Valence band of molybdenum by photoelectron spectroscopy. *Czech. J. Phys. B*, 31:1165.

Moharam, M. G. and Gaylord, T. K. (1981). Rigorous coupled-wave analysis of planar-grating diffraction. *J. Opt. Soc. Am.*, 71:811.

Moulder, J. F., Chastain, J., and King, R. C., editors (1995). *Handbook of X-Ray Photoelectron Spectroscopy: A Reference Book of Standard Spectra for Identification and Interpretation of XPS Data*. Physical Electronics Division, Perkin-Elmer Corp., Eden Prairie, MN.

Musket, R. G., McLean, W., Colmenares, C. A., Makowiecki, D. M., and Siekhaus, W. J. (1982). Preparation of atomically clean surfaces of selected elements: A review. *Appl. Surf. Sci.*, 10:143.

Möller, C., Barreto, J., Stavale, F., and Nilius, N. (2019). Manganese oxide thin films on Au(111): Growth competition between MnO and Mn3O4. *J. Phys. Chem. C*, 123:7665.

Müller, M., Neel, N., Crampin, S., and Kroger, J. (2016). Lateral electron confinement with open boundaries: Quantum well states above nanocavities at Pb(111). *Phys. Rev. Lett.*, 117:136803.

Nandi, S., Plésiat, E., Zhong, S., Palacios, A., Busto, D., Isinger, M., Neoričić, L., Arnold, C. L., Squibb, R. J., Feifel, R., Decleva, P., L'Huillier, A., Martín, F., and Gisselbrecht, M. (2020). Attosecond timing of electron emission from a molecular shape resonance. *Sci. Adv.*, 6:eaba7762.

Nayak, J., Rai, A., D'Souza, S. W., Maniraj, M., and Barman, S. R. (2012). Mn deposition on Ni_2MnGa(100). *AIP Conf. Proc.*, 1447:717.

Paggel, J. J., Miller, T., and Chiang, T.-C. (1999). Quantum-well states as fabry-pérot modes in a thin-film electron interferometer. *Science*, 283:1709.

Pal, J., Smerieri, M., Celasco, E., Savio, L., Vattuone, L., Ferrando, R., Tosoni, S., Giordano, L., Pacchioni, G., and Rocca, M. (2014). How growing conditions and interfacial oxygen affect the final morphology of MgO/Ag(100) films. *J. Phys. Chem. C*, 118:26091.

Palmer, C. (2014). *Diffraction Grating Handbook (7th edition)*. Newport Corporation.

Patchkovskii, S., Zhao, Z., Brabec, T., and Villeneuve, D. M. (2006). High harmonic generation and molecular orbital tomography in multielectron systems: Beyond the single active electron approximation. *Phys. Rev. Lett.*, 97:123003.

Paulus, A., Winterfeldt, C., Pfeifer, T., Walter, D., Gerber, G., and Spielmann, C. (2006). Novel time-of-flight electron spectrometer optimized for time-resolved soft-X-ray photoelectron spectroscopy. *Rev. Sci. Instrum.*, 77:043105.

Pendry, J. B. (1974). *Low Energy Electron Diffraction: The Theory and Its Application to Determination of Surface Structure*. Academic Press.

Photonis (2024). Microchannel plates.

Polanyi, J. C. and Zewail, A. H. (1995). Direct observation of the transition state. *Acc. Chem. Res.*, 28:119.

Poletto, L., Miotti, P., Frassetto, F., Spezzani, C., Grazioli, C., Coreno, M., Ressel, B., Gauthier, D., Ivanov, R., Ciavardini, A., de Simone, M., Stagira, S., and Ninno, G. D. (2014). Double-configuration grating monochromator for extreme-ultraviolet ultrafast pulses. *Appl. Opt.*, 53:5879.

Poletto, L., Villoresi, P., and Frassetto, F. (2010). Diffraction gratings for the selection of ultrashort pulses in the extreme-ultraviolet. In *Advances in Solid State Lasers*, chapter 18. IntechOpen, Rijeka.

Prada, S., Martinez, U., and Pacchioni, G. (2008). Work function changes induced by deposition of ultrathin dielectric films on metals: A theoretical analysis. *Phys. Rev. B*, 78:235423.

Purcell, E. M. (1938). The focusing of charged particles by a spherical condenser. *Phys. Rev.*, 54:818.

Reinert, F. and Hüfner, S. (2005). Photoemission spectroscopy—from early days to recent applications. *New J. Phys.*, 7:97.

Rife, J. C. (2000). Optical materials—UV, VUV. In *Electro-Optics Handbook*, chapter 10. McGraw-Hill, 2 edition.

Rogers, L. C. G. and Rhead, G. E. (1990). Statistical analysis of auger electron spectroscopy data for thin film growth modes. *Thin Solid Films*, 188:109.

Rohde & Schwarz (2025). R&S MXO 4 Oscilloscope.

Rundquist, A., Chang, Z., Wang, H., Christov, I., Kapteyn, H. C., and Murnane, M. M. (1998a). Coherent X-ray generation at 2.7 nm using 25 fs laser pulses. In *AIP Conference Proceedings*.

Rundquist, A., Durfee, C. G., Chang, Z., Herne, C., Backus, S., Murnane, M. M., and Kapteyn, H. C. (1998b). Phase-matched generation of coherent soft x-rays. *Science*, 280:1412.

Salières, P., L'Huillier, A., Antoine, P., and Lewenstein, M. (1999). Study of the spatial

and temporal coherence of high-order harmonics. In *Advances in Atomic, Molecular, and Optical Physics*, volume 41, page 83. AP.

Samarin, S. N., Artamonov, O. M., Waterhouse, D. K., Kirschner, J., Morozov, A., and Williams, J. F. (2003). Highly efficient time-of-flight spectrometer for studying low-energy secondary emission from dielectrics: Secondary-electron emission from LiF film. *Rev. Sci. Instrum.*, 74:1274.

Santis, M. D., Langlais, V., Schneider, K., and Torrelles, X. (2021). Growth-mode and interface structure of epitaxial ultrathin MgO/Ag(001) films. *J. Phys. Condens. Matter*, 33:265002.

Savitzky, A. and Golay, M. J. E. (1964). Smoothing and differentiation of data by simplified least squares procedures. *Anal. Chem.*, 36:1627.

Schafer, K. J., Yang, B., DiMauro, L. F., and Kulander, K. C. (1993). Above threshold ionization beyond the high harmonic cutoff. *Phys. Rev. Lett.*, 70:1599.

Schultz, T. (2022). A unified secondary electron cut-off presentation and common mistakes in photoelectron spectroscopy. *Electron. Struct.*, 4:044002.

Schäfers, F. (1996). The bessy raytrace program to calculate synchrotron radiation beamlines. Technical report, BESSY GmbH, Berlin, Germany. Version from 05.04.2004.

Seah, M. P. (1984). A review of the analysis of surfaces and thin films by AES and XPS. *Vacuum*, 34:463.

Seah, M. P. and Dench, W. A. (1979). Quantitative electron spectroscopy of surfaces: A standard data base for electron inelastic mean free paths in solids. *Surf. Interface Anal.*, 1:2.

Shukla, A. K., Banik, S., Dhaka, R. S., Biswas, C., Barman, S. R., and Haak, H. (2004). Versatile UHV compatible knudsen type effusion cell. *Rev. Sci. Instrum.*, 75:4467.

Sokolov, A., Sertsu, M. G., Gaupp, A., Lüttecke, M., and Schäfers, F. (2018). Efficient high-order suppression system for a metrology beamline. *J. Synchrotron Radiat.*, 25:100.

Spectra-Physics (2026). Ultrafast pump lasers.

Spielmann, C., Burnett, N., Sartania, S., Koppitsch, R., Schnürer, M., Kan, C., Lenzner, M., Wobrauschek, P., and Krausz, F. (1997). Generation of coherent x-rays in the water window using 5-femtosecond laser pulses. *Science*, 278:661.

Strickland, D. and Mourou, G. (1985). Compression of amplified chirped optical pulses. *Opt. Commun.*, 56:219.

Sundar, S., Banik, S., Chandra, L. S. S., Chattopadhyay, M. K., Ganguli, T., Lodha, G. S., Pandey, S. K., Phase, D. M., and Roy, S. B. (2016). Electronic structure of Mo1-xRex alloys studied through resonant photoemission spectroscopy. *J. Phys. Condens. Matter*, 28:315502.

Sutherland, J. R., Christensen, E. L., Powers, N. D., Rhynard, S. E., Painter, J. C., and

Peatross, J. (2004). High harmonic generation in a semi-infinite gas cell. *Opt. Express*, 12:4430.

Tjeng, L. H., Vos, A. R., and Sawatzky, G. A. (1990). Electronic structure of MgO studied by angle-resolved ultraviolet photoelectron spectroscopy. *Surf. Sci.*, 235:269.

Tong, X. M. and Chu, S. I. (1998). Time-dependent density-functional theory for strong-field multiphoton processes: Role of dynamical electron correlation in multiple high-order harmonic generation. *Phys. Rev. A*, 57:452.

Vaida, M. E. (2010). *PhD Thesis*. PhD thesis, University of Ulm, Ulm.

Vaida, M. E. and Bernhardt, T. M. (2010). Surface pump-probe femtosecond-laser mass spectrometry: Time-, mass-, and velocity-resolved detection of surface reaction dynamics. *Rev. Sci. Instrum.*, 81:104103.

Vaida, M. E., Bernhardt, T. M., Barth, C., Esch, F., Heiz, U., and Landman, U. (2010). Ultrathin magnesia films as support for molecules and metal clusters: Tuning reactivity by thickness and composition. *Phys. Status Solidi B.*, 247:1001.

Vaida, M. E., Gleitsmann, T., Tchitnga, R., and Bernhardt, T. M. (2009). Femtosecond-laser photoemission spectroscopy of Mo(100) covered by ultrathin MgO(100) films of variable thickness. *J. Phys. Chem. C*, 113:10264.

Vaida, M. E. and Leone, S. R. (2016). Femtosecond extreme ultraviolet photoemission spectroscopy: Observation of ultrafast charge transfer at the n-TiO2/p-Si(100) interface with controlled TiO2 oxygen vacancies. *J. Phys. Chem. C*, 120:2769.

Vaida, M. E., Rawal, T. B., Bernhardt, T. M., Marsh, B. M., Rahman, T. S., and Leone, S. R. (2022). Nonmetal-to-metal transition of magnesia supported Au clusters affects the ultrafast dissociation dynamics of adsorbed CH3Br molecules. *J. Phys. Chem. Lett.*, 13:4747.

van Elp, J., Potze, R. H., Eskes, H., Berger, R., and Sawatzky, G. A. (1991). Electronic structure of MnO. *Phys. Rev. B*, 44:1530.

van Oversteeg, C. H. M., Doan, H. Q., de Groot, F. M. F., and Cuk, T. (2017). In situ X-ray absorption spectroscopy of transition metal based water oxidation catalysts. *Chem. Soc. Rev.*, 46:102.

Werfel, F. and Minni, E. (1983). Photoemission study of the electronic structure of Mo and Mo oxides. *J. Phys. C: Solid State Phys.*, 16:6091.

Wernet, P., Gaudin, J., Godehusen, K., Schwarzkopf, O., and Eberhardt, W. (2011). Femtosecond time-resolved photoelectron spectroscopy with a vacuum-ultraviolet photon source based on laser high-order harmonic generation. *Rev. Sci. Instrum.*, 82:063114.

West Control Solutions Ltd (2018). *CAL-9900 Manual*.

Wiechen, M., Berends, H.-M., and Kurz, P. (2012). Water oxidation catalysed by manganese compounds: from complexes to 'biomimetic rocks'. *Dalton Trans.*, 41:21.

Wollschläger, J., Erdös, D., and Schröder, K.-M. (1998). The formation of mosaics during the reactive growth of MgO films on Ag(100). *Surf. Sci.*, 402–404:272.

Wu, M.-C., Corneille, J. S., Estrada, C. A., He, J.-W., and Goodman, D. W. (1991). Synthesis and characterization of ultra-thin MgO films on Mo(100). *Chem. Phys. Lett.*, 182:472.

Xu, X., Oh, W. S., and Goodman, D. W. (1996). Interfacial reactions between oxide films and refractory metal substrates. *Langmuir*, 12:4877.

Young, L., Ueda, K., Gühr, M., Bucksbaum, P. H., Simon, M., Mukamel, S., Rohringer, N., Prince, K. C., Masciovecchio, C., Meyer, M., Rudenko, A., Rolles, D., Bostedt, C., Fuchs, M., Reis, D. A., Santra, R., Kapteyn, H., Murnane, M., Ibrahim, H., Légaré, F., Vrakking, M., Isinger, M., Kroon, D., Gisselbrecht, M., L'Huillier, A., Wörner, H. J., and Leone, S. R. (2018). Roadmap of ultrafast X-ray atomic and molecular physics. *J. Phys. B: At. Mol. Opt. Phys.*, 51:032003.

Zaharieva, I., Chernev, P., Risch, M., Klingan, K., Kohlhoff, M., Fischer, A., and Dau, H. (2012). Electrosynthesis, functional, and structural characterization of a water-oxidizing manganese oxide. *Energy Environ. Sci.*, 5:7081.

Zaharieva, I., Najafpour, M. M., Wiechen, M., Haumann, M., Kurz, P., and Dau, H. (2011). Synthetic manganese–calcium oxides mimic the water-oxidizing complex of photosynthesis functionally and structurally. *Energy Environ. Sci.*, 4:2400.

Zinth, W. and Körner, H.-J. (1998). *Physik III: Optik, Quantenphänomene und Aufbau der Atome*. Oldenbourg Wissenschaftsverlag, München, 3 edition.

Zouros, T. J. M. and Benis, E. P. (2002). The hemispherical deflector analyser revisited. I. motion in the ideal 1/r potential, generalized entry conditions, kepler orbits and spectrometer basic equation. *J. Electron Spectrosc.*, 125:221.

Zürch, M., Chang, H.-T., Borja, L. J., Kraus, P. M., Cushing, S. K., Gandman, A., Kaplan, C. J., Oh, M. H., Prell, J. S., Prendergast, D., Pemmaraju, C. D., Neumark, D. M., and Leone, S. R. (2017). Direct and simultaneous observation of ultrafast electron and hole dynamics in germanium. *Nat. Commun.*, 8:15734.

Statement

I hereby declare that I have done the work independently and have not used any other sources and resources than those indicated, I have identified the passages taken over in words or content as references and have complied with the statues of the University of Ulm for the Protection of Good Scientific Practice as currently published.

I agree that the dissertation may also be used for the purpose of verifying compliance with generally accepted scientific standards, in particular by using electronic data processing programs.

Date and Signature: .....

Scientific Contributions

Posters:

January 30 – February 3, 2022, 739. WE-Heraeus-Seminar. Molecular Physics and Physical Chemistry with Advanced Photon Sources:
Christian Weigelt, Mihai E. Vaida, Thorsten M. Bernhardt, *Ultrafast wettability alteration: The decisive moments of adsorption on supported particles*

June 7–10, 2022, MUST 2022, International Conference on Molecular Ultrafast Science and Technology:
Christian Weigelt, Mihai E. Vaida, Thorsten M. Bernhardt, *Ultrafast wettability alteration: The decisive moments of adsorption on supported particles*

June 22–23, 2023, 15th BESSY@HZB User Meeting, HZB:
Christian Weigelt, Mihai E. Vaida, Thorsten M. Bernhardt, *Ultrafast wettability alteration: The decisive moments of adsorption on supported particles*

September 3–8, 2023, ISSPIC XXI International Symposium on Small Particles and Inorganic Clusters:
Christian Weigelt, Mihai E. Vaida, Thorsten M. Bernhardt, *Ultrafast wettability alteration: The decisive moments of adsorption on supported particles*

September 11–13, 2023, WavemiX 2023:
Christian Weigelt, Mihai E. Vaida, Thorsten M. Bernhardt, *Ultrafast wettability alteration: The decisive moments of adsorption on supported particles*

August 26–30, 2024, SRI 2024, Hamburg:
Christian Weigelt, Mihai E. Vaida, Thorsten M. Bernhardt, *Ultrafast wettability alteration: The decisive moments of adsorption on supported particles*

Oral Presentations:

September 2023, ISSPIC XXI International Symposium on Small Particles and Inorganic Clusters:
XUV - Beamline Raytracing: An introduction to RAY

February 2025, Physics Department, Lund University, Prof. Dr. Cord Arnold:
Femtosecond XUV Spectroscopy on Nano Structured Surfaces

Publications in Preparation

1. C. Weigelt, M. E. Vaida, T. M. Bernhardt:
   XUV-photoemission from manganese and manganese oxide nanoparticles on MgO,
   J. Phys. Chem. Lett. (2026), submitted for publication.

2. C. Weigelt, F. Knall, T. Gleitsmann, M. E. Vaida, T. M. Bernhardt:
   Temperature dependent electronic structure of MgO ultrathin films,
   Surf. Sci. (2026), in preparation for publication.

3. C. Weigelt, T. M. Bernhardt:
   High intensity XUV beamline for surface experiments in nano-catalysis,
   Rev. Sci. Instrum. (2026), in preparation for publication.

4. S. Mauthe, L. Niedringhaus, C. Weigelt, T. M. Bernhardt:
   Manganese and manganese oxide nanoparticles on ultrathin films: Characterization of geometric and electronic structure via STM and PES,
   Surf. Sci. (2026), in preparation for publication.

5. S. M. Lang, C. Weigelt, T. M. Bernhardt:
   Structures and catalytic properties of calcium-manganese-oxide clusters: A gas phase and surface science model system approach,
   Chem. Rev. (2026), in preparation for publication.